

UNIVERSITY OF TWENTE.

---

Modelling the effect of Andreev bound states  
on quantum transport in superconducting  
magnetic topological systems

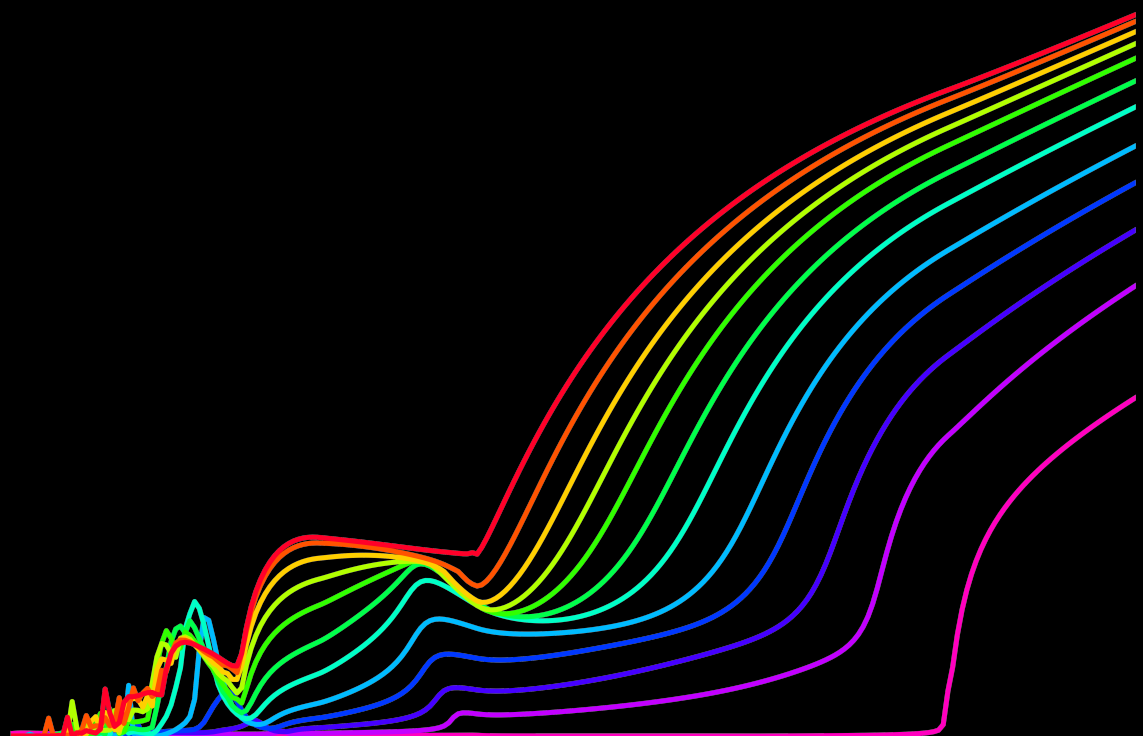
---

Master's thesis  
Applied Physics and Applied Mathematics

S. R. de Wit  
February 2022

**Supervisors:**  
prof.dr.ir. A. Brinkman  
prof.dr.ir. B.J. Geurts

Quantum Transport in Matter  
Faculty of Science and Technology  
Multiscale Modeling and Simulation  
Faculty of Electrical Engineering, Mathematics and Computer Science



## Abstract

The quantum transport in the sub-gap regime ( $|E| \leq |\Delta_0|$ ) in magnetic-superconducting-topological heterostructures was modelled using the Bogoliubov-de Gennes equations in combination with the recurrence relations. Following the prediction by Fu and Kane [1], an interface between a magnetic- and ( $s$ -wave) superconducting topological insulator was shown to host chiral Majorana modes in the form of Andreev bound states. Zero-energy Majorana modes are a fruitful approach to fault-tolerant topological quantum computing [2]. A novel mechanism to invert the chirality of the Majorana modes in such systems is proposed. To study the effect of the Andreev bound states on the electrical transport properties, the multiple Andreev reflection spectra in a topological Josephson junction consisting of a magnetic tunnel barrier are computed using the recurrence relations. A relationship between the location of resonance peaks in the computed  $I, V$ -curves for the topological Josephson junction and the Andreev bound state energies is established.

# Contents

<b>1</b>	<b>Introduction</b>	<b>1</b>
1.1	Quantum computing . . . . .	2
1.2	Majorana modes . . . . .	4
1.3	Modelling superconducting topological heterostructures . . . . .	9
<b>2</b>	<b>Reviewing theoretical concept of superconductivity and topological insulators</b>	<b>13</b>
2.1	Superconductivity . . . . .	13
2.1.1	The history of superconductivity . . . . .	14
2.1.2	BCS theory . . . . .	17
2.1.3	Superconducting ground state . . . . .	19
2.1.4	Quasiparticle excitation spectrum . . . . .	21
2.2	Andreev reflections . . . . .	25
2.2.1	Andreev bound state . . . . .	29
2.2.2	Multiple Andreev reflections . . . . .	30
2.3	Topological insulators . . . . .	34
2.3.1	TI edge states analogy to QHE . . . . .	34
2.3.2	Magnetic and superconducting topological insulators . . . . .	38
<b>3</b>	<b>Re-deriving and solving the Bogoliubov-de Gennes equations</b>	<b>41</b>
3.1	Derivation Bogoliubov-de Gennes equations . . . . .	42
3.1.1	Hamiltonian . . . . .	43
3.1.2	Mean field approximation . . . . .	44
3.1.3	Commutators . . . . .	46
3.1.4	Bogoliubov transformation . . . . .	49
3.1.5	Bogoliubov-de Gennes equations . . . . .	49
3.1.6	Bogoliubov-de Gennes equations in matrix form . . . . .	52
3.2	Solutions to the Bogoliubov-de Gennes equations . . . . .	54
3.2.1	Topological insulator . . . . .	56
3.2.2	Magnetic topological insulator . . . . .	57
3.2.3	Superconducting topological insulator . . . . .	59
3.2.4	Dispersion relations . . . . .	62
3.3	Time reversal- and particle-hole symmetry . . . . .	65
3.3.1	Basis 2 . . . . .	65
3.3.2	Symmetries of the Hamiltonian . . . . .	66
<b>4</b>	<b>Designing and implementing a symbolic tool</b>	<b>69</b>
4.1	Calculation route . . . . .	71
4.2	Tool motivation & assumptions . . . . .	74

4.3	How to use the tool . . . . .	75
4.4	Validation . . . . .	77
4.4.1	Equivalent wavefunctions in literature . . . . .	77
4.4.2	Manual reflection coefficient computation . . . . .	78
<b>5</b>	<b>Results</b>	<b>82</b>
5.1	Chiral Majorana modes as Andreev bound states . . . . .	83
5.1.1	TI-STI bilayer . . . . .	84
5.1.2	MTI-TI bilayer . . . . .	87
5.1.3	Andreev bound state phase coherence condition . . . . .	90
5.1.4	Andreev bound state, a necessary phase condition . . . . .	93
5.1.5	TI-MTI-TI-STI transmission . . . . .	95
5.2	Majorana mode chirality inversion . . . . .	98
5.3	Multiple Andreev reflections . . . . .	103
5.3.1	Fermi surface mismatch tunnel barrier . . . . .	104
5.3.2	Magnetic tunnel barrier . . . . .	105
5.3.3	Recurrence relations . . . . .	109
5.3.4	Fermi surface mismatch tunnel barrier spectrum . . . . .	111
5.3.5	Magnetic tunnel barrier spectra . . . . .	113
<b>6</b>	<b>Concluding remarks and outlook</b>	<b>121</b>
	<b>Appendices</b>	<b>128</b>
<b>A</b>	<b>Spinors basis 2</b>	<b>128</b>
A.1	Topological insulator . . . . .	128
A.2	Magnetic topological insulator . . . . .	128
A.3	Superconducting topological insulator . . . . .	129
<b>B</b>	<b>Equivalent spinors: spin rotation</b>	<b>130</b>
<b>C</b>	<b>Additional calculations</b>	<b>133</b>
C.1	TI-MTI-TI-STI-transmission . . . . .	133
C.2	AR coefficients . . . . .	134
<b>D</b>	<b>Recurrence relations for a topological tunnel junction</b>	<b>136</b>
D.1	Scattering matrices . . . . .	137
D.2	Recurrence relations for the TI/MTI/TI junction . . . . .	138
D.2.1	Recurrence relation for $B_n$ . . . . .	140
D.2.2	Recurrence relation for $A_n$ . . . . .	142

# 1 Introduction

In this thesis, the physics governing the behaviour of charge carriers in a system comprising of multiple interfaces between varying types of quantum materials is investigated. A custom-made tool was developed to predict various quantum transport parameters such as the conduction through and the transparency of a composite system of such interfaces. The modelled systems consist of the interfaces between superconducting, topological, and magnetic materials. The constructed tool automates the process of solving the Bogoliubov-de Gennes equations, which describe the charge carrier's wavefunctions in each material, and combines them with the (Andreev) scattering processes occurring at the modelled interfaces to effectively and efficiently compute quantum transport properties.

The foundation of the presented analysis is inspired by the work of Blonder Tinker and Klapwijk [3]. Further knowledge on the physics governing the transport near interfaces between magnetic and superconducting topological materials is of great interest considering the prediction by Fu and Kane [1] on the potential existence of chiral Majorana states in the form of zero energy Andreev bound state therein. The existence of Majorana states in solid-state physics has been a topic of discussion for decades as they could form the building blocks for the quantum bits (qubits) in a so-called topological quantum computer proposed by Kitaev [2]. An operational quantum computer would not only reduce the energy consumption of certain types of computations, but it also allows for the employment of various quantum algorithms proposed to model and study problems in medicine[4], networking, and finance [5] that are currently unsolvable with conventional supercomputers.

In the coming introduction, we shortly discuss the field of quantum computing and focus on the topological quantum computer. We define the core concepts in topological quantum computing and give adequate references to detailed discussion in literature. Next, we dive into the most promising candidate that could serve as a building block for a topological quantum computer called a Majorana mode. Subsequently, we discuss Majorana modes and explain how they can emerge in condensed matter systems and focus on the approach taken in this work. We close the introduction by sketching the outline of this thesis.

## 1.1 Quantum computing

In the past several decades our society has become fully dependent on the availability, reliability and security of the modern age information technology that advances in conventional computing have brought us. Banking, medicine, academia, the automotive industry, and various leisure activities all require the usage of a computer in any way shape or form. This increasing demand was and is the driving force behind the technological innovations in semiconductor-based computer chips that are responsible for faster, better and cheaper electronics. This progress went hand in hand with the size reduction of the computer chips, best captured by Moore's law [6]. The increasing demand on conventional computers has pushed its building blocks to their fundamental size limits where quantum mechanical effects halter further improvements of the conventional technology putting an expected stop to Moore's law [7].

Rather than fighting against the quantum effects emerging at the smallest length scales, quantum computers embrace these effects by considering precisely those effects as the foundation of their units of computation. The field of quantum computing builds on notions from quantum physics to investigate novel ways to probe computational power in computing science. At its core, quantum computing relies on the principles of superposition and quantum entanglement to build and manipulate its units of computation called qubits (quantum bits). A given quantum system (e.g. qubit) can be in a simultaneous superposition of many different states [8]. A conventional computer uses bits as units of computing that can either be in an on (1) or off state (0), so a system consisting of a sequence of  $n$  bits spans a space of  $2^n$  unique binary configurations. Through the principle of superposition, a qubit can be in a superposition of linear combinations of any of those unique configurations at the same time. This vastly enlarges the realm of possible configuration states. Ordinary computations with qubits in superposition of many states are not trivial and require adapted algorithms called quantum algorithms. For an excellent detailed overview of the principles of quantum computing and quantum information the reader is referred to [8], [9].

Already in the 1980s the idea of quantum computing was suggested by Yuri Manin [10], Richard Feynman [11], and Paul Benioff[12]. Shor's 1994 discovery[13] of an efficient quantum algorithm for integer factorization in polynomial time sparked a further interest in the field of quantum computers. This is because most current online security systems rely on the public key cryptosystem called RSA[14], and RSA is built on the inability of conventional computers to factor large prime numbers. Fortunately, a form of

quantum cryptography [15] is robust against quantum algorithms. The sole purpose of the field of quantum computing is not to oppose the threat of breaking modern RSA based encryption it posed itself by countering it with quantum cryptography. Fully operational quantum computers would, namely offer a wide range of applications ranging from energy-efficient computing; and solving complex networking problems [5]; to the biological sciences and medicine [4].

The first small 2-qubit quantum computer was built as early as 1997, and in 2001 an operational 5-qubit optical quantum computer successfully found the prime factors of the number 15 [8]. A demonstration of the state of the art operational quantum computer is Google's 'quantum supremacy' experiment [16], in which a quantum computer performed a complicated sampling task on 53 qubits that is claimed to be no longer viable in a reasonable time on the largest existing conventional supercomputer [8].

The usage of quantum computers is however not widespread. This is due to the heavy constraints put on a quantum system that is to be used as a reliable qubit. The most notable requirements were first described by DiVincenzo and Loss [17] and can be summarized as [9]: " a qubit should be able to be *prepared* in, at least, two distinct states (like the '0' and '1' in bits); the states are weakly coupled to avoid information losses giving rise to *low decoherence* rates on the long time scale; we can switch between the states using a *controlled unitary transformation*; and we can perform *state-specific quantum measurements* to get a reliable readout "

The restrictive criteria imposed on physical systems to be used as qubits pose practical problems haltering the physical realizations of quantum computers. However, as early as the 1990s in relatively short succession to the development of the first quantum algorithms, physical systems potentially hosting entangled states suitable to be used as a qubit were already suggested. The proposed systems came from various fields of physics. These fields were nanophysics, condensed matter physics, nuclear physics, optics, and topology. Many of the initially proposed ideas remain a fruitful fields of study since there is still a great interest in the potential for qubits based on, for instance quantum dots [18], bulk nuclear magnetic resonance [19], linear optics [20],[21], and topological materials [22]. In this work we focus on the former class, i.e. we model the quantum transport in materials that show potential to be used as building blocks for a so-called topological quantum computer.

Topological quantum computation is the pursuit to store and manipulate quantum information using so-called non-abelian anyons. Anyons are quasi-particle excitations of a topological phase of matter<sup>1</sup> that are neither bosons (integer spin) nor fermions (half-integer spin) [23]. Given two indistinguishable particles in 2D, anyons can be defined [24] as the class of particles that gain a complex phase different from  $-1$  or  $1$  upon the clockwise exchange of the two particles. Recall that by the Pauli exclusion principle [25] the class of particles whose wavefunction gains a factor  $-1$  ( $1$ ) are called fermions (bosons) - these are anti-symmetric (symmetric) under such an exchange. Elementary computations on a topological quantum computer are done by braiding quasi-particles and the subsequent measurement of the formed multi-quasiparticle state [26]. Anyons that satisfy the property that for two elementary braiding operators the order in which we apply them matters are called non-Abelian anyons.

Yuri Kitaev showed that in a two-dimensional quantum system unitary transformations performed by moving the anyonic excitations around each other gives rise to quantum computations that are fault-tolerant by their physical nature [2]. Non-abelian anyons are described by a degenerate energy spectrum giving rise to non-local properties. This non-locality protects them from errors caused by local perturbations giving rise to the fault tolerance of a topological quantum computer [23]. Three main classes of systems possibly hosting non-Abelian anyons are fractional quantum Hall states, intrinsic  $p$ -wave superconductors, and topological superconductors in heterostructures [27]. The most promising and experimentally most tractable candidates to perform topological quantum computations are localised (pairs of) zero-energy Majorana modes in superconducting heterostructures [22]. We will consider those in the next section.

## 1.2 Majorana modes

A Majorana mode in solid-state physics is the emerging quasiparticle excitation that is its own anti-particle. It is named after the Majorana fermion postulated by Ettore Majorana [28], but does not constitute a fundamental particle. The fact that a Majorana mode is its own antiparticle means that by definition it should be charge- and spin-less. Already suggested in 1937, the Majorana fermion has never been experimentally observed. In the field

---

<sup>1</sup>Technical terms such quasiparticle excitations of a topological phase of matter will be discussed at length in the coming theory chapters.

of (theoretical) high energy physics, the particle however continues to pop up in discussions of the nature of neutrinos and open questions about dark matter[29]. In condensed matter physics the Majorana ‘particle’ enters the stage as a state suggested to obey the non-Abelian anyonic statistics required in topological quantum computing. In this section, we introduce the fundamental properties of (chiral) Majorana modes in the context of this work. The reader is referred to [22], [27], and [30] for a detailed overview of the physics governing Majorana modes in condensed matter.

In contrast to the Majorana fermion, a Majorana mode is a *quasi*particle excitation, and not a fundamental particle (e.g. protons and electrons). This means that a Majorana in condensed matter physics emerges as a simultaneous combination of excitations of fundamental particles (e.g. electrons and holes) of a state of matter (e.g. a topological superconductor). We consider electrons as filled states with an energy  $E$  above the Fermi level<sup>2</sup>  $E_f$ , and holes as the oppositely charged absence of states with an energy  $-E$  below the Fermi level. To describe Majorana modes in operator language we introduce the electronic field operators  $c_\sigma^\dagger(E)$  and  $c_\sigma(E)$  creating(adding) and annihilating(removing) an electron with spin  $\sigma$  and energy  $E$  from a state. Here the ‘dagger’ superscript  $\dagger$  is the Hermitian conjugate. We also introduce the creation and annihilation operator associated with a Majorana mode, as  $\gamma^\dagger(E)$  and  $\gamma(E)$ . The relation that a Majorana particle is its own antiparticle then implies  $\gamma = \gamma^\dagger$ .

In a system having particle-hole symmetry, creating a quasiparticle with energy  $E$  or removing one with energy  $-E$  are identical operations. Phrased in operators this reads

$$\gamma(E) = \gamma^\dagger(-E), \quad (1.1)$$

for  $\gamma^\dagger(E)$ , ( $\gamma(E)$ ) creating (annihilating) a particle in a particle-hole symmetric system at energy  $E$  relative to the Fermi energy  $E_f$ . This means that only at the Fermi level  $E = 0$ , we have  $\gamma(0) = \gamma = \gamma^\dagger$ . Furthermore this shows that Majorana modes necessarily occur at  $E = 0$  in particle-hole symmetric systems.

We will show in the coming theoretical survey in section 2.1 that an s-wave superconductor obeys particle-hole symmetry and its quasiparticle

---

<sup>2</sup>The Fermi level is defined at zero temperature as the energy of the electron in the highest occupied momentum state. At  $T = 0$  this is equivalent to the energy required to add an additional electron called the chemical potential. Often the two notions are (erroneously) used interchangeably at finite temperature.

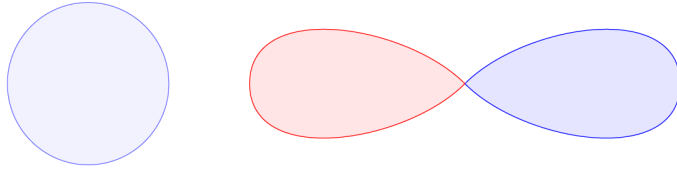


Figure 1: Image from [32]: a two dimensional illustration of the pair potentials of  $s$ -wave (left) and  $p$ -wave (right) superconductors. For  $s$ -wave superconductors, the pair potential is isotropic, for  $p$ -wave superconductors, the pair potential has a strong angle dependence,  $\Delta = \Delta_0 \cos \phi$ , where  $\phi$  is the angle made with a horizontal line. Colour coding has been used to indicate the sign of  $\Delta$ .

excitations are a superposition of electron and hole excitations. Since electrons and holes have opposite charge, and opposite energies relative to  $E_f$  we have that, c.q. (1.1), zero energy excitations in a superconductor are charge neutral and equally electron-like (particle) hole-like (anti-particle) [30]. Superconductors therefore provide a natural basis for such chargeless Majorana modes. Based on that we might naively construct a ‘Majorana’ excitation in a superconductor as a linear combination of these hole and electron creation operators,  $\gamma^\dagger = \alpha c_\sigma^\dagger + \beta c_{-\sigma}$ , for  $\alpha, \beta \in \mathbb{C}$ , such that the total state is chargeless. However, this form is distinct from its ‘anti-particle’ version,  $\gamma = (\gamma^\dagger)^\dagger = \beta^* c_{-\sigma}^\dagger + \alpha^* c_\sigma$  because of the opposite spin. This means that in a pure  $s$ -wave superconductor Majorana states can not exist. If we had a spinless version of the above system, then we might have zero energy Majorana modes. Fortunately Read and Green showed in their seminal work [31] that in the spinless chiral  $p_x + ip_y$  superconductors Majorana states emerge when in contact with a material breaking time reversal symmetry (e.g. a magnet). The difference between an isotropic  $s$ -wave (singlet) superconductor and an an-isotropic  $p$ -wave (triplet) superconductor is illustrated in figure 1. Please note that we construct linear combinations of  $p$ -waves to form e.g.  $p_x + ip_y$ -wave superconductors.

The emergence of Majorana states in spinless  $p$ -wave superconductors sounds promising, but actual materials exhibiting such  $p$ -wave superconductive pairing are still to be found ( $\text{Sr}_2\text{RuO}_4$  is a promising candidate [33]). An analogous system can however be constructed by inducing superconductivity onto the 2D surface states of a 3D topological insulator (topological insulators are discussed in section 2.3). As was shown by Fu and Kane [1] the  $s$ -wave superconductivity induces a  $p_x + ip_y$ -wave like superconductive pairing into the 2D edge states. They predicted for a heterostructure of an  $s$ -wave superconductor in contact with a topological insulator and a material

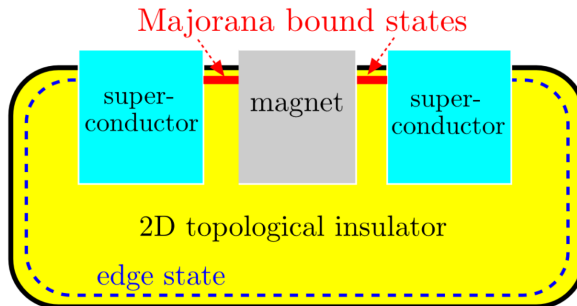


Figure 2: Top view of a 2D topological insulator, contacted at the edge by two superconducting electrodes separated by a magnetic tunnel junction. A pair of Majorana fermions is bound by the superconducting and magnetic gaps. In red we indicate the spatial location the Majorana bound states are predicted to be localized. The figure is an adaptation of [30]

that breaks time-reversal symmetry (e.g. a magnetic active material) the appearance of Majorana modes in the form of so-called Andreev bound states. Figure 2 illustrates the Majorana states bound at the interfaces in such a heterostructure.

An alternative system, proposed by Kitaev [34], is the superconducting 1D quantum wire potentially hosting Majorana's. In this field, this is the most probed both theoretically and experimentally. Similar to the work by Read and Green[31] where Majorana modes were suggested to be pinned at magnetic active sites (magnetic vortices or an interface to a magnetic material) within a  $p$ -wave superconductor, the so-called Kitaev chain supports the appearance of Majorana modes near the ends of a superconducting wire. Again, this toy-model supposes the existence of a  $p$ -wave superconductor, but it was found that by inducing  $s$ -wave superconductivity into a semiconducting nanowire with strong spin-orbit (Rashba) coupling, and placing it in external magnetic fields [35][36] a system analogous to the Kitaev chain could be formed [22].

Having considered various systems potentially hosting Majorana modes, we close this section by summarizing the properties of chiral Majorana's and describing possible experiments to detect them. In condensed matter systems a Majorana mode,

- Is its own antiparticle  $\gamma = \gamma^\dagger$
- Is a quasiparticle and not a fundamental particle
- Occurs at zero energy (relative to the Fermi level)

- Is spinless
- Is chargeless

For all practical purposes in their application in topological quantum computing, they should emerge in a pair of spatially separated localized Majorana zero modes[27].

In passing, the term *chiral* Majorana was mentioned. The chirality here refers to the direction of motion of the Majorana mode along the surface near which it is located. Consider for instance the edge state in figure 2. On the 2D surface states in the topological insulator, edge states occur that are analogous to those in the quantum Hall systems [37]. The emerging Majorana mode that is pinned at the magnet's surface, adopts the same direction of motion as the edge state, thus giving it a chirality. The term chiral Majorana is often used to describe a mode initially at zero energy, obeying the criteria above, that through some external effect (magnetic orientation, chemical potential, etc) has gained a finite energy and becomes de-localized. In that sense, the chiral Majorana mode (CMM) is not strictly a Majorana zero mode anymore, but by a continuous change of said external parameter, it can be brought back to the zero energy state. The chirality of the Majorana modes is shown to be a controllable property [38][39] and is important in proposed experiments for (chiral) Majorana detection [27].

We now list a couple of exemplary signatures of Majorana modes that could be observed experimentally. We state the most notable Majorana characteristics that can arise, the reader is referred to the cited works for more details.

- *Josephson current<sup>3</sup> effects.* The detection of a so-called zero-bias conductance peak occurring at zero bias voltage would be a smoking gun of zero-energy Majorana modes [27]. Alternatively observing a  $4\pi$ -periodic Josephson effect would too [30]. Here the periodicity is with respect to the superconducting phase difference over the two superconductors. Moreover, one of the key experimental electrical transport observables are  $I, V$  characteristics, and the presence of Majorana zero modes is predicted to show up as resonances and steps in the current at predictable bias voltages [40],[41].

---

<sup>3</sup>The Josephson current is the unique current that starts to flow between two superconducting current leads that have a so-called superconducting phase difference and are connected by some form of link (e.g. contact resistance, tunnel barrier). This will be clarified in section 2.1

- *Tunneling signatures of Majorana modes.* Direct detection of Majorana bound states through tunnelling spectroscopy can be done by observing a conductance of  $2e^2/h$  that without Majorana bound states would be absent [30].
- *Interferometry.* Observing discrete conductance oscillations for a varying applied magnetic flux in a ferromagnetic insulator-3D topological-superconductor heterostructure would provide clear evidence for chiral Majorana edge states in the system [27].
- *Thermal transport properties.* Collective properties of Majorana modes can be detected in thermal conductance. [30]. Moreover, the inverted chirality (changing the direction of motion) of CMM would be visible in transport experiments both in thermal and in electrical conduction [39].

### 1.3 Modelling superconducting topological heterostructures

We have identified two distinct approaches to Majorana modes in superconducting systems. On the one hand, we have the intrinsic  $p_x + ip_y$ -wave superconductors and on the other hand, we have the 'induced'  $p$ -wave superconductors. The latter class is further divided into the superconducting nanowires, and heterostructures of an  $s$ -wave superconductor, a 3D topological insulator, and a magnetic active site. These systems can mathematically be described by using different machinery in different regimes. For instance one can study the assumed intrinsic  $p$ -wave superconductors in a dirty (very diffusive) limit using Green's functions techniques [42][32]. Similarly, many efforts are done towards modelling the intrinsic and induced  $p$ -wave superconductivity Kitaev chains using the Bogoliubov-de Gennes equations as reviewed in [43]. In this thesis, we will model the quantum transport in the heterostructures consisting of 3D topological insulators,  $s$ -wave superconductors, and (ferro)magnetic insulators using the Bogoliubov-de Gennes equations (described in chapter 3).

To illustrate the type of heterostructures considered in this study we show figure 3. Here we see a 3D topological insulator (TI) with 2D surface states indicated in grey, on top of which  $s$ -wave superconductors (S) and a ferromagnetic insulator (F) are placed. The superconductors locally induce superconductivity into the 2D surface states beneath it. In this way, we form a region that is referred to as an (induced) superconducting topological

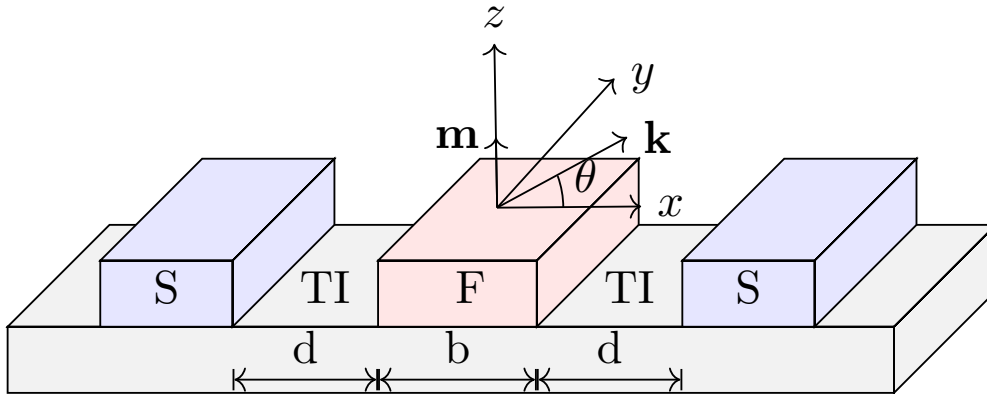


Figure 3: Simplistic schematic of a superconducting topological junction that hosts MAR. From left to right the system consists of an STI, TI, MTI, TI and STI. The STI and MTI are formed by the ferromagnetic insulator (F) and *s*-wave superconductor (S) stacked vertically on top of the 3D topological insulator (TI), through the proximity effect. The width of the MTI and the TI segments are indicated. The axis system is illustrated such that  $\mathbf{k}$  is in the 2D  $xy$ -plane and the magnetic orientation in F is along  $z$ .

insulator (STI). Similarly, the magnetization  $\mathbf{m}$  in the ferromagnetic insulator induces ferromagnetism into the TI region below it forming a so-called magnetic topological insulator (MTI). We might consider slight variations or sub-parts of the system in figure 3. In a 3D TI, all charge is (theoretically) carried by 2D surface states, thus our domain of computation is the 2D region<sup>4</sup> on the top side of the TI on which locally superconductivity or magnetism is induced. This means that we only consider charge carriers moving in the  $x, y$ -plane.

When we consider the superconductors on either end of the system in figure 3 as current leads, we get a so-called topological Josephson junction. The term Josephson junction is used to describe a system of superconducting leads connected by some form of a link, be it a quantum dot, (tunnel) barrier or interface. In the limit that the distance  $d$  between the superconductors and ferromagnetic insulator goes to zero, we get two interfaces between an STI and MTI that are claimed [1] to host chiral Majorana modes in the form of Andreev bound states.

In light of the predicted Majorana modes emerging in topological - superconducting - magnetic heterostructures and their intriguing application

<sup>4</sup>If we ignore the interference effect from the underlying bulk states on the surface states, which is observed experimentally [44].

in topological quantum computing, the academic ground to research them further is apparent. In literature the quantum transport of systems such as figure 3 has been studied in the 1D limit in [40][41],[45]; a MTI-TI-STI sub-system was shown to host controllable chiral Majorana modes [38]; and an attempt to model multiple Andreev reflections in 2D [46] proved promising. In this thesis, we hope to further the discussion in [46] by modelling the quantum transport using the Bogoliubov-de Gennes equations to study the physics governing the different scattering mechanisms taking place at the various interfaces in figure 3.

The structure of this thesis is as follows. We first qualitatively introduce key notions and concepts from superconductivity and topological materials in chapter 2. Here we introduce the physics governing *s*-wave superconductivity and the scattering mechanism occurring at interfaces with a superconducting material, that is key to this work, called Andreev reflections. The reason for the interest in *s*-wave superconductivity, is the proposed [1] equivalence between induced *s*-wave superconductivity into topological surface states and *p*-wave superconductivity. From the concept of Andreev reflection, we describe multiple Andreev reflections and the formation of Andreev bound states. Next, we discuss the origin of topological materials and their place in this work.

After this qualitative introduction, in chapter 3 we introduce and describe the set of so-called Bogoliubov-de Gennes equations (BdG) used to make quantitative predictions in this analysis. In short, the BdG equations are coupled Schrödinger equations describing the wavefunctions in superconducting materials. We re-derive the BdG equations to accommodate topological (spin-orbit coupling) and magnetic (Zeeman term) effects, and write this into a matrix Schrödinger form,  $H_{BdG}\phi = E\phi$ . Then we solve for the plane wave eigenvector solutions to the BdG Hamiltonian in matrix form. We close this section with a discussion on the (broken) symmetries of the BdG Hamiltonian. The derived wavefunction eigensolutions to the BdG Hamiltonian are used to compute the complex coefficients associated with the reflection and transmission of plane wave wavefunctions inbound on e.g. an interface between two materials of varying kinds. The derivation of the wavefunctions and the computation of the wavefunction amplitudes are all automated using a custom made tool described in chapter 4. The type of computations automated by the tool are in essence trivial steps but are prone to error, repetitive and time-consuming.

In chapter 5 the outcome of the tool is used to model and predict various

quantum transport properties such as the transmission through a tunnel barrier, the formation of chiral Majorana modes in the form of Andreev bound states in a bilayer system, the effect of said Andreev bound state on the electrical conduction through a system, or the modulation of the DC current as a function of the applied bias voltage ( $I(V)$  curve) due to multiple Andreev reflections. By applying the tool to such problems, we first validate its correctness by re-deriving various results in literature [47], [38] and [41] before applying it to uncover novel findings such as a new mechanism for the inversion of chiral Majorana's and the rich multiple Andreev reflection spectrum for a 2D topological Josephson junction consisting of a magnetic tunnel junction. These results are a basis for discussion and further research (section 6).

## 2 Reviewing theoretical concept of superconductivity and topological insulators

We are interested in the physics governing the behaviour of charge carriers in a system comprising of (multiple) junctions between magnetic, superconducting and/or topological and materials. In order to model such systems, we require knowledge on superconductivity and topology (in the context of condensed matter physics). This chapter provides an overview of the theoretical framework underlying the governing physics. It comprises of a qualitative introduction to superconductivity and topological materials and acts as an introduction to the underlying physics we attempt to model in chapter 3. The computation work in this thesis revolves around the Bogoliubov-de Gennes equations, which are discussed, derived, and solved in chapter 3.

This chapter is structured as follows, we first qualitatively introduce superconductivity and topological insulators in sections 2.1 and 2.3. In the former section we briefly sketch the relevant (historic) background before we focus on the concepts that are key to the further analysis, such as BCS-theory, which is the most complete theory describing the microscopic origin of superconductivity. Moreover by explaining BCS-theory we can in a natural way introduce notions that will become vital later on in this thesis such as the (quasi)particle excitation spectrum, and Andreev reflections. After this we delve further into the phenomenon of Andreev reflections in section 2.2 by considering the occurrence of a so-called Andreev bound state in a system consisting of multiple interfaces. In section 2.3 we introduce the relevant notions of topological mater in the context of condensed matter physics. The reason for the interest in the combination of topology and these Andreev bound states is the prediction by Fu and Kane [1] on the emergence of a zero energy Majorana bound state as an Andreev bound state in certain topological superconducting junctions.

### 2.1 Superconductivity

We first give a brief historical introduction to the field of superconductivity before introducing the superconductivity concepts relevant to this work. The historical account is mainly based on chapter 1 in [48], and the section on the relevant concepts is based on chapters 6 and 7 in [48]. This abridged introduction does not do credit to the rich field of superconductivity neither from a theoretical perspective nor from an engineering one. The reader is referred to the mentioned work for an elaborate overview of the subject.

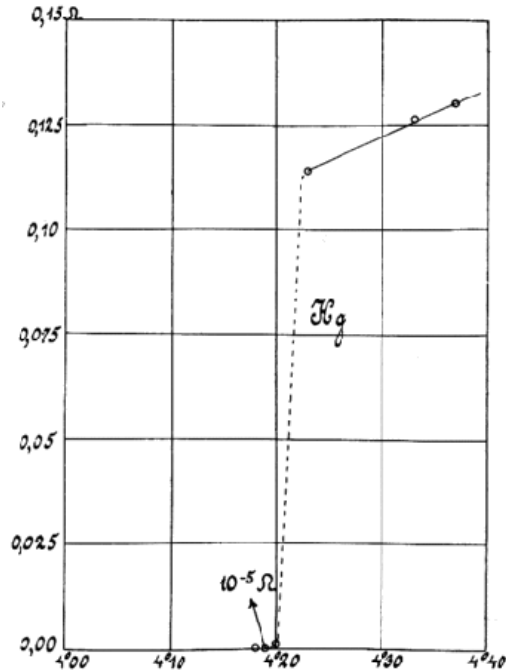


Figure 4: Kamerlingh Onnes' original[50] plot showing the measured resistance ( $\Omega$ ) as a function of temperature (Kelvin). This observed rapid decrease in electrical resistance around the critical temperature of 4.2K for mercury lead to the discovery of superconductivity.

### 2.1.1 The history of superconductivity

At the beginning of the 20<sup>th</sup> century the Dutch physicist Heike Kamerlingh Onnes founded the cryogenics laboratory at the university of Leiden where the lab would become the first to liquefy Helium. This breakthrough enabled the possibility to cool samples down to a few Kelvin. In 1911 whilst studying the temperature dependency of mercury Kamerlingh Onnes was the first to observe the hallmark of superconductivity [49]. He discovered that for a temperature around 4K the electrical resistance of the mercury suddenly dropped to zero (immeasurable) and even remain there for decreasing temperatures. Kamerlingh Onnes was the first to measure the critical temperature that marks the transition of a material from a resistive state to a so-called superconducting state as seen in figure 4. In a superconducting state a material has the capability to carry an electrical current without generating resistance, i.e., without requiring an applied voltage.

Kamerlingh Onnes' findings stood in stark contrast to the leading ideas and theoretical predictions on the temperature dependency of the resistivity



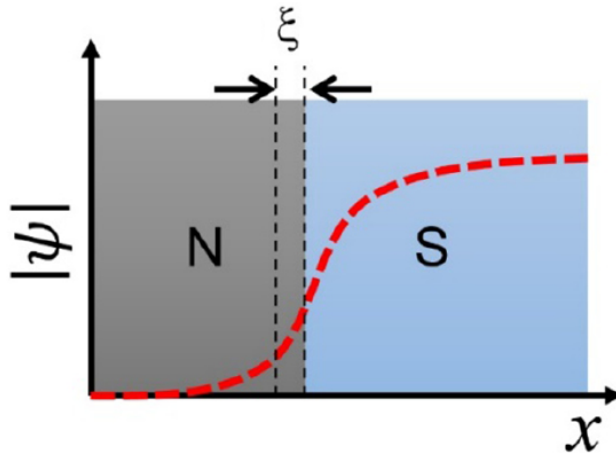


Figure 6: The superconducting order parameter  $|\psi|$  of a superconductor (S) penetrating into the normal metal (N) with a length scale of the superconducting coherence length,  $\xi$ . Image courtesy of [55]

Ginzburg-Landau[54] theory, that included quantum mechanics, being the most successful ones.

Two important notions from Ginzburg Landau theory that will become important later on in our investigations are the order parameter  $\psi(\mathbf{r})$  and the coherence length  $\xi$ . The origin of the order parameter is based on the important physical insight that Landau and Ginzburg brought forward, namely the combination of quantum mechanics with the physics of phase transitions borrowed from thermodynamics. The observational evidence Ginzburg and Landau aimed to describe was the phase transition between the superconducting and non-superconducting phase occurring at a critical temperature. In a combined effort to unite quantum mechanics and the knowledge on phase transitions, they introduced the order parameter as both the effective quantum mechanical wavefunction of superconducting electrons and the quantity that undergoes a second order phase transition. A second order phase transition is accompanied by a gradual change in the order parameter, while there is a discontinuous change in a system's symmetries at the transition temperature.

From the order parameter introduced as the wavefunction describing the superconducting electrons we can define a characteristic length scale called the coherence length. Let the  $\psi(x)$  be the order parameter as a function of some spacial coordinate  $x$  (for simplicity we consider only a single coordinate here). Consider now a superconducting slab on which we deposit a thin film

of normal metal at say  $\mathbf{x}_0$ . Close to the interface the normal metal becomes slightly superconducting, whilst locally suppressing superconductivity on the superconductor's side as illustrated in figure 6. This means that in the superconductor near the interface the order parameter is reduced relative to the bulk inside the superconductor (where we set the order parameter to 1). Hence here we have that  $|\psi(x \sim x_0)| < |\psi(x \gg x_0)|$ . This phenomenon is referred to as the superconducting proximity effect[48]. The coherence length is defined as the characteristic length over which the order parameter recovers to 1 when departing from the normal metal interface into the superconducting material.

### 2.1.2 BCS theory

In the coming section we will introduce and describe quasiparticle excitations in a 'regular' *s*-wave superconductor using BCS theory, because later on we will model quantum transport of those quasiparticle excitations in more complex systems using the Bogoliubov-de Gennes equations. Following the discovery of superconductivity, the empirical theories of Landau and Ginzburg successfully predicted many remarkable properties of superconductors, these empirical theories do not address the microscopic origin of superconductivity. Bardeen, Cooper, and Schrieffer (BCS) were collectively the first to describe the physical mechanism of superconductivity in their microscopic theory [56]. Please note that the BCS theory presented here is a microscopic theory that correctly predicts many features for the class of so-called BCS superconductors, indicated by the dark green circles in figure 5. For many of the other classes of superconductors BCS theory and its proposed phonon induced electron-electron interaction is insufficient and advanced pairing mechanisms and corresponding theories need to be constructed.

In the original microscopic theory for superconductivity [56] it was proposed that superconductivity was due to a coupling between electrons mediated by lattice vibrations (phonons in solid state physics language). This idea was inspired by the isotope effect, i.e., the experimentally observed power law dependency of the critical temperature on mass of the used isotope of superconducting metals. This observation suggested that the atomic lattice might be an important player in these electron-electron interactions.

The Feynman diagram [57] describing a phonon mediated interaction is given in figure 7. An electron pair with momenta labels  $(\mathbf{k}_1, \mathbf{k}_2)$  exchange momentum,  $\mathbf{q}$ , through a phonon-mediated interaction, and end up in the momenta states  $(\mathbf{k}_1', \mathbf{k}_2')$ . Let  $\omega$  be the lattice frequency associated with

this exchanged momentum  $\mathbf{q}$ . Then the order of magnitude for the displaced momentum is set by the natural characteristic frequency of the lattice, i.e., the Debye frequency ( $\omega_D$ ). This restriction limits the allowed momenta of electrons undergoing the proposed phonon mediated pairing. Only those electrons that are an energy  $\hbar\omega_D$  away from the Fermi level take part in the attractive pairing. Roughly speaking, in a bulk superconductor, like in a metal, Pauli's exclusion principle tells us that electrons can not occupy the same state, so there is an energy, defined as the Fermi level<sup>5</sup> (chemical potential) describing the (kinetic) energy of the highest occupied electron state. We can translate the  $\hbar\omega_D$  restriction in energy for the BCS coupling to momentum space, and visualize this as a slab of thickness  $2\Delta k$  around the Fermi surface. Similar to the Fermi level in energy, we have the Fermi surface in momentum space. In momentum space, the lowest (kinetic) energy states occupy to the lowest momenta states, and higher (kinetic) energy states reside at higher momenta states, until we arrive at the highest energy state, the Fermi level, which then sets the limit for the momenta of the outer states on the surface, called the Fermi surface. The states on the Fermi surface are a distance  $k_F$  (Fermi wavevector) away from the origin. In a 2D (3D) electron gas the Fermi surface is a circle (sphere). The superconducting case shall be discussed later when we discuss the superconducting ground state in section 2.1.3.

The conservation of momentum during the scattering illustrated in figure 7 restricts the possible momenta in the final state ( $\mathbf{k}_1', \mathbf{k}_2'$ ). Figure 8 shows the possible allowed areas in  $\mathbf{k}$ -space for the final state to be located. The scattering amplitude for this interaction increases as the area of potential outcomes increases. So observe that this region is maximal as  $\mathbf{q} \rightarrow 0$ , hence the pairing is the strongest when the wave vectors oppose. This explains the reason for the pairing of electrons of opposite momenta in the BCS theory. Such a pair of coupled electrons became known as Cooper pairs. Phrased in the language of second quantization, Bardeen, Cooper, and Schrieffer showed that such an interaction, when attractive and stronger than Coulomb repulsion, lowers the energy if electrons are coupled. This pairing renders the Cooper pairs protected from (non-magnetic) scattering events, yielding the superconducting state. The superconducting state remains for temperatures below the material specific  $T_c$ , because then thermal excitations do not provide sufficient energy to break the Cooper pairs.

---

<sup>5</sup>We consider a material in its superconducting state, which implies a sufficiently low temperature (few Kelvin), but at absolute zero the Fermi level coincides with the Fermi energy, so the two notions might both be used in this context.

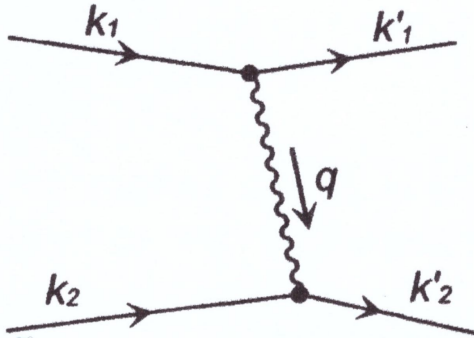


Figure 7: A graphical representation of the proposed coupling mechanism in BCS theory, two electrons (of momenta  $\mathbf{k}_1$  and  $\mathbf{k}_2$ ) interact with each other through the underlying atomic lattice. The two electrons scatter to two new momenta states ( $\mathbf{k}_1'$  and  $\mathbf{k}_2'$ ) by exchanging a momentum  $\mathbf{q}$  via a lattice vibration. Formally speaking, this is a so-called Feynman diagram describing the electron-electron interaction for an incoming electron with initial momentum  $\mathbf{k}_1$  emitting a phonon of momentum  $\mathbf{q}$  that subsequently is absorbed by another electron with initial momentum  $\mathbf{k}_2$ . This figure is taken from [48].

### 2.1.3 Superconducting ground state

At absolute zero, the lowest energy configuration (ground state) for a superconducting metal is quite different from an electron gas. In fact, contrary to a for instance an electron gas, the density of states is not a packed Fermi surface with all states inside it occupied and the rest empty, but rather within a distance  $\Delta\mathbf{k}$  from the Fermi surface there are respectively occupied and unoccupied electron states. This is indicated in figure 9 and expresses the phonon-mediated interaction between electrons near the Fermi level. The existence of occupied states in the ground state above the Fermi level might sound counter intuitive as these states possess a higher kinetic energy than they would in say the ground state of an electron gas. This energy gain by electrons occupying a higher energy state is however compensated by the negative energy contribution due to the attractive electron pairing potential. Pairing can only occur if a pair, say  $(\mathbf{k}_1, \mathbf{k}_2)$ , can scatter to a previously empty state  $(\mathbf{k}_1', \mathbf{k}_2')$ , this gives rise to the unoccupied states within the Fermi level in the ground state. The combination of the existence of unoccupied states within and occupied states outside the Fermi surface, effectively smears out the Fermi surface. This is similar to what happens for normal metals due to thermal excitations, but in superconductors this smearing already occurs at zero temperature.

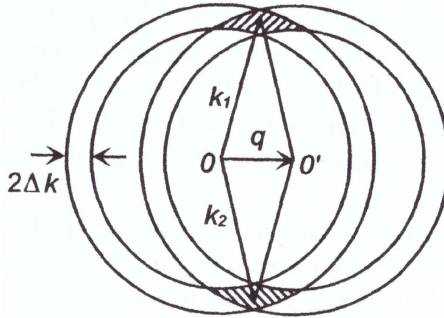


Figure 8: A figure describing the allowed areas in  $\mathbf{k}$ -space for a phonon-mediated interaction. For an initial state  $(\mathbf{k}_1, \mathbf{k}_2)$ , the shaded region indicates the possible available states to scatter into. This figure is taken from [48]

Bardeen, Cooper, and Schrieffer showed that relative to the ground state energy, the energy cost due to the addition of a single electron at state  $\mathbf{k}$ ,  $E_{\mathbf{k}}$ , is given by<sup>6</sup>

$$E_{\mathbf{k}} = \sqrt{\varepsilon_{\mathbf{k}}^2 + \Delta_0^2} = \sqrt{\left(\frac{\hbar^2 \mathbf{k}^2}{2m} - \frac{\hbar^2 \mathbf{k}_f^2}{2m}\right)^2 + \Delta_0^2} \geq |\Delta_0|, \quad (2.1)$$

where  $\varepsilon_{\mathbf{k}}$  is the kinetic energy for an electron in state  $\mathbf{k}$ ,  $\mathbf{k}_F$  is the Fermi wavevector, and  $\Delta_0$  is the superconducting energy gap (for conventional superconductors). The superconducting energy gap is a material property and has the units of energy. It is a measure for the cost of adding an excitation to the superconducting ground state. It can be shown [48] that it scales globally as

$$\Delta_0 \approx \frac{3.58}{2} k_b T_c, \quad (2.2)$$

where  $k_b$  is the Boltzmann constant and  $T_c$  is critical temperature.

The spectrum (2.1) shows another signature of superconductivity, namely that the excitation spectrum shows a gap about the Fermi level. This can be seen by the fact that if we would like to excite a state from the ground state, regardless the value of  $\mathbf{k}$ , we require an energy  $E_{\mathbf{k}} \geq \Delta_0$  i.e., no excited states exist below an energy of  $\Delta_0$ . The separation between the ground state energy and the excited energy levels is called the energy gap, hence the name for  $\Delta_0$ . The spectrum shall be discussed at length in section 2.1.4

<sup>6</sup>See [48] chapter 6 for more details.

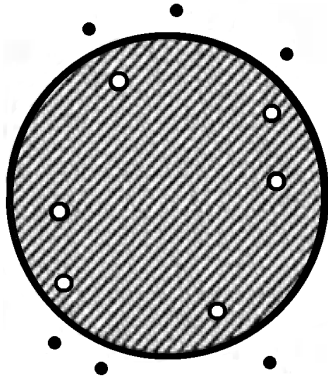


Figure 9: An illustration of the ground state of a conventional superconductor in momentum space. The shaded area within the large circle represents the Fermi surface in 2D and the solid (empty) dots represent occupied (unoccupied) electron states outside (inside) the Fermi surface. Even though the occupied electron states outside the surface have higher kinetic energy, the superconducting pairing potential lowers the overall ground state energy making such a configuration energetically favorable. The relative distance from the states to the Fermi surface is exaggerated for illustrative purposes. This figure is taken from[48].

The superconducting ground state consists of paired charge carriers. In order to break a pair, we need to create two excitations with their spectrum described by (2.1). This implies that breaking a Cooper pair would require the excitation of both constituent electrons beyond the gap, i.e., breaking a Cooper pair would cost an energy of at least  $2\Delta_0$ . Coming back to the question of how the Cooper pairs are protected from undergoing scattering events, we combine the knowledge on the surprising configuration of the superconducting BCS ground state and the excitation spectrum. Electrical resistance is due to the scattering of electrons as they get accelerated by an applied external electrical field over some distance (voltage). In a superconducting state, Cooper pairs are formed and breaking them would cost an energy of at least  $2\Delta_0$ , hence many scattering events are energetically insufficient to break them. The inability to scatter Cooper pairs gives rise to superconductivity.

#### 2.1.4 Quasiparticle excitation spectrum

The excitation spectrum introduced in the previous section can be phrased more formally using the notion of quasiparticles. Studying superconductivity in this setting will prove useful for later analyses, especially when we will consider scattering events and for instance topology. Until now we considered the elementary excitations in superconductors as electron states either

being occupied or empty. In this section we will define the notion of electron- and hole-like quasiparticles. First we introduce holes by considering a normal metal, then we generalize this to the more complex superconducting case.

In case of a normal metal the ground state at zero temperature is as sketched before, all states within the Fermi surface are occupied and all those outside are empty. Suppose we add an electron to the system. The only available states are those with momenta,  $k_+ > k_f$ , outside the Fermi surface. This condition on its momentum yields a positive energy increase, relative to the Fermi energy, for the total electron system of  $(\hbar^2\mathbf{k}_+ - \hbar^2\mathbf{k}_f) / 2m$ . We measure the energy relative to the Fermi level, so the excitation will have an energy equal to this increase and the system a momentum equal to  $\mathbf{k}_+$ . We can consider this as an electron excitation.

Now suppose the metallic ground state, as described above, but we prepare it with an electron from a state  $k_- < k_f$  removed. The total system lost  $\mathbf{k}_-$ , so we can see this is an excitation of momentum  $-\mathbf{k}_-$ . This configuration is not in its lowest energy state, there is some 'extra energy', namely, an electron from the Fermi surface at  $\mathbf{k}_f$  can for instance now move to this empty state at  $\mathbf{k}_-$ . The moved electron has gained an energy of  $(\hbar^2\mathbf{k}_f - \hbar^2\mathbf{k}_-) / 2m$  by doing so. We can therefore consider the initial configuration with a hole present within the Fermi surface as being excited since it has a greater energy than the lowest energy configuration of the remaining electrons in the metal. That is, the restored system where an electron  $\mathbf{k}_f$  went to  $\mathbf{k}_-$  has a lower energy. Hence the configuration with an electron removed from the ground state can be considered as an excitation with an energy equal to this difference and a momentum equal to  $-\mathbf{k}_-$ . Since this excitation behaves as an 'absent electron' and has a positive charge we shall refer to it as a hole.

In case of a superconductor the ground state is as illustrated in figure 9 and described in section 2.1.3. Suppose we add an electron with momentum  $\mathbf{k}$  to it. Since there are empty available states both above and below the Fermi level it will occupy one of the vacant states either with  $k < k_f$  or  $k > k_f$ . This will however leave the originally paired state at  $-\mathbf{k}$  unoccupied. Contrary to a normal metal, an electron-like quasiparticle (excitation) in a superconductor can either be inside or outside the Fermi surface due to the nature of the superconducting ground state. Now consider the superconducting ground state but with an electron removed from the state  $-\mathbf{k}$ . Consequently, the initially paired complementary state at  $\mathbf{k}$  uncouples. The uncoupled electron will start to act as a hole with momentum  $\mathbf{k}$ . As for the electronlike quasiparticle this hole-like excitation can either be inside or

outside the Fermi surface. Combing these two results gives us that the elementary excitation of a superconductor for a state  $\mathbf{k}$  being occupied and the corresponding state  $-\mathbf{k}$  being vacant is a combination of electron- and hole-like behaviour.

To formalize the concept of quasiparticle excitations we introduce two related functions of  $\mathbf{k}$ ,  $v_{\mathbf{k}}$  and  $u_{\mathbf{k}}$ , which are vital in the formal treatment of BCS theory. Let  $v_{\mathbf{k}}$  be the function such that  $v_{\mathbf{k}}^2$  gives the probability that the pair state  $(\mathbf{k}, -\mathbf{k})$  is occupied, and  $u_{\mathbf{k}}$  such that  $u_{\mathbf{k}}^2$  denotes the probability that it is unoccupied. Since the total probability should be unity, these functions are related by

$$u_{\mathbf{k}}^2 = 1 - v_{\mathbf{k}}^2. \quad (2.3)$$

Since a hole-like quasiparticle requires a state  $\mathbf{k}$  to be initially occupied, the probability that a quasiparticle acts hole-like is proportional to  $v_{\mathbf{k}}^2$ . Conversely its electron-like behaviour should be proportional to the probability that the state that  $\mathbf{k}$  is vacant, i.e., proportional to  $u_{\mathbf{k}}^2$ . The mixing of these two notions becomes most apparent as  $v_{\mathbf{k}}^2$  and  $u_{\mathbf{k}}^2$  become of similar size. Moreover, the behavior of the quasiparticle becomes purely hole-like or electron-like as  $v_{\mathbf{k}}^2$  or  $u_{\mathbf{k}}^2$  tends to unity, respectively. It can be shown that in BCS theory[48]

$$v_{\mathbf{k}}^2 = \frac{1}{2} \left( 1 - \frac{\varepsilon_{\mathbf{k}}}{E_{\mathbf{k}}} \right), \quad u_{\mathbf{k}}^2 = \frac{1}{2} \left( 1 + \frac{\varepsilon_{\mathbf{k}}}{E_{\mathbf{k}}} \right). \quad (2.4)$$

where  $\varepsilon_{\mathbf{k}} = (\hbar^2 \mathbf{k}^2 - \hbar^2 \mathbf{k}_f^2)/2m$  and  $E_{\mathbf{k}}$  is as in (2.1). We note that as  $\mathbf{k} \rightarrow 0$  we see that  $\varepsilon_{\mathbf{k}} \rightarrow -\hbar^2 \mathbf{k}_f^2/2m$  and  $E_{\mathbf{k}} \rightarrow \hbar^2 \mathbf{k}_f^2/2m$  (since typically  $\hbar^2 \mathbf{k}_f^2/2m \gg \Delta_0$ ), thus  $v_{\mathbf{k}}^2 \rightarrow 1$  and  $u_{\mathbf{k}}^2 \rightarrow 0$ . Indeed these excitations deep inside the Fermi surface, beyond a distance  $\Delta_{\mathbf{k}}$  from the Fermi surface, are hole-like and thus  $u_{\mathbf{k}}^2$  dominates over  $v_{\mathbf{k}}^2$ . Similarly using (2.3) and (2.4) we can show the limiting behavior for  $v_{\mathbf{k}}^2 \rightarrow 1$  for excitations well beyond the Fermi surface for the electron-like states. Finally, we note for states on the Fermi surface,  $\mathbf{k} = \mathbf{k}_f$ , that  $v_{\mathbf{k}}^2 = u_{\mathbf{k}}^2 = 1/2$  and the quasiparticle states are equally electron- and hole-like.

Figure 10 illustrates the differences between these specified electron-like and hole-like quasiparticle branches. On the left we see the known metallic quadratic dispersion, and on the right we include the dispersion relation for a superconductor in case the coupling term  $\Delta_0$  is nonzero. Notable features are the opening of a gap in the dispersion around the Fermi level, taken at zero energy in this figure, and the transition from an electron-like to a hole-like behavior for a single branch as seen in the top green curve. We also indicate the limiting behavior in the electron-like versus hole-like nature

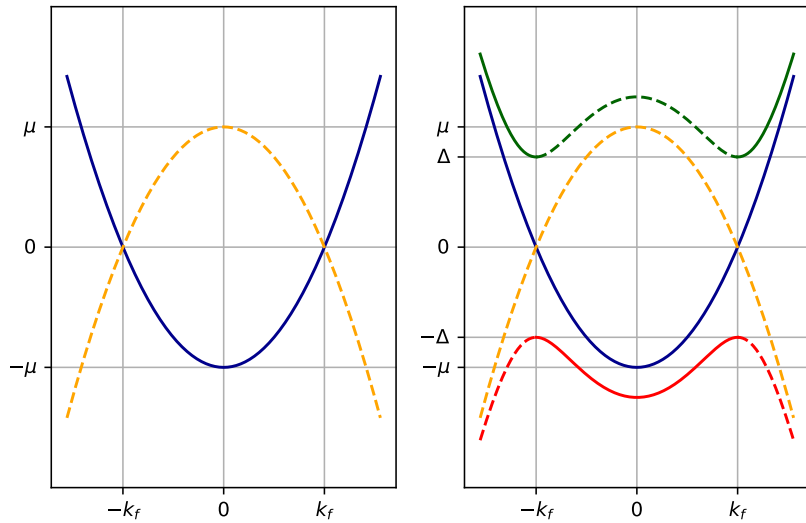


Figure 10: A figure showing the quadratic dispersion relation for a metal ( $\Delta_0 = 0$ ) on the left and the dispersion relation for a superconductor ( $\Delta_0 > 0$ ) together with the quadratic dispersion on the right. We consider the projection onto a single  $\mathbf{k}$  component on the  $x$ -axis, and energy on the vertical axis. A shift of  $-E_f$  is taken to place the zero energy point at the origin, and a nonzero chemical potential  $\mu$  is assumed. The solid and dashed lines indicate an electron- and hole-like branch respectively. The superconducting dispersion relation shown corresponds to (2.1). Note that the relative size of the superconducting gap is increased to highlight the notable features of the dispersion.

of our quasiparticles either for large or small momenta. A particular point of interest is around  $k \approx \pm k_f$ , because here our quasiparticles are equally electron- and hole-like. This specific phenomenon is one of the key ingredients why superconductivity might be a fruitful route towards the realization of Majorana modes. Since Majorana modes are, loosely speaking, defined as 'particles' that are their own anti-quasi-particles, the specific excitations at this inversion point where our quasiparticles are equally electron- and hole-like satisfy one of the agreed requirements listed in section 1.2 that  $\gamma = \gamma^\dagger$ .

Lastly, we consider the propagation direction in real space which is given by the group velocity of the quasiparticle

$$\mathbf{v}_g = \frac{1}{\hbar} \nabla_{\mathbf{k}} E_{\mathbf{k}}, \quad (2.5)$$

i.e., gradient of the dispersion relation w.r.t. the momentum  $\mathbf{k}$ . For electron-like quasiparticles the group velocity is in the same direction as the  $\mathbf{k}$ -vector. Consider for example an electron-like positive energy excitation with a positive momentum greater than  $k_f$ , i.e., on the upper right part of the solid

green line in figure 10. The group velocity, defined as the derivative of the curve, is in the same direction as the momentum. This holds true for all electron-like quasiparticles. Contrary, the hole-like quasiparticles propagate opposite to their momentum. For instance hole-like quasiparticles populating the upper right part of the dashed green curve have a positive momentum but move towards the left. This difference is of interest when studying (Andreev) scattering phenomena next.

## 2.2 Andreev reflections

Given a superconductor's (quasiparticle) excitation spectrum in BCS theory as discussed in section 2.1.4 we can study the phenomenon called Andreev reflection and the possible occurrence of a phase-coherent bound state resulting from the Andreev reflections called an Andreev bound state. The relevance of Andreev bound states in this thesis is based on the previously mentioned prediction by Fu and Kane [1] on the possible existence of Majorana state in the form of an Andreev bound state at the interface between a magnetic and superconducting topological insulator. We first introduce Andreev reflections (AR) by considering a simple interface between a normal metal and a superconductor. Please note that AR can equally well occur at an interface in a system consisting of a topological insulator rather than a normal metal. After the discussion of AR, the formation of Andreev bound states (ABS) are discussed before explaining multiple Andreev reflections (MAR). These three phenomena are treated in [48],[58] and [59].

In 1964 the Russian theoretical physicist Alexander F. Andreev[60] was the first to accurately describe the reflection that occurs at the interface between a normal metal and a superconductor (NS-interface). In short, an Andreev reflection is the spin conserved charge transfer of  $2e$  from a normal metal to a superconductor through the retroreflection of an electron (hole) to a hole (electron). Figure 11 shows Andreev reflection in real space. In the figure, an incoming spin-up electron from N with an amplitude of 1 is retroreflected ( $\theta \rightarrow \pi + \theta$ ) as a hole with spin down, and a spin-up electron is transmitted. The process seems to violate charge conservation, but this will be addressed shortly. The reflected hole moves anti-parallel to the initial electron, but a hole's momentum is opposite to its direction of motion, so momentum is conserved in AR. Moreover, since a hole is considered as an absent electron, the reflected spin-down hole describes the same spin as the initial electrons, i.e., spin is conserved. AR is different from normal reflections, where the spin and particle type (thus charge) are conserved, but momentum is not. In normal reflections, the horizontal momentum gets in-

verted ( $\theta \rightarrow \pi - \theta$ ), but the vertical momentum is unchanged. To understand the reason why AR occurs and its details we first introduce the proximity effect and describe the NS-interface in more detail.

As described and seen in figure 6 in section 2.1.1, the proximity effect is the simultaneous suppression of the order parameter in a superconductor (S) and the increase of it in a normal metal (N) in the vicinity of an N-S interface. In the language of BCS theory, the proximity effect can be explained by considering the interface between a normal metal (N) and a superconductor (S) in 2D and the mechanical interface at  $x_0$ . The Cooper pairs from S penetrate into N and remain paired for a while, causing the formation of a thin superconducting layer near  $x_0$ . As the paired Cooper pairs leak from S into N, their local density drops on the S side and as a result, the order parameter drops. This drop is referred to as the proximity effect and occurs over the characteristic coherence length scale  $\xi$ . Along with the drop in the order parameter, the effect the superconducting energy gap has on the system (and hence dispersion) also decreases the further we move from S into N. Deep inside S,  $\Delta(x \gg x_0) = \Delta_0$ , and deep in N,  $\Delta(x \ll x_0) = 0$ . The superconducting gap is continuously increased from zero, as  $x$  approaches  $x_0$ , and reaches  $\Delta_0$  deep inside S. We can define the NS-interface as the region in which these transitions of the order parameter and the superconducting gap occur.

Now we can study the scattering process in more detail by considering the Andreev reflection in figure 12 step by step in momentum space. Each panel in figure 12 is a snapshot, in momentum space, of the process. The drawn curves are the positive energy parts of the dispersion relations displayed in figure 10. Per panel, we indicate a (quasi)particle, an electron- or hole-like (quasi)particle is indicated by a filled or empty circle respectively with an arrow indicating the spin orientation.

An incoming electron with energy  $E$  populates a state with positive  $k$  and positive group velocity. As the electron moves towards the NS interface, the proximity effect causes the electron to start to experience the effect of the superconducting gap on its dispersion, effectively transitioning the particle to a quasiparticle. The quasiparticle gradually becomes more and more hole-like due to the strengthening effect of the superconducting gap. Moreover, its group velocity reduces until it becomes zero when the superconducting energy gap equals the initial energy  $E$  at  $k_f$ . It is at this point that the quasiparticle moves to the hole-like branch with positive momentum, but with a negative group velocity, so it starts to move away from the interface

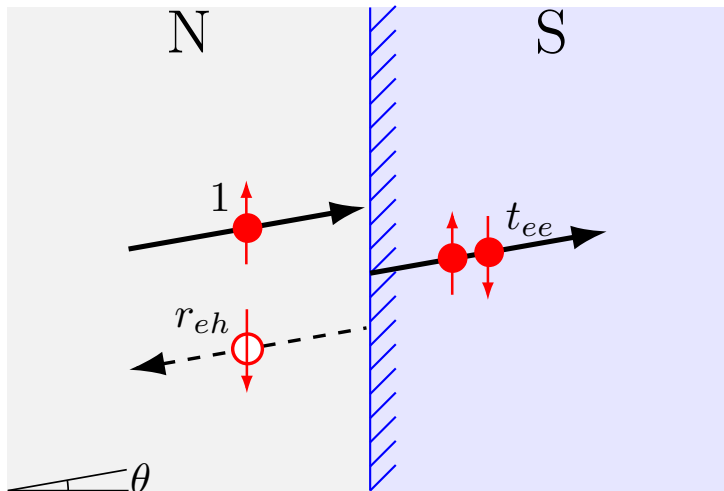


Figure 11: A figure illustrating, in real space, the Andreev scattering of an incoming spin-up electron from a normal metal (N) with amplitude 1 travelling under an angle  $\theta$  to a spin-down hole with amplitude  $r_{eh}$  whilst transmitting a spin-up electron with amplitude  $t_{ee}$  to a superconductor (S). The solid (empty) circles correspond to electron-like (holes-like) quasiparticles. The retroflected hole is reflected with an angle of  $\theta + \pi$ . The second spin down electron in the superconducting material is drawn to illustrate the fact that the incoming electron found itself an appropriate partner to form a Cooper pair with.

in opposite direction. We know however that a positive charge propagating to the left is equivalent to a negative charge propagating to the right. Hence we have described the  $2e$  charge transfer from an incoming electron retroflected by the NS interface as a hole, this process is called the Andreev reflection. For completeness, we also mention here that at an NS interface also branch-crossed transmission can occur as described in [3].

When looking critically at the discussion of the Andreev reflection above one might argue that charge is not conserved in this process, however the so-called condensate[48] in the superconductor remedies this. The condensate is the name given to the collection of Cooper pairs in the superconductor. The superconducting spectrum we considered in the dispersion relation in (2.1) and correspondingly figure 10 is the spectrum of particles that get excited from this condensate. This condensate is by no means static, continuously Cooper pairs are broken and formed again through phonon mediated scattering. What happens during Andreev reflection is that the incoming spin up electron with positive momentum transforms to a spin-up hole with positive momentum as described in figure 12. The interaction with the condensate can be seen as the initial electron pairing up with a spin down electron with

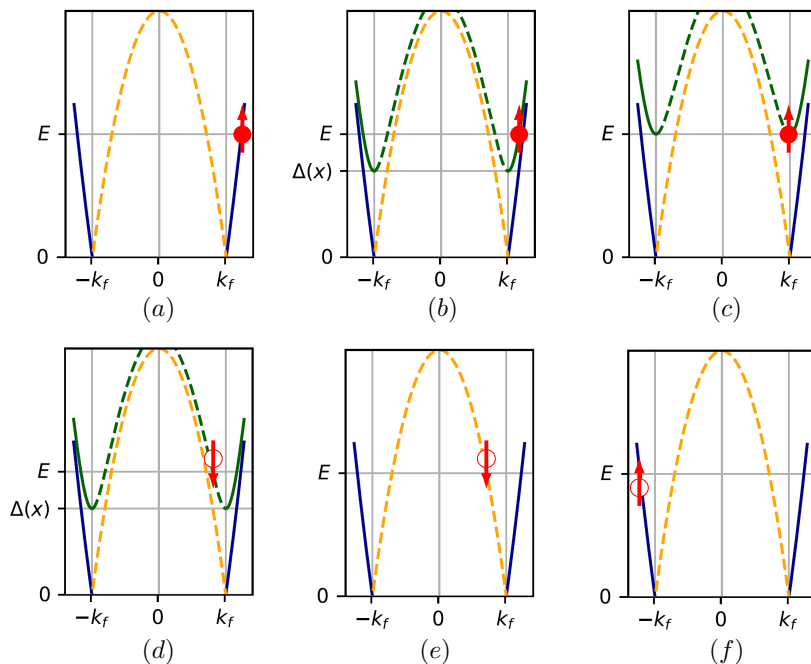


Figure 12: A figure illustrating, in momentum space, the Andreev scattering of an incoming electron to a hole. The drawn curves are the positive energy half of figure 10. The solid (empty) circles correspond to electron-like (holes-like) quasiparticles. The two indicated energies are the incoming electron's energy,  $E$ , and the value of the superconducting gap,  $\Delta(x)$ , as a function of the distance,  $x$ , the incoming particle has travelled into the NS junction. Initially, the electron in the normal metal obeys a metallic dispersion with a positive group velocity (a). As it moves towards the superconductor it starts to experience the effect of the superconducting energy gap, and its dispersion becomes that of a, mostly electron-like, quasiparticle and its group velocity drops (b). This effect strengthens until the quasiparticle becomes equally electron- and hole-like and its group's velocity vanishes (c) and it gets reflected. Now the quasiparticle moves onto a more hole-like branch with a negative group velocity (d). The hole-like quasiparticle moves (far) away from the interface and becomes a metallic hole excitation (e). The final panel emphasizes the equivalence between an excited spin-down hole with positive momentum and a vacant spin up negative momentum state in the electronic dispersion branch.

negative momentum in the superconductor to form a Cooper pair, as seen in figure 11, effectively leaving behind a vacancy in the electron branch in at the spin-up state with negative momentum. From the entire state's perspective, this vacancy is equivalent to an excited hole with opposite spin and momentum, i.e. the reflected spin-down hole with positive momentum. This last equivalence is depicted in the figure 11.f.

### 2.2.1 Andreev bound state

Suppose we now consider a system consisting of more than one interface of which at least one is superconducting. At the superconducting interface, Andreev reflections occur and at the other interface(s) different types of reflection take place (e.g. normal reflection). Due to these consecutive reflections, charge carriers scatter back and forth between the interfaces and an Andreev bound state can form (ABS). Since a bound state opens up a resonant channel for charge conduction, an ABS occurring for some certain energy and parameter range will result in increased conduction at that energy.

To illustrate Andreev bound states (ABS) we consider a system consisting of a slab of 2D normal metal in contact with a ferromagnetic insulator on the left and a superconductor on the right, as depicted in figure 13. In the figure, we illustrate the possible reflection and transmission paths in an F-N-S junction. At the ferromagnetic insulator side normal reflection is possible ( $\theta \rightarrow \pi - \theta$ ) for both electrons and holes, and at the normal metal-superconductor interface AR occurs ( $\theta \rightarrow \pi + \theta$ ). The possibility for an incoming particle to undergo normal or Andreev reflection at the N-S interface depends on various parameters such as the superconducting energy gap and the chemical potential. This means that the system can be engineered such that AR are more favourable. Upon each reflection, an incoming wavefunction gains a complex phase.

In the FNS system, ABS occurs when we form a phase-coherent 'closed loop'. We start our loop at for instance the right travelling electron wavefunction, labelled by  $r_{ee}^F$ , inbound on the N-S interface under angle  $\theta$ . The right travelling electron undergoes AR, the resulting hole ( $r_{eh}^S$ ) travels in the negative  $x$ -direction towards the F-N interface. At the interface, the hole normal reflects and moves back towards to N-S interface ( $r_{hh}^F$ ). There, the hole Andreev reflects to an electron ( $r_{he}^S$ ) moving in the negative  $x$ -direction. To close the loop a final normal reflection brings us back to  $r_{ee}^F$ . The closed-loop is phase-coherent when the phase gain by the consecutive reflection

processes is an integer multiple of  $2\pi$ , when the width is sufficiently small we can safely ignore the phase gain due to propagation. The idea that phase coherence gives rise to resonances is similar to the principal giving rise to resonant tunnelling in ballistic double barrier normal metal junctions[61], [62].

Given the expressions for the reflection coefficients depicted in figure 13, then mathematically speaking phase coherence occurs when the sum of the phase gains associated with each reflection is an integer multiple of  $2\pi$ , this is called the Bohr-Sommerfeld quantization [63][64]. We formulate the Andreev bound state's phase coherence condition as follows

$$\alpha_{r_{eh}^S} + \alpha_{r_{hh}^F} + \alpha_{r_{he}^S} + \alpha_{r_{ee}^F} = 2n\pi, \quad n \in \mathbb{Z}, \quad (2.6)$$

where  $\alpha_{r_{ij}^m} := \arg(r_{ij}^m)$  is the phase gain<sup>7</sup> under the reflection from a particle  $i$  to a particle  $j$  at the interface between a normal metal and a material of type  $m$ .

In the coming section (2.3) topological insulators will be introduced, but the description of ABS the FNS system described above still hold in a 2D system consisting of topological insulators. To reiterate, the relevance of the ABS in these systems is due to the prediction[1] that Majorana states could emerge in the form of zero energy Andreev bound states, called zero-energy Majorana bound states (ZEMBS).

### 2.2.2 Multiple Andreev reflections

Consider a symmetric Josephson junction consisting of two superconducting leads, one left and one right, connected by some link. In such systems, multiple Andreev reflections (MAR) can occur. MAR is possible in both a normal metal and a topological material in contact with a superconductor on either side. The study of MAR has a rich history in the field of superconductivity, see for instance the work by Blonder Tinker and Klapwijk [65], or [41][58]. To explain the physical origin of MAR we follow [65]. Consider a normal metal with a constriction with on either side a superconducting lead attached such that we can apply a voltage  $V$  over the superconducting leads. The middle constriction acts as a tunnel barrier between the two leads. A schematic illustration is given in figure 14. Here we show the density of states in the superconductors in  $(E, k)$  space as well as some reflected charge

---

<sup>7</sup>Note that for  $z \in \mathbb{C}$ ,  $\arg(z) = \text{atan2} \frac{\Im(z)}{\Re(z)}$  where  $\text{atan2}$  is four-quadrant adaption of the inverse tangent. This detail is important in numerical implementation, every known programming language has an implementation of the four-quadrant inverse tangent.

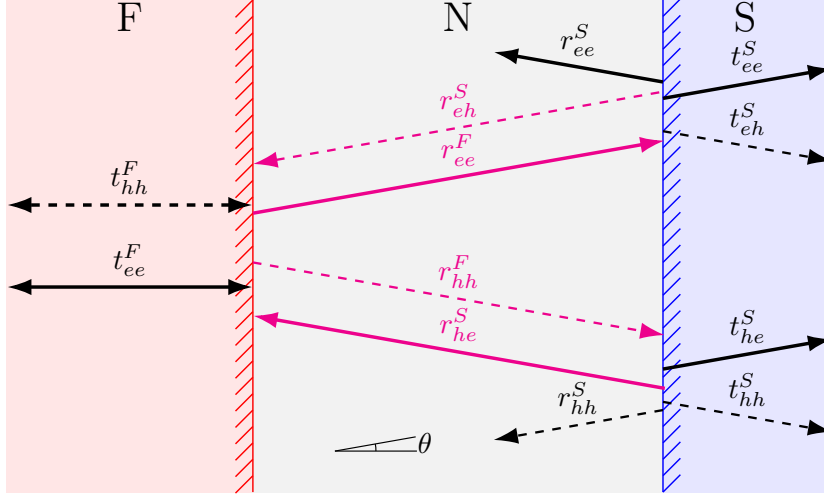


Figure 13: This figure illustrates the possible types of reflections occurring in a ballistic 2D F-N-S junction between a ferromagnetic insulator (F), normal metal (N), and s-wave superconductor (S). The solid and dashed lines refer to electron and hole wavefunctions respectively. The indicated angle  $\theta$  is defined for electrons positive x-direction respectively. The (first-order) ABS is indicated by the magenta-coloured reflection coefficients and wavefunctions in the middle normal metal. At the ferromagnetic insulator side, normal reflection for both electrons and holes can occur, whereas at the superconductor side both normal and Andreev reflections are possible.

carriers. The tunnel barrier is omitted in the figure. The narrow line drawn at  $E = 0$  illustrates a (potential) finite density of states at zero energy, the superconductors' continuum levels are an energy of  $\Delta_0$  away from zero.

Let us now concentrate on an electron injected from the left S into the normal metal at an energy  $E$  when applying a finite bias energy  $eV$ . Passing through the device along with the voltage drop, it gains energy  $eV$  from the applied electric field, and (Andreev) reflects at the NS interface. Upon Andreev reflection, at the NS interface, it returns as a hole, so the sign of its charge has switched and the hole gains another  $eV$  by retraversing the field. A similar reflection process will occur at the left SN interface. Then, by iteration of this process, Andreev reflection provides a way to gain arbitrarily large integral multiples of  $eV$  from the field.

When two occupied density of states levels align, current can easily flow through the system and steps in conduction will occur. We shift the energy scale of the two superconductors with respect to each other by changing the bias voltage. So by tuning the bias voltage, we can study the location of energy levels in the system. For instance when we apply a bias of  $eV = 2\Delta_0$ ,

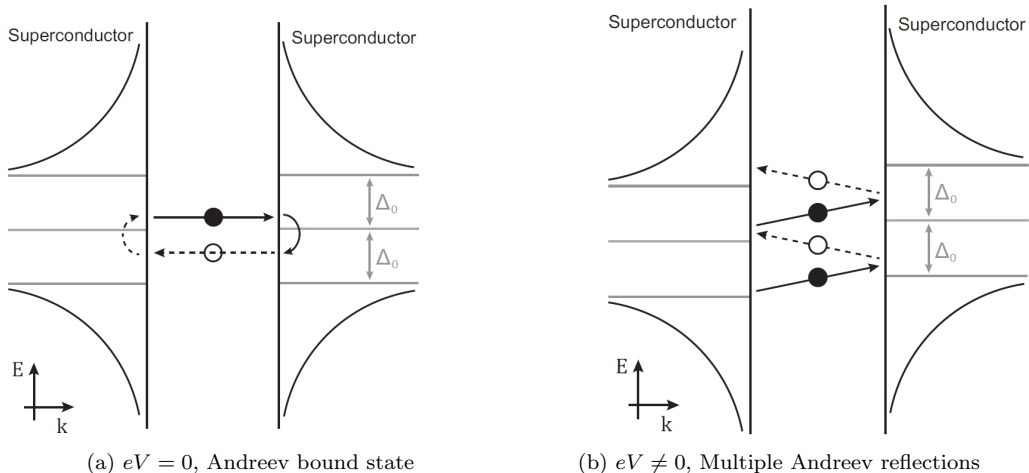


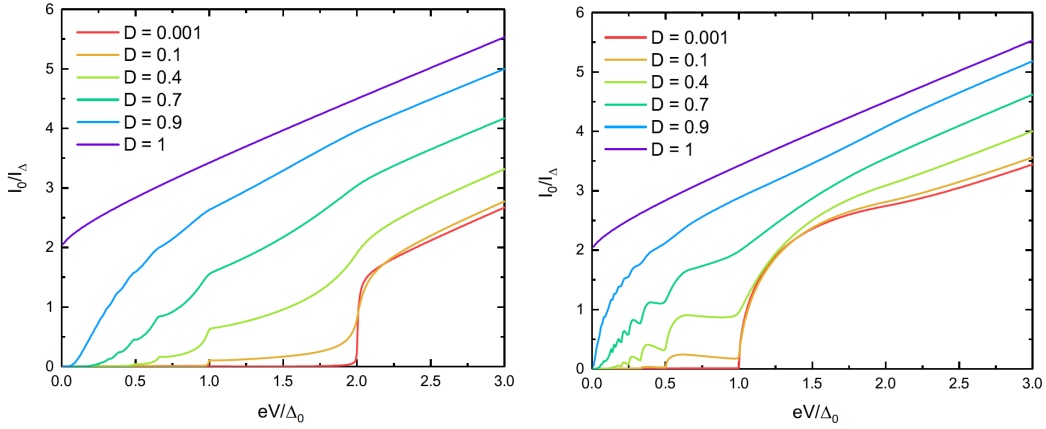
Figure 14: Reflections in between two superconductors are shown in  $E, k$  space. The superconductor's continuum density of states levels are shown. Solid (open) circles represent electrons (holes). The left image shows the situation for a zero bias voltage applied over the two superconductors, the right image shows the finite voltage case. When a bias voltage is applied an electric field is set up, and the charge carriers gain energy when traversing the field. Image courtesy of Linde Olde Olthof [46].

the the continuum levels align and current can easily flow. MAR actually opens the potential for the rich structure superimposed on a smooth background for voltages  $eV \leq \Delta_0$ . Distinct steps are easily seen in the differential resistance at integral submultiples of the gap. This phenomenon is referred to as the sub-gap structure[65].

To illustrate of the effect of MAR on the conduction potential  $I, V$  curves for a topological system without and with a structure at  $E = 0$  are shown in figures 15.a and b. The left hand figure shows steps in the conduction when.

$$eV = \frac{2\Delta_0}{n}, \quad n \in \mathbb{N}. \quad (2.7)$$

Consider an electron from the left superconducting lead undergoing MAR in a system with an absent DOS at  $E = 0$ . When we apply a bias of  $2\Delta_0$ , the continuum levels align and the electron gains sufficient energy to enter the right superconductors continuum level. The reason for the integer submultiple modes is that the charge carriers climb in energy, and when the energy gain after  $n - 1$  Andreev reflections is  $n \times 2\Delta_0/n$  its energy aligns with that of the continuum level at the other lead and it can conduct. This process repeats and we get steps in the conduction as seen in figure 15a at the biases indicated in (2.7). Since the spectrum corresponds to an absent structure in the DOS at  $E = 0$  we refer to this MAR spectrum as trivial.



(a) MAR  $I, V$  curve for no structure in the DOS at  $E = 0$ . (b) MAR  $I, V$  curve for a structure in the DOS at  $E = 0$ .

Figure 15: Normalized  $I, V$  curves for a system without and with a structure in the DOS at  $E = 0$ . The drawn curves are for various transparencies  $D$  of the middle barrier. Image courtesy of Linde Olde Olthof [46]

When we now do consider a structure in the DOS at  $E = 0$ , illustrated in e.g. 14, an  $I, V$  curve shows steps in the conduction for a bias of

$$eV = \frac{\Delta_0}{n}, \quad n \in \mathbb{N}, \quad (2.8)$$

as seen in figure 15b. We shall refer to this as a non-trivial MAR spectrum. The origin of these steps is explained analogously to the steps in figure 15a, however now we already have a finite DOS at both sides at  $E = 0$ . So for an initial electron in the left superconductor only half the energy gain as compared to the previous case is required for the electron's energy to align with a nonempty level in the DOS on the other side. The same can be said for higher-order consecutive AR. Hence the same procedure explained above now clarifies the resonances at biases of  $eV/n$ , for details the reader is referred to [45]. So by studying the  $I, V$  curve of a (symmetric) junction, we can probe the structure in the DOS at  $E = 0$ .

## 2.3 Topological insulators

The cornerstone prediction by Fu and Kane [1] on the existence of a chiral Majorana mode propagating on the surface of an  $s$ -wave induced topological insulator at the edge along a magnetic topological insulator required the materials to be topological. Having discussed superconducting materials, we now introduce the concept of topological insulators (TI). In short a TI is a material that is intrinsically insulating in the bulk, but conducting on the surface. So a 3D topological insulator, such as  $\text{Bi}_2\text{Se}_3$  or  $\text{Bi}_2\text{Te}_3$  [30] or  $(\text{Bi}_{0.4}\text{Sb}_{0.6})_2\text{Te}_3$  thin films [66], would be insulating in its core, but conducting on its outer 2D surface. This is clearly different from either the properties of a normal metal that is conducting everywhere or a regular insulator that is insulating everywhere. A great layman (for a mathematician or non condensed matter physicist) introduction to TIs is given in [67], an extensive review is given in [68], and for an advanced course book the reader is referred to [69].

In this section we globally explain the origin of the peculiar nature of the TI's edge conductance by drawing the analogy to the quantum hall effect, we give references where more technical details are required. This introduction is followed by a discussion on the modelling of magnetic and superconducting magnetic (MTI) and superconducting topological insulators (STI).

### 2.3.1 TI edge states analogy to QHE

As the name suggests, a topological insulator is mostly insulating, but allows for some form of conduction related to its topology. The notion of topology is reserved for a so-called topological invariant, i.e., a property of a geometric shape that does not change when the shape is stretched or distorted. One such invariant is the genus  $g$ , which is given by the number of holes in the surface. Shapes with no holes in them ( $g = 0$ ) are all considered topologically equivalent, as do the class of shapes with one hole in them ( $g = 1$ ) [67]. The (over)used example is the topological equivalence between the shape of doughnut and of a coffee mug, they both contain a single hole and can (in principle) be continuously deformed into each other without tearing a hole into the surface. Given a surface  $S$ , its genus is defined by the Gauss–Bonnet theorem,

$$\frac{1}{2\pi} \int_S K dA = n, \quad (2.9)$$

which says the integral over the curvature  $\kappa$  of an object is quantized. Here  $n$  is an integer related to the genus by  $n = 2(1 - g)$ . The discrete nature of the integer  $g$  reflects that we can not continuously change (deform) the genus of a surface since we can not continuously transform integers into each other. This means that the genus is topologically invariant under continuous deformations of the surface.

This notion of topology is all nice and well, but what has it to do with the conduction of charge? Consider now not the shape of a sample in real space, but consider the shape of its Brillouin zone in momentum space. The Brillouin zone is a periodic region in a crystal lattice describing all allowable electronic crystal momenta and is an important concept in the field (electronic) charge transport[70]. It can be shown [67] that an analogous version to the Gauss-Bonnet theorem in momentum space can be obtained,

$$\frac{1}{2\pi\hbar^2} \int_{\text{BZ}} \Omega d^2p = C, \quad (2.10)$$

where  $\Omega = \nabla \times \mathbf{X}$  is the curl of the so-called Berry connection  $\mathbf{X}$ .  $C$  is the Chern-number. Without going into details, the Berry connection is an intrinsic material dependent vector field and acts analogous as the magnetic vector potential [67]. In fact when applying an external electric field  $\mathbf{E}$ , electrons propagate perpendicular to both  $\mathbf{E}$  and to  $\Omega$ . This is exactly what happens for electrons in an electric and magnetic field. So we can consider the curvature of the Berry connectivity (Berry curvature for short) to act as an intrinsic magnetic field.

A more known derived quantity from the Berry connection is called the Berry phase. It is a geometric phase that does not depend on time and is given by the integral of the Berry connection along some path  $P$  in momentum space. Consider for example an electron getting accelerated and decelerated in a lattice such that it traverses a closed path returning back at its initial location. Even though the initial and final position are identical, the particle has acquired a complex phase called the Berry phase.

To explain the surface conduction in a TI, we further on the magnetic field analogy by considering the quantum hall effect (QHE)[37][61]. In the QHE a sample placed in a sufficiently strong external magnetic field has electronic states carrying current in one direction localized on one side of the sample, while those carrying current in the other direction are localized on the other side of the sample. This separation of the two opposing flows limits counter flow of charge carriers and back-scattering can not occur [61], giving rise

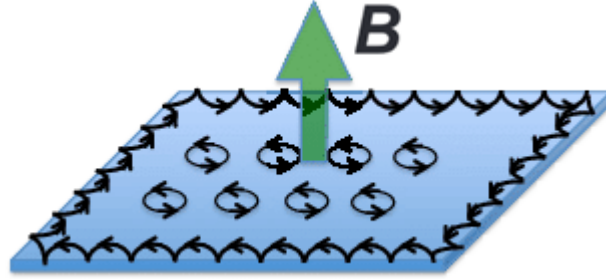


Figure 16: The quantum hall effect; the strong magnetic field  $B$  enforces electrons into Landau level with cyclotron motion and become localized in bulk while conducting at edges. Adapted from [71].

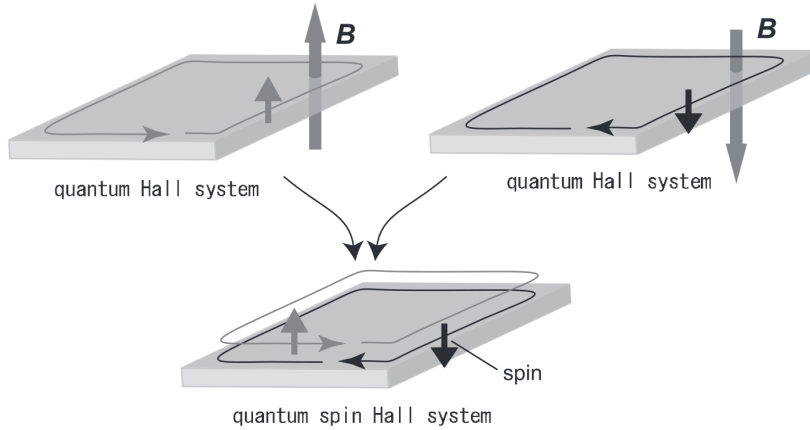


Figure 17: A schematic illustration of the quantum spin hall state as the superposition of two opposite quantum hall states that originate from applied external magnetic fields with opposite field directions. The image is taken from [72].

to clean ballistic conduction along the edge. For a sample in a sufficiently strong external magnetic field the QHE is explained by the electrons being forced into so-called closed Landau cyclotron orbits in the bulk, but taking half open skipping orbits electrons at the edge of the sample [72]. In figure 16 these two type of trajectories are shown. The localized closed orbits do not conduct any charge as they are localized (stationary), but the edge state do 'creep' up along the edge and conduct. This gives rise to the insulating character of the bulk and the conductive behavior of the edge states. In a TI the Berry curvature is the intrinsic material property that plays the role of the magnetic field in the QHE giving rise to the conducting edge states.

To bridge the last gap from the conducting QHE edge states analogy to a TI we need to consider the quantum spin hall effect (QSHE) to account for the

spin-momentum locking observed in a TI. In short we can consider the QSHE effect as a superposition of two QHE that arise from strong applied magnetic fields in two opposite directions acting on opposite spin orientations. The QSHE effect does not require an external magnetic field, a strong-spin orbit coupling in the material acts as an intrinsic magnetic field acting in opposite direction on edge states of opposite spin as illustrated in figure 17 [73]. The spin enters the equation here because the opposite spin orientations rather align parallel than the anti-parallel with the magnetic field, and this gives rise to the two counter-propagating spin orientations.

To answer the question what topological invariant is responsible for the edge states we consider what happens at the surface of a TI in contact with a topologically trivial material (i.e. normal insulator). The term surface here is ambiguous: in a 3D TI, the conducting states are the 2D surface state, whereas, in a 2D TI, the 'surface' states are the 1D edge state. A normal insulator has a band gap between its conduction('empty') and valence('filled') band, but a topological insulator has inverted band structure due to the spin orbit coupling [74]. Formally speaking the two materials are described by different  $\mathbb{Z}_2$  invariants<sup>8</sup>, 1 for the TI and 0 for the regular insulator [74]. The band structure can not be continuously deformed to go from the topologically trivial material (the insulator) with a band gap to the the inverted band gap in a TI due to this integer  $\mathbb{Z}_2$  invariant difference. As we close the band gap to invert the bands, we need to transform the  $\mathbb{Z}_2$  invariant integer from 0 to 1, this is not allowed (similar to how we're topologically not allowed to cut a hole in a pizza to deform it into a doughnut). The surviving metallic edge states in a TI are therefore said to be topologically protected. The surface states are protected by time-reversal symmetry, and are robust against non-magnetic disorder and perturbations[75].

We close this brief introduction to the origin of the conducting spin-locked edge states in a TI by showing an effective Hamiltonian for a TI describing spin orbit coupling,

$$h_{TI} = v_f \mathbf{p} \cdot \boldsymbol{\sigma} - \mu \sigma_0, \quad (2.11)$$

where  $\boldsymbol{\sigma} = (\sigma_x, \sigma_y, \sigma_z)$  are the canonical Hermitian unitary Pauli spin matrices [25] and  $\sigma_0$  is the two dimensional identity matrix. The first term introduces spin orbit coupling (also called Rashba coupling [77]) where  $v_f$  is the Fermi velocity and  $\mathbf{p}$  is the momentum. The second term sets the

---

<sup>8</sup>This  $\mathbb{Z}_2$  invariant can be seen as the number of times the band structure intersects the Fermi energy mod 2[68]. Thus for a band gapped insulator no bands cross the Fermi energy, but for a TI, an edge state crosses the Fermi energy

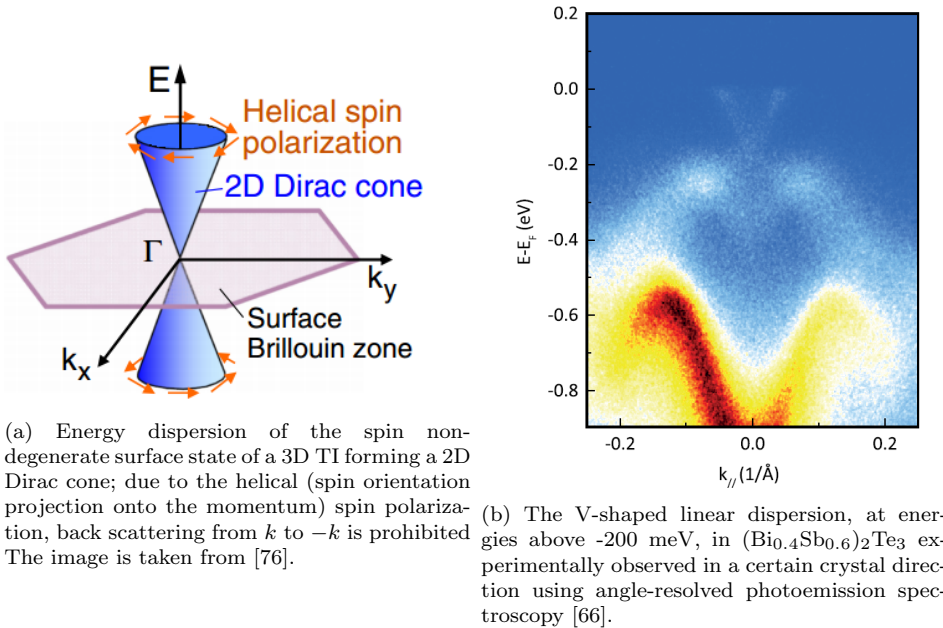


Figure 18: Local linear dispersion relation theory (a) vs experiment (b).

chemical potential,  $\mu$ . If we solve for the eigenvalues of the TI Hamiltonians in (2.11) (using plane waves  $e^{i\mathbf{k}\cdot\mathbf{r}}$ ) we get the well known TI's (local) linear dispersion relation.

$$E_{TI} = -\mu \pm \hbar v_f |\mathbf{k}|. \quad (2.12)$$

The dispersion relations describe two inverted cones in  $(E, \mathbf{k})$  space (see figure 18).

### 2.3.2 Magnetic and superconducting topological insulators

In the coming work we will consider the topological Josephson junctions consisting of a (magnetic) tunnel barrier. The system consists of a 3D TI with 2D surface states on top of which we induce regular  $s$ -wave superconductivity and ferromagnetism as shown in figure 3. In the region below the superconductor or ferromagnet the 2D surface states in TI become locally superconducting or ferromagnetic.

To elaborate on the superconducting topological insulator (STI) we consider an  $s$ -wave superconductor deposited on the TI's surface. At the interface, the proximity effect allows Cooper pairs to tunnel into the surface states. When we discussed Andreev reflections (section 2.2) we introduced the proximity effect. Mathematically speaking the effect of the induced

Cooper pairs introduces an attractive superconducting singlet pairing potential  $V = \Delta\psi_{\uparrow}^{\dagger}\psi_{\downarrow}^{\dagger} + h.c.$  to the Hamiltonian describing a TI (2.11)[1]. Here  $\Delta = \Delta_0 e^{i\varphi}$  depends on the superconducting phase  $\varphi$  of the superconductor. Later in chapter 3 when discussing the quantitative aspects in this thesis we formally introduce the STI's Hamiltonian and derive and solve the set of so-called Bogoliubov-de Gennes equations describing the wavefunctions in a (S)TI.

As mentioned, it is shown by Fu and Kane [1] that for a sufficiently small superconducting energy gap  $\mu \gg \Delta_0$  the low energy dispersion relation ( $E \sim \Delta_0$ ) of a STI resembles that of a spin-less  $p_x + ip_y$  superconductor,

$$E_{STI} = \pm \sqrt{\Delta_0^2 + (\mu_s \pm \hbar v_f |\mathbf{k}|)^2}. \quad (2.13)$$

This resemblance is particularly interesting in light of the observation that such a  $p$ -wave superconductor allows Majorana bound states [31]. We will show in section 3.2.4 that indeed, if we introduce  $s$ -wave superconductivity into the TI surface states that the resulting STI's dispersion resembles that of a spinless  $p_x + ip_y$  superconductor. In short, the induced  $s$ -wave superconductivity opens up a gap of size  $2\Delta_0$  in the linear TI dispersion relations (2.12) about the Fermi level. This is similar to the gap that opened up in a regular  $s$ -wave superconductor in figure 10.

Similar to the formation of a STI, we can construct a magnetic topological insulator by inducing ferromagnetism into the surface states. The TI below the F becomes a ferromagnetic insulator due to the exchange coupling[38]. We model the MTI by introducing a Zeeman gap due to an induced magnetisation  $\mathbf{m}$  in the TI Hamiltonian (2.11)

$$h_{\alpha\beta} = v_f \mathbf{p} \cdot \boldsymbol{\sigma} - \mu_m \sigma_0 + \mathbf{m} \cdot \boldsymbol{\sigma}, \quad (2.14)$$

the final term is added to study the effects of an induced ferromagnetic effect, note that  $\mathbf{m} = (m_x, m_y, m_z)$  is the magnetization vector with each  $m_i$ , for  $i = x, y, z$  having units of energy. In this work we consider the case that magnetisation only has a component  $m_z$  along the  $z$ -axis. The effect of the induced magnetism is the opening of a gap  $m_z$  about the chemical potential in the MTI  $\mu_m$

$$E_{MTI} = -\mu_m \pm \sqrt{m_z^2 + \hbar^2 k_y^2 v_f^2}, \quad (2.15)$$

where we have taken the momentum projection onto the  $k_y$  direction. Again we will show this formally using the Bogoliubov-de Gennes equations in chapter 3. We note that for a sufficiently large  $m_z$ , the MTI shows a band gap

about  $-\mu_m$ . Note that this magnetic energy gap is different from the superconducting gap that opens about the Fermi level  $E_f$ . The band gap creates a so-called forbidden region. Incoming particles in this range will thus often reflect from the barrier, but can tunnel through with an exponentially decreasing probability. Thus the MTI acts as an insulator because incoming charges in the energy range of the band gap will scatter from the MTI.

We conclude this section by comparing the energy scales of the relevant material properties in the three dispersion relations (2.12), (2.13), and (2.15). We consider the chemical potential  $\mu$ , the superconducting energy gap  $\Delta_0$  and the magnetic energy gap  $m_z$ . The superconducting energy gap's critical temperature dependence was given in (2.2). Considering that the critical temperatures of *s*-wave superconductors in figure 5 are  $\sim 15\text{K}$  we have that  $\Delta_0 \sim 2\text{meV}$ . We should however note that in a STI we induce superconductivity through the proximity effect, this value drops by roughly a factor 10 due to contact transparency effects. Thus we get that the induced superconducting gap in a STI is of the order  $0.1\text{meV}$ . An extensive survey of MTIs is given in [78] and shows that a reasonable high estimate of the magnetic band gap in a MTI is of the order  $m_z \sim 30\text{meV}$ . Lastly an estimate of the chemical potential is  $\mu \sim 100\text{meV}$ . More importantly we can assume that we can control the chemical potential, by using gating voltages for instance, with a sensitivity of  $\sim 10\text{meV}$ . The proposed exciting Majorana physics [31],[1] requires  $\mu \gg \Delta$  which is indeed possible, and we would like the MTI to be mostly insulating, i.e. the magnetic energy gap should be larger than the chemical potential in the MTI:  $m_z > \mu_m$ . This is in the realm of possibilities if we tune  $\mu_m \sim 10\text{meV}$  and have a  $m_z \sim 30\text{meV}$ . Finally, we work with energies in the sub-gap  $|E| \leq \Delta_0$

### 3 Re-deriving and solving the Bogoliubov-de Gennes equations

In this thesis, we model the physics governing the behaviour of charge carriers in a system comprising of (multiple) junctions between magnetic, superconducting and/or topological materials using the Bogoliubov-de Gennes equations. In the rich field of superconductivity, there is however a wide variety of models used to provide theoretical predictions. Each come with their own set of underlying assumptions and resulting limitations. The choice of model is therefore dependent on the system-specifics (type of superconductor, geometry, etc) as well as on a wide range of other parameters such as the temperature or the impurity of the system (dirty or clean conduction). We first discuss why the Bogoliubov-de Gennes equations are applicable for the systems and energies considered in this work by comparing them to alternative approaches. Then we formally introduce and derive the Bogoliubov-de Gennes equations and solve them in material-specific cases.

A phenomenological theory already mentioned in section 2.1.1 is the Ginzburg-Landau theory, with an associated set of equations. Briefly stated the Ginzburg-Landau equations are a set of equations derived by minimizing the free energy of a superconducting material placed in a magnetic field with respect to the order parameter  $\psi(\mathbf{r})$ . Please see [48] chapter 3 for a detailed discussion. The coupled set of equations provides a phenomenological description of the behaviour of the superconducting charge carriers and the magnetic field inside a superconducting material. The Ginzburg-Landau equations can be studied (numerically) to provide insight into the dynamics of the magnetic fields generated by a superconductor. This is of great importance in, for instance, the realization of super strong magnets. However, since it is not a microscopic theory, it is not well suited to study the scattering and behaviour of charge carriers in a superconducting material in contact with a topological material on the smallest scale.

One class of (microscopic) models is based on the Green's functions technique. The interested reader is referred to [79] for an elaborate treatment of the application of Green's functions in the context of superconductivity. One well-known equation in the field of Green's functions is the so-called Gorkov equation. It is a partial differential equation giving a detailed description of quantum transport in a superconductor. The level of physical detail in this equations comes at a numerical computational cost. Therefore, people are forced to study the Gorkov equation in limiting cases. For instance, af-

ter further simplification and in the diffusive (dirty) limit one arrives at the Usadel equation. The Usadel equation can be solved numerically to get the dynamics of charge carriers in a diffusive (un)conventional superconductor, in contact with a normal metal. It however can not be trivially extended to include topological effects.

Evolved from BCS theory (discussed in section 2.1.2), there is another set of equations having a microscopic origin, called the Bogoliubov-de Gennes equations. The equations find their origin in the work by de Gennes [80], and are based on BCS theory, meaning that the microscopic origin of the charge carriers responsible for superconductivity, i.e., the Cooper pairs arise from an attractive pairing interaction. In short, the BdG equations can be viewed as a coupled set of Schrödinger equations, with much emphasis on the description of superconductivity in terms of electron- and hole-like quasiparticles. This enables an insightful description of quasiparticle properties down to the atomic scale. The BdG formalism serves as a complementary approach to the Ginzburg–Landau theory that is used to describe the spatial variations of the superconducting order parameter, when it is slowly varying at a larger length scale [75].

In this work, we consider the conduction through a topological insulator base material in contact with superconducting and magnetic active materials. We are interested in the behaviour, on the smallest scale, of the (quasiparticle) charge carriers in a system consisting of multiple interfaces between materials of varying kinds. Since the edge states in a topological insulator are topologically protected, we are in a clean conduction limit (ballistic). Moreover, superconductivity is induced into the topological insulator through the proximity effect by considering a conventional *s*-wave superconductor on top of the topological insulator. Conventional superconductivity is confined to low temperatures. Hence we are dealing with a ballistic low-temperature regime. A set of equations that, in light of the context of this work, can capture the essential features of the intricate physics occurring when we combine superconductivity, magnetism and topology are the BdG equations. In the coming two subsection we derive (section 3.1) and solve (section 3.2) the BdG equations in a plane wave basis for the steady-state eigenfunctions.

### 3.1 Derivation Bogoliubov-de Gennes equations

The BdG equations are, in essence, a coupled set of Schrödinger equations describing the quasiparticle excitations from the superconducting condensate. Here, we briefly sketch the outline of the coming derivation. We have 4 un-

known functions that we represent in a vector,  $\boldsymbol{\phi} = (u_{\uparrow}(\mathbf{r}), u_{\downarrow}(\mathbf{r}), v_{\uparrow}(\mathbf{r}), v_{\downarrow}(\mathbf{r}))^T$ , the  $u_{\sigma}$  and  $v_{\sigma}$  ( $\sigma$  indicated the spin orientation) one might recognize from BCS theory. They are governed by the coupled BdG equations. We are after a Hamiltonian (in matrix form) such that we get a Schrödinger like equation:  $\tilde{H}_{BdG}\boldsymbol{\phi} = E\boldsymbol{\phi}$ . We consider a suitable Hamiltonian expressed in the electronic creation and annihilation field operators  $\psi^{\dagger}$  and  $\psi$ . We apply a mean field approximation to reduce its complexity to arrive at a reduced effective Hamiltonian  $\mathcal{H}_{eff}$  in bi-linear form. Next, we use a so-called Bogoliubov transformation to go from electronic field operators to quasiparticle field operators  $\gamma, \gamma^{\dagger}$ , this transformation diagonalizes the bi-linear form  $\mathcal{H}_{eff}$ . In this transformation, we write the electronic field operators ( $\psi, \psi^{\dagger}$ ) as a linear combination of the Fermionic quasiparticle operators ( $\gamma, \gamma^{\dagger}$ ), the coefficients in this expansion are  $u_{\sigma}$  and  $v_{\sigma}$  coefficients. To derive the BdG, we compute the commutators of the form  $[\psi_{\sigma}, \mathcal{H}_{eff}]$ , and  $[\gamma, \mathcal{H}_{eff}]$ . By plugging in the Bogoliubov transformation for the  $\psi$ s in the commutation relation and equating this result to the computed commutator  $[\gamma, \mathcal{H}_{eff}]$  we get a coupled set of equation describing the  $u_{\sigma}$  and  $v_{\sigma}$ . Final, we write this set of equations in a matrix form using the vector  $\boldsymbol{\phi}$  containing the unknown coefficients. The following derivation is an extension of the work by Jian-Xin Zhu [75] by introducing topology. An alternative derivations can be done using a tight binding model [81]. For further references on the BdG equations, see [43], [30].

### 3.1.1 Hamiltonian

A Hamiltonian describing an attractive pairing potential in second quantization language is of the form

$$\mathcal{H} = \int d\mathbf{r} \psi_{\alpha}^{\dagger}(\mathbf{r}) h_{\alpha\beta}(\mathbf{r}) \psi_{\beta}(\mathbf{r}) - \frac{1}{2} \int \int d\mathbf{r} d\mathbf{r}' V_{eff}(\mathbf{r}, \mathbf{r}') \psi_{\alpha}^{\dagger}(\mathbf{r}) \psi_{\beta}^{\dagger}(\mathbf{r}') \psi_{\beta}(\mathbf{r}') \psi_{\alpha}(\mathbf{r}), \quad (3.1)$$

where the Greek subscripts indicate spin orientation (up, down), and we use the Einstein summation convention. The first term describes a single particle (topological) Hamiltonian. We have chosen a positive  $V_{eff}$ , such that the second term constitutes an attractive potential [75]. The second term describes the pairing that is observed in superconductivity. The relevant field operators are the electron creation and annihilation operators,  $\psi_{\alpha}^{\dagger}(\mathbf{r})$  and  $\psi_{\alpha}(\mathbf{r})$  respectively. The field operators obey the following anti-commutation

relations

$$\begin{aligned} \left\{ \psi_\alpha(\mathbf{r}), \psi_\beta^\dagger(\mathbf{r}') \right\} &= \delta(\mathbf{r} - \mathbf{r}') \delta_{\alpha\beta}, \\ \left\{ \psi_\alpha(\mathbf{r}), \psi_\beta(\mathbf{r}') \right\} &= \left\{ \psi_\alpha^\dagger(\mathbf{r}), \psi_\beta^\dagger(\mathbf{r}') \right\} = 0, \end{aligned} \quad (3.2)$$

where  $\{A, B\} := AB + BA$  is defined as the anti-commutator of two operators  $A, B$ , later we will encounter the commutator  $[A, B] := AB - BA$ . We describe the topological effects, c.q. the topological Hamiltonians in (2.11) by a Dirac-like single particle Hamiltonian with spin orbit coupling (Rashba effect) [38],

$$h_{\alpha\beta} = v_f \mathbf{p} \cdot \boldsymbol{\sigma} - \mu \sigma_0 + \mathbf{m} \cdot \boldsymbol{\sigma}, \quad (3.3)$$

where  $\boldsymbol{\sigma} = (\sigma_x, \sigma_y, \sigma_z)$  are the canonical Hermitian unitary Pauli spin matrices and  $\sigma_0$  is the two dimensional identity matrix. The first term introduces spin orbit coupling, where  $v_f$  is the Fermi velocity and  $\mathbf{p}$  is the momentum. The second term sets the chemical potential,  $\mu$ . The final term is added to study the consequences of an induced ferromagnetic effect, note that  $\mathbf{m} = (m_x, m_y, m_z)$  is the magnetization vector with each  $m_i$ , for  $i = x, y, z$  having units of energy. Please note that here no spatial dependencies are specified, for instance the chemical potential or the magnetic energy gap are homogenous in each material, but their value depends on which material we are considering. For example, in the MTI region  $m_z$  is finite, but in the TI or STI  $m_z = 0$ .

### 3.1.2 Mean field approximation

The pairing term in the Hamiltonian (3.1) has a four-field operator term. To reduce the complexity, we can perform a mean-field approximation. Physically speaking, a mean-field approximation is valid when the random (thermal) fluctuations are small relative to a constant background. For  $s$ -wave superconductivity, we, by definition, require low temperatures such that we are well below the critical superconducting temperature, where thermal fluctuations are sufficiently small compare to the background [75] [82]. Mean-field theories are generally used to reduce a many-body problem to a two-body or single body problem. The loss of higher-order effects come at the benefit of reduced algebraic complexity and numerical costs when doing simulations. We consider a background energy level (mean-field) and focus on fluctuations from this mean background field, i.e., we write a product of two field operators as the sum of a mean plus fluctuations

$$\begin{aligned} \psi_\alpha^\dagger(\mathbf{r}) \psi_\beta^\dagger(\mathbf{r}') &= \langle \psi_\alpha^\dagger(\mathbf{r}), \psi_\beta^\dagger(\mathbf{r}') \rangle + (\psi_\alpha^\dagger(\mathbf{r}) \psi_\beta^\dagger(\mathbf{r}') - \langle \psi_\alpha^\dagger(\mathbf{r}), \psi_\beta^\dagger(\mathbf{r}') \rangle), \\ \psi_\beta(\mathbf{r}') \psi_\alpha(\mathbf{r}) &= \langle \psi_\beta(\mathbf{r}'), \psi_\alpha(\mathbf{r}) \rangle + (\psi_\beta(\mathbf{r}') \psi_\alpha(\mathbf{r}) - \langle \psi_\beta(\mathbf{r}'), \psi_\alpha(\mathbf{r}) \rangle). \end{aligned} \quad (3.4)$$

We have not changed anything, we simply added and subtracted a mean  $\langle \psi_\alpha^\dagger(\mathbf{r}), \psi_\beta^\dagger(\mathbf{r}') \rangle$ , to get fluctuations  $(\psi_\alpha^\dagger(\mathbf{r})\psi_\beta^\dagger(\mathbf{r}') - \langle \psi_\alpha^\dagger(\mathbf{r}), \psi_\beta^\dagger(\mathbf{r}') \rangle)$ . First we note that we model *s*-wave superconductors, so we shall only consider spin singlet pairing. We now substitute (3.4) in the two particle term in (3.1) and ignore terms consisting of the product of fluctuations because for low temperatures these are small compared to the mean field. This gives

$$\begin{aligned}
& -\frac{1}{2} \int \int d\mathbf{r}d\mathbf{r}' V_{\text{eff}}(\mathbf{r}, \mathbf{r}') \psi_\alpha^\dagger(\mathbf{r})\psi_\beta^\dagger(\mathbf{r}') \psi_\beta(\mathbf{r}') \psi_\alpha(\mathbf{r}) \\
&= -\frac{1}{2} \int \int d\mathbf{r}d\mathbf{r}' V_{\text{eff}}(\mathbf{r}, \mathbf{r}') \left[ \langle \psi_\alpha^\dagger(\mathbf{r}), \psi_\beta^\dagger(\mathbf{r}') \rangle + (\psi_\alpha^\dagger(\mathbf{r})\psi_\beta^\dagger(\mathbf{r}') - \langle \psi_\alpha^\dagger(\mathbf{r}), \psi_\beta^\dagger(\mathbf{r}') \rangle) \right] \\
&\quad \times \left[ \langle \psi_\beta(\mathbf{r}'), \psi_\alpha(\mathbf{r}) \rangle + (\psi_\beta(\mathbf{r}')\psi_\alpha(\mathbf{r}) - \langle \psi_\beta(\mathbf{r}'), \psi_\alpha(\mathbf{r}) \rangle) \right] \\
&\approx - \int \int d\mathbf{r}d\mathbf{r}' V_{\text{eff}}(\mathbf{r}, \mathbf{r}') \left[ - \langle \psi_\uparrow^\dagger(\mathbf{r})\psi_\downarrow^\dagger(\mathbf{r}') \rangle \langle \psi_\downarrow(\mathbf{r}')\psi_\uparrow(\mathbf{r}) \rangle \right. \\
&\quad \left. + \langle \psi_\uparrow^\dagger(\mathbf{r})\psi_\downarrow^\dagger(\mathbf{r}') \rangle \psi_\downarrow(\mathbf{r}')\psi_\uparrow(\mathbf{r}) \right. \\
&\quad \left. + \psi_\uparrow^\dagger(\mathbf{r})\psi_\downarrow^\dagger(\mathbf{r}') \langle \psi_\downarrow(\mathbf{r}')\psi_\uparrow(\mathbf{r}) \rangle \right] \\
&= \iint d\mathbf{r}d\mathbf{r}' \frac{|\Delta(\mathbf{r}, \mathbf{r}')|^2}{V_{\text{eff}}(\mathbf{r}, \mathbf{r}')} + \iint d\mathbf{r}d\mathbf{r}' \left[ \Delta^*(\mathbf{r}, \mathbf{r}') \psi_\downarrow(\mathbf{r}')\psi_\uparrow(\mathbf{r}) + \Delta(\mathbf{r}, \mathbf{r}') \psi_\uparrow^\dagger(\mathbf{r})\psi_\downarrow^\dagger(\mathbf{r}') \right],
\end{aligned}$$

where the spherical symmetric *s*-wave pairing potential is given by

$$\begin{aligned}
\Delta(\mathbf{r}, \mathbf{r}') &= -V_{\text{eff}}(\mathbf{r} - \mathbf{r}') \langle \psi_\downarrow(\mathbf{r}') \psi_\uparrow(\mathbf{r}) \rangle = V_{\text{eff}}(\mathbf{r} - \mathbf{r}') \langle \psi_\uparrow(\mathbf{r}) \psi_\downarrow(\mathbf{r}') \rangle, \\
\Delta^*(\mathbf{r}, \mathbf{r}') &= -V_{\text{eff}}(\mathbf{r} - \mathbf{r}') \langle \psi_\uparrow^\dagger(\mathbf{r}) \psi_\downarrow^\dagger(\mathbf{r}') \rangle = V_{\text{eff}}(\mathbf{r} - \mathbf{r}') \langle \psi_\downarrow^\dagger(\mathbf{r}') \psi_\uparrow^\dagger(\mathbf{r}) \rangle.
\end{aligned} \tag{3.5}$$

After plugging the reduced mean field form of pairing term back into (3.1) we find the following effective Hamiltonian

$$\begin{aligned}
\mathcal{H}_{eff} &= \int d\mathbf{r} \psi_\alpha^\dagger(\mathbf{r}) h_{\alpha\beta}(\mathbf{r}) \psi_\beta(\mathbf{r}) + \iint d\mathbf{r}d\mathbf{r}' \left[ \Delta^*(\mathbf{r}, \mathbf{r}') \psi_\downarrow(\mathbf{r}')\psi_\uparrow(\mathbf{r}) + \Delta(\mathbf{r}, \mathbf{r}') \psi_\uparrow^\dagger(\mathbf{r})\psi_\downarrow^\dagger(\mathbf{r}') \right] \\
&\quad + \iint d\mathbf{r}d\mathbf{r}' \frac{|\Delta(\mathbf{r}, \mathbf{r}')|^2}{V_{\text{eff}}(\mathbf{r}, \mathbf{r}')}.
\end{aligned} \tag{3.6}$$

Note that we have reduced the complexity from a term with a product of four field operators to only a product of two. Through this, the effective Hamiltonian becomes the sum of bilinear terms [75]. This result tells us that there is an associated matrix to represent this bilinear form [83]. This matrix might be diagonalizable through an additional transformation. In the following subsections we will follow this path by first calculating the commutators between  $\mathcal{H}_{eff}$  and the field operators of the form,  $[\psi_\uparrow(\mathbf{r}), \mathcal{H}_{eff}]$ , to observe the structure of this matrix. This matrix becomes important when

we want to find the (quasi)particle wavefunction solutions to the Hamiltonian as eigensolutions of this matrix.

### 3.1.3 Commutators

We calculate the commutation relations between the effective Hamiltonian and the field operators using two results. Let  $A, B$  and  $C$  be three operators, then

$$\begin{aligned} [A, BC] &:= ABC - BCA \\ &= ABC + BAC - BAC - BCA \\ &= (ABC + BAC) - (BAC + BCA) \\ &= \{A, B\}C - B\{A, C\}. \end{aligned}$$

So we find

$$[A, BC] = \{A, B\}C - B\{A, C\}. \quad (3.7)$$

This identity will prove useful when we want to change the order of two operators  $A$  and  $BC$ . Say we know  $\{A, B\}$  and  $\{A, C\}$  then to swap  $A$  and  $BC$  we can simply use (3.7).

Let  $[a, b]$  be some domain and  $\delta(x)$  be the Dirac delta function obeying the defining property

$$\int_a^b \delta(x - x_0) dx = \begin{cases} 1 & \text{if } x_0 \in (a, b), \\ 0 & \text{if } x_0 \notin [a, b], \end{cases}$$

such that for any test function  $f(x)$  continuous at  $x_0$  we have

$$\int_a^b \delta(x - x_0) f(x) dx = \begin{cases} f(x_0) & \text{if } x_0 \in (a, b), \\ 0 & \text{if } x_0 \notin [a, b]. \end{cases}$$

Using this, simple integration by parts gives us (vanishing boundary terms  $\delta(a - x)$  and  $\delta(b - x)$ )

$$\int_a^b \frac{d\delta(x - x_0)}{dx} f(x) dx = \begin{cases} -\frac{df(x)}{dx} \Big|_{x_0} & \text{if } x_0 \in (a, b), \\ 0 & \text{if } x_0 \notin [a, b]. \end{cases} \quad (3.8)$$

This later result will become useful when we want to compute the commutator between a term consisting of a differential operator e.g.  $h_{\alpha\beta}$  and a function  $\psi(\mathbf{r})$ .

Observe that the effective Hamiltonian consists of a topology term ( $h_{\alpha\beta}$ ), a pairing term ( $V_{eff}$ ), and a constant term ( $\frac{|\Delta(r,r')|^2}{V_{eff}}$ ). We write  $\mathcal{H}_{eff} = T + P + C$  and immediately note that any operator commutes with a constant term. Hence, we only need to compute the commutation relation between the field operators and the  $T$  and  $P$  terms. Using (3.2) and (3.7) we calculate

$$\begin{aligned}
[\psi_\alpha(\hat{\mathbf{r}}), P] &= \iint d\mathbf{r}d\mathbf{r}' [\Delta^*(\mathbf{r}, \mathbf{r}') (\{\psi_\alpha(\hat{\mathbf{r}}), \psi_\downarrow(\mathbf{r}')\} \psi_\uparrow(\mathbf{r}) - \psi_\downarrow(\mathbf{r}') \{\psi_\alpha(\hat{\mathbf{r}}), \psi_\uparrow(\mathbf{r})\}) \\
&\quad + \Delta(\mathbf{r}, \mathbf{r}') (\{\psi_\alpha(\hat{\mathbf{r}}), \psi_\uparrow^\dagger(\mathbf{r})\} \psi_\downarrow^\dagger(\mathbf{r}') - \psi_\uparrow^\dagger(\mathbf{r}) \{\psi_\alpha(\hat{\mathbf{r}}), \psi_\downarrow^\dagger(\mathbf{r}')\})] \\
&= \iint d\mathbf{r}d\mathbf{r}' \Delta(\mathbf{r}, \mathbf{r}') (\delta_{\alpha\uparrow} \delta(\hat{\mathbf{r}} - \mathbf{r}) \psi_\downarrow^\dagger(\mathbf{r}') - \psi_\uparrow^\dagger(\mathbf{r}) \delta_{\alpha\downarrow} \delta(\hat{\mathbf{r}} - \mathbf{r}')) \\
&= \delta_{\alpha\uparrow} \int d\mathbf{r}' \Delta(\hat{\mathbf{r}}, \mathbf{r}') \psi_\downarrow^\dagger(\mathbf{r}') - \delta_{\alpha\downarrow} \int d\mathbf{r} \Delta(\mathbf{r}, \hat{\mathbf{r}}) \psi_\uparrow^\dagger(\mathbf{r}).
\end{aligned}$$

Similarly we find

$$[\psi_\alpha^\dagger(\hat{\mathbf{r}}), P] = \delta_{\alpha\downarrow} \int d\mathbf{r} \Delta^*(\mathbf{r}, \hat{\mathbf{r}}) \psi_\uparrow(\mathbf{r}) - \delta_{\alpha\uparrow} \int d\mathbf{r}' \Delta^*(\hat{\mathbf{r}}, \mathbf{r}') \psi_\downarrow(\mathbf{r}').$$

Now using (3.2), and (3.7) we calculate  $[\psi_\alpha(\hat{\mathbf{r}}), T]$ :

$$\begin{aligned}
[\psi_\gamma(\hat{\mathbf{r}}), T] &= \int d\mathbf{r} [\{\psi_\gamma(\hat{\mathbf{r}}), \psi_\alpha^\dagger(\mathbf{r})\} h_{\alpha\beta}(\mathbf{r}) \psi_\beta(\mathbf{r}) - \psi_\alpha^\dagger(\mathbf{r}) \{\psi_\gamma(\hat{\mathbf{r}}), h_{\alpha\beta}(\mathbf{r}) \psi_\beta(\mathbf{r})\}] \\
&= \int d\mathbf{r} \delta_{\alpha\gamma} \delta(\mathbf{r} - \hat{\mathbf{r}}) h_{\alpha\beta}(\mathbf{r}) \psi_\beta(\mathbf{r}) \\
&= h_{\gamma\beta}(\hat{\mathbf{r}}) \psi_\beta(\hat{\mathbf{r}}) \\
&= h_{\gamma\uparrow}(\hat{\mathbf{r}}) \psi_\uparrow(\hat{\mathbf{r}}) + h_{\gamma\downarrow}(\hat{\mathbf{r}}) \psi_\downarrow(\hat{\mathbf{r}}).
\end{aligned}$$

Now also using (3.8) we find

$$\begin{aligned}
[\psi_\gamma^\dagger(\hat{\mathbf{r}}), T] &= \int d\mathbf{r} [\{\psi_\gamma^\dagger(\hat{\mathbf{r}}), \psi_\alpha^\dagger(\mathbf{r})\} h_{\alpha\beta}(\mathbf{r}) \psi_\beta(\mathbf{r}) - \psi_\alpha^\dagger(\mathbf{r}) h_{\alpha\beta}(\mathbf{r}) \{\psi_\gamma^\dagger(\hat{\mathbf{r}}), \psi_\beta(\mathbf{r})\}] \\
&= - \int d\mathbf{r} \psi_\alpha^\dagger(\mathbf{r}) h_{\alpha\beta}(\mathbf{r}) \delta(\mathbf{r} - \hat{\mathbf{r}}) \delta_{\gamma\beta} \\
&= - \int d\mathbf{r} \psi_\alpha^\dagger(\mathbf{r}) h_{\alpha\gamma}(\mathbf{r}) \delta(\mathbf{r} - \hat{\mathbf{r}}) \\
&= -h_{\gamma\alpha}^*(\hat{\mathbf{r}}) \psi_\alpha^\dagger(\hat{\mathbf{r}}) \\
&= -h_{\gamma\uparrow}^*(\hat{\mathbf{r}}) \psi_\uparrow^\dagger(\hat{\mathbf{r}}) - h_{\gamma\downarrow}^*(\hat{\mathbf{r}}) \psi_\downarrow^\dagger(\hat{\mathbf{r}}).
\end{aligned}$$

It is important to stress here that in the fourth step we used (3.8), effectively giving a minus sign to the differential part of the single particle Hamiltonian in (3.3). That is, only those terms in the single particle Hamiltonian that consist of a differential operator should change sign. Now we validate the fourth line in the above derivation. The way we can incorporate this sign change in the equations, depends on the form of  $h_{\alpha\beta}$  in (3.3). Say we consider a magnetic field in the  $z$  direction and a spin-orbit coupling term, then  $h_{\alpha\beta}$  reduces to<sup>9</sup>

$$h_{\alpha\beta} = -i\hbar v_f \left( \frac{d}{dx} \sigma_x + \frac{d}{dy} \sigma_y \right) - \mu \sigma_0 + m_z \sigma_z, \quad (3.9)$$

in this case we can show that using the conjugate plus transpose for  $h_{\alpha\beta}$  as above correctly handles this sign change. We introduce the notation  $(\frac{\partial}{\partial \mathbf{x}})$  to indicate the sign in front of the differential operators in the single particle Hamiltonian. After the third line we essentially have a term of the form  $h_{\beta\alpha}(-\frac{\partial}{\partial \mathbf{x}})$ . We show that, using the fact that each Pauli matrix is Hermitian ( $\sigma_i^\dagger = \sigma_i \leftrightarrow \sigma_i^* = \sigma_i^T$ ), this is equal to

$$\begin{aligned} h_{\beta\alpha}(-\frac{\partial}{\partial \mathbf{x}}) &= \left( -i\hbar v_f \left( (-\frac{d}{dx}) \sigma_x + (-\frac{d}{dy}) \sigma_y \right) - \mu \sigma_0 + m_z \sigma_z \right)^T \\ &= -i\hbar v_f \left( -\frac{d}{dx} \sigma_x^* - \frac{d}{dy} \sigma_y^* \right) - \mu \sigma_0^* + m_z \sigma_z^* \\ &= \left( -i\hbar v_f \left( \frac{d}{dx} \sigma_x + \frac{d}{dy} \sigma_y \right) - \mu \sigma_0 + m_z \sigma_z \right)^* \\ &= h_{\alpha\beta}^* \left( \frac{\partial}{\partial \mathbf{x}} \right). \end{aligned}$$

We have used the fact that both  $\mu$  and  $m_z$  are real.

Combining the results for all commutators gives (relabeling  $\hat{\mathbf{r}} \rightarrow \mathbf{r}$ )

$$\begin{aligned} [\psi_\uparrow(\mathbf{r}), \mathcal{H}_{eff}] &= h_{\uparrow\uparrow}(\mathbf{r}) \psi_\uparrow(\mathbf{r}) + h_{\uparrow\downarrow}(\mathbf{r}) \psi_\downarrow(\mathbf{r}) + \int d\mathbf{r}' \Delta(\mathbf{r}, \mathbf{r}') \psi_\downarrow^\dagger(\mathbf{r}'), \\ [\psi_\downarrow(\mathbf{r}), \mathcal{H}_{eff}] &= h_{\downarrow\uparrow}(\mathbf{r}) \psi_\uparrow(\mathbf{r}) + h_{\downarrow\downarrow}(\mathbf{r}) \psi_\downarrow(\mathbf{r}) - \int d\mathbf{r}' \Delta(\mathbf{r}', \mathbf{r}) \psi_\uparrow^\dagger(\mathbf{r}'), \\ [\psi_\uparrow^\dagger(\mathbf{r}), \mathcal{H}_{eff}] &= -h_{\uparrow\uparrow}^*(\mathbf{r}) \psi_\uparrow^\dagger(\mathbf{r}) - h_{\uparrow\downarrow}^*(\mathbf{r}) \psi_\downarrow^\dagger(\mathbf{r}) - \int d\mathbf{r}' \Delta^*(\mathbf{r}, \mathbf{r}') \psi_\downarrow(\mathbf{r}'), \\ [\psi_\downarrow^\dagger(\mathbf{r}), \mathcal{H}_{eff}] &= -h_{\downarrow\uparrow}^*(\mathbf{r}) \psi_\uparrow^\dagger(\mathbf{r}) - h_{\downarrow\downarrow}^*(\mathbf{r}) \psi_\downarrow^\dagger(\mathbf{r}) + \int d\mathbf{r}' \Delta^*(\mathbf{r}', \mathbf{r}) \psi_\uparrow(\mathbf{r}'). \end{aligned} \quad (3.10)$$

---

<sup>9</sup>The constant term  $\iint d\mathbf{r} d\mathbf{r}' \frac{|\Delta(\mathbf{r}, \mathbf{r}')|^2}{V_{\text{eff}}(\mathbf{r}, \mathbf{r}' )}$  is taken into the chemical potential.

### 3.1.4 Bogoliubov transformation

The set of commutators in (3.10) allows us to consider a transformation that uncovers more structure in the matrix associated with the bilinear form in (3.6). Following Nikolai Bogoliubov's 1958 work [84] we introduce the electron field operator in terms of electron- and hole-like quasiparticles,

$$\psi_\alpha(\mathbf{r}) = \sum_n [u_{n\alpha}(\mathbf{r})\gamma_n - \alpha v_{n\alpha}^*(\mathbf{r})\gamma_n^\dagger], \quad (3.11)$$

where the spin  $\alpha = \pm 1$  for spin up or down.  $\gamma_n^\dagger, \gamma_n$  create and annihilate Fermionic quasiparticles with well defined spin in a superposition of electron and hole states. Recall that we are trying to find an associated matrix  $\check{M}$  for the effective Hamiltonian in bi-linear form, such that given the ground state energy  $E_g$  we have

$$\mathcal{H}_{eff} = E_g + \boldsymbol{\psi}^\dagger \check{M} \boldsymbol{\psi}.$$

For  $\boldsymbol{\psi} = (\psi_\uparrow, \psi_\downarrow, \psi_\uparrow^\dagger, \psi_\downarrow^\dagger)^T$ . Using the Bogoliubov transformation we can find a diagonalizable matrix[75]

$$\mathcal{H}_{eff} = E_g + \sum_n E_n \gamma_n^\dagger \gamma_n. \quad (3.12)$$

In fact, any system with Fermion excitations (such as  $\gamma, \gamma^\dagger$ ), the total system energy,  $\mathcal{H}_{eff}$ , can be written like this [3]. The summation runs over  $n$ , positive energy excited states, so when we consider individual energy excitations the sum becomes a single term.

A sufficient condition for the Bogoliubov transformation in (3.11) to obey the electron field operator anticommutation relation in (3.2) is for the quasiparticle operators to satisfy anticommutation relations

$$\begin{aligned} \{\gamma_n, \gamma_m^\dagger\} &= \delta_{nm}, \\ \{\gamma_n, \gamma_m\} &= \{\gamma_n^\dagger, \gamma_m^\dagger\} = 0. \end{aligned} \quad (3.13)$$

In order to strictly satisfy the electron operator anticommutators there is an additional normalization requirement on the  $u_{n\alpha}(\mathbf{r})$  and  $v_{n\alpha}(\mathbf{r})$  coefficients

$$\int d\mathbf{r} (|u_{n\alpha}(\mathbf{r})|^2 + |v_{n\alpha}(\mathbf{r})|^2) = 1. \quad (3.14)$$

### 3.1.5 Bogoliubov-de Gennes equations

Using the Bogoliubov transform in (3.11) we work in a quasiparticle basis and we can work towards the Bogoliubov-de Gennes equations. The procedure is as follows, we compute the commutators between the quasiparticle

operators  $\gamma_n^\dagger, \gamma_n$  and the effective Hamiltonian in (3.6). Then we insert the Bogoliubov transformation (3.11) into the electronic commutators in (3.10) and compare the resulting equation to the commutator results found for  $\gamma_n^\dagger$  and  $\gamma_n$ .

Now we calculate the commutator between the effective Hamiltonian and the quasiparticle creation operator:

$$\begin{aligned}
[\gamma_n^\dagger, \mathcal{H}_{eff}] &= \left[ \gamma_n^\dagger, \sum_m E_m \gamma_m^\dagger \gamma_m \right] \\
&= \sum_m E_m \gamma_n^\dagger \gamma_m^\dagger \gamma_m - \sum_m E_m \gamma_m^\dagger \gamma_m \gamma_n^\dagger \\
&= \sum_m E_m \gamma_n^\dagger \gamma_m^\dagger \gamma_m + \sum_m (E_m \gamma_m^\dagger \gamma_n^\dagger \gamma_m - \gamma_m^\dagger \{\gamma_m, \gamma_n^\dagger\}) \\
&= \sum_m E_m \gamma_n^\dagger \gamma_m^\dagger \gamma_m - \sum_m E_m (\gamma_n^\dagger \gamma_m^\dagger \gamma_m - \gamma_m \{\gamma_n^\dagger, \gamma_m^\dagger\} + \gamma_m^\dagger \delta_{mn}) \\
&= - \sum_m E_m \gamma_m^\dagger \delta_{mn} \\
&= -E_n \gamma_n^\dagger,
\end{aligned}$$

and for the annihilation operator we find something similar

$$\begin{aligned}
[\gamma_n^\dagger, \mathcal{H}_{eff}] &= -E_n \gamma_n^\dagger, \\
[\gamma_n, \mathcal{H}_{eff}] &= E_n \gamma_n.
\end{aligned} \tag{3.15}$$

We substitute the Bogoliubov transformed electron operators in (3.11) into the previously derived commutators in (3.10) and use the quasiparticle results in (3.13) and (3.15) to derive the Bogoliubov-de Gennes equations. For the given Hamiltonian these consist of four equations. First we consider the  $\psi_\uparrow(\mathbf{r})$

case. This gives

$$\begin{aligned}
[\psi_{\uparrow}(\mathbf{r}), \mathcal{H}_{eff}] &= \left[ \sum_n [u_{n\uparrow}(\mathbf{r})\gamma_n - v_{n\uparrow}^*(\mathbf{r})\gamma_n^\dagger], \mathcal{H}_{eff} \right] \\
&= \sum_n u_{n\uparrow}(\mathbf{r})[\gamma_n, \mathcal{H}_{eff}] - \sum_n v_{n\uparrow}^*(\mathbf{r})[\gamma_n^\dagger, \mathcal{H}_{eff}] \\
&\stackrel{*}{=} \sum_n E_n [u_{n\uparrow}(\mathbf{r})\gamma_n + v_{n\uparrow}^*(\mathbf{r})\gamma_n^\dagger] \\
[\psi_{\uparrow}(\mathbf{r}), \mathcal{H}_{eff}] &= h_{\uparrow\uparrow}(\mathbf{r})\psi_{\uparrow}(\mathbf{r}) + h_{\uparrow\downarrow}(\mathbf{r})\psi_{\downarrow}(\mathbf{r}) + \int d\mathbf{r}' \Delta(\mathbf{r}, \mathbf{r}') \psi_{\downarrow}^\dagger(\mathbf{r}') \\
&\stackrel{*}{=} h_{\uparrow\uparrow}(\mathbf{r}) \sum_n [u_{n\uparrow}(\mathbf{r})\gamma_n - v_{n\uparrow}^*(\mathbf{r})\gamma_n^\dagger] \\
&\quad + h_{\uparrow\downarrow}(\mathbf{r}) \sum_n [u_{n\downarrow}(\mathbf{r})\gamma_n + v_{n\downarrow}^*(\mathbf{r})\gamma_n^\dagger] \\
&\quad + \int d\mathbf{r}' \Delta(\mathbf{r}, \mathbf{r}') \sum_n [u_{n\downarrow}^*(\mathbf{r}')\gamma_n^\dagger + v_{n\downarrow}(\mathbf{r}')\gamma_n].
\end{aligned}$$

By equating the coefficients of each  $\gamma_n$  term for the marked (\*) lines we find

$$E_n u_{n\uparrow}(\mathbf{r}) = h_{\uparrow\uparrow}(\mathbf{r})u_{n\uparrow}(\mathbf{r}) + h_{\uparrow\downarrow}(\mathbf{r})u_{n\downarrow}(\mathbf{r}) + \int d\mathbf{r}' \Delta(\mathbf{r}, \mathbf{r}') v_{n\downarrow}(\mathbf{r}'). \quad (3.16)$$

We could have equally well collected  $\gamma_n^\dagger$ -terms, but this would result in the equivalent equation (overall conjugation and minus sign). A similar computation for  $\psi_{\uparrow}^\dagger(\mathbf{r})$  results in

$$\begin{aligned}
[\psi_{\uparrow}^\dagger(\mathbf{r}), \mathcal{H}_{eff}] &= \left[ \sum_n [u_{n\uparrow}^*(\mathbf{r})\gamma_n^\dagger - v_{n\uparrow}(\mathbf{r})\gamma_n], \mathcal{H}_{eff} \right] \\
&= \sum_n u_{n\uparrow}^*(\mathbf{r})[\gamma_n^\dagger, \mathcal{H}_{eff}] - \sum_n v_{n\uparrow}(\mathbf{r})[\gamma_n, \mathcal{H}_{eff}] \\
&\stackrel{*}{=} - \sum_n E_n [u_{n\uparrow}^*(\mathbf{r})\gamma_n^\dagger + v_{n\uparrow}(\mathbf{r})\gamma_n] \\
[\psi_{\uparrow}^\dagger(\mathbf{r}), \mathcal{H}_{eff}] &= -h_{\uparrow\uparrow}^*(\mathbf{r})\psi_{\uparrow}^\dagger(\mathbf{r}) - h_{\uparrow\downarrow}^*(\mathbf{r})\psi_{\downarrow}^\dagger(\mathbf{r}) - \int d\mathbf{r}' \Delta^*(\mathbf{r}, \mathbf{r}') \psi_{\downarrow}(\mathbf{r}') \\
&\stackrel{*}{=} -h_{\uparrow\uparrow}^*(\mathbf{r}) \sum_n [u_{n\uparrow}^*(\mathbf{r})\gamma_n^\dagger - v_{n\uparrow}(\mathbf{r})\gamma_n] \\
&\quad - h_{\uparrow\downarrow}^*(\mathbf{r}) \sum_n [u_{n\downarrow}^*(\mathbf{r})\gamma_n^\dagger + v_{n\downarrow}(\mathbf{r})\gamma_n] \\
&\quad - \int d\mathbf{r}' \Delta^*(\mathbf{r}, \mathbf{r}') \sum_n [u_{n\downarrow}(\mathbf{r}')\gamma_n + v_{n\downarrow}^*(\mathbf{r}')\gamma_n^\dagger].
\end{aligned}$$

By comparing terms of equal  $\gamma_n$  we arrive at

$$E_n v_{n\uparrow}(\mathbf{r}) = -h_{\uparrow\uparrow}^*(\mathbf{r})v_{n\uparrow}(\mathbf{r}) + h_{\uparrow\downarrow}^*(\mathbf{r})v_{n\downarrow}(\mathbf{r}) + \int d\mathbf{r}' \Delta^*(\mathbf{r}, \mathbf{r}') u_{n\downarrow}(\mathbf{r}'). \quad (3.17)$$

We go through the same procedure for the remaining two spin orientations, i.e.,  $\psi_{\downarrow}(\mathbf{r})$  and  $\psi_{\downarrow}^\dagger(\mathbf{r})$ . Then we collect all four equations together and in the end we find the coupled set of so-called Bogoliubov-de Gennes<sup>10</sup> equations:

$$\begin{aligned} E_n u_{n\uparrow}(\mathbf{r}) &= h_{\uparrow\uparrow}(\mathbf{r})u_{n\uparrow}(\mathbf{r}) + h_{\uparrow\downarrow}(\mathbf{r})u_{n\downarrow}(\mathbf{r}) + \int d\mathbf{r}' \Delta(\mathbf{r}, \mathbf{r}') v_{n\downarrow}(\mathbf{r}'), \\ E_n u_{n\downarrow}(\mathbf{r}) &= h_{\downarrow\uparrow}(\mathbf{r})u_{n\uparrow}(\mathbf{r}) + h_{\downarrow\downarrow}(\mathbf{r})u_{n\downarrow}(\mathbf{r}) + \int d\mathbf{r}' \Delta(\mathbf{r}, \mathbf{r}') v_{n\uparrow}(\mathbf{r}'), \\ E_n v_{n\uparrow}(\mathbf{r}) &= -h_{\uparrow\uparrow}^*(\mathbf{r})v_{n\uparrow}(\mathbf{r}) + h_{\uparrow\downarrow}^*(\mathbf{r})v_{n\downarrow}(\mathbf{r}) + \int d\mathbf{r}' \Delta^*(\mathbf{r}, \mathbf{r}') u_{n\downarrow}(\mathbf{r}'), \\ E_n v_{n\downarrow}(\mathbf{r}) &= h_{\downarrow\uparrow}^*(\mathbf{r})v_{n\uparrow}(\mathbf{r}) - h_{\downarrow\downarrow}^*(\mathbf{r})v_{n\downarrow}(\mathbf{r}) + \int d\mathbf{r}' \Delta^*(\mathbf{r}, \mathbf{r}') u_{n\uparrow}(\mathbf{r}'). \end{aligned} \quad (3.18)$$

These Bogoliubov-de Gennes equations describe the steady-state behaviour of a superconducting, magnetic active, topological material. Since no time derivatives are present the equations describe a steady-state. Moreover, topology and (induced) magnetism are in the form of  $h_{\alpha\beta}$  in (3.9) and superconductivity enters through  $\Delta(\mathbf{r}, \mathbf{r}')$ . The form of  $h_{\alpha\beta}$  and the presence or absence of a superconducting energy gap depends on the material we wish to model using the BdG equations. The space-dependent functions we are after are the quasiparticle 'weights'  $u_{n\sigma}(\mathbf{r})$  and  $v_{n\sigma}(\mathbf{r})$  for both spin orientations. Similar to in BCS theory the quasiparticle excitations are fully described by these weights [3]. We note that we will drop the label  $n$ , since we consider only single energy excitations separately. In principle, one can now use an algorithm of choice to solve the coupled linear differential equations (3.18). We will write them into a matrix using a basis (representation) and solve for the plane-wave eigensolutions.

### 3.1.6 Bogoliubov-de Gennes equations in matrix form

The set of equations (3.18) can be written into a matrix equation to emphasize the underlying structure. We let the four quasiparticle weights form a

<sup>10</sup>This set of equations is named after the Russian mathematical physicist Nikolay Bogolyubov (transliterated from Russian to Bogoliubov) for his contribution through the Bogoliubov transformation [84], and the French physicist Pierre-Gilles de Gennes for the original physical formalism described by this Hamiltonian [75].

basis (or representation) vector

$$\phi_{\mathbf{1}}(\mathbf{r}) = \begin{pmatrix} u_{\uparrow}(\mathbf{r}) \\ u_{\downarrow}(\mathbf{r}) \\ v_{\uparrow}(\mathbf{r}) \\ v_{\downarrow}(\mathbf{r}) \end{pmatrix}, \quad (3.19)$$

such that we can write the Bogoliubov-de Gennes equations (3.18) in a matrix-vector form (for a single excitation, so we drop the  $n$ -label)

$$\int d\mathbf{r}' \check{H}_1(\mathbf{r}, \mathbf{r}') \phi_{\mathbf{1}}(\mathbf{r}') = E \phi_{\mathbf{1}}(\mathbf{r}), \quad (3.20)$$

with the  $4 \times 4$  matrix  $\check{H}_1(\mathbf{r}, \mathbf{r}')$  given by

$$\check{H}_1(\mathbf{r}, \mathbf{r}') = \begin{bmatrix} h_{\uparrow\uparrow}(\mathbf{r})\delta(\mathbf{r} - \mathbf{r}') & h_{\uparrow\downarrow}(\mathbf{r})\delta(\mathbf{r} - \mathbf{r}') & 0 & \Delta(\mathbf{r}, \mathbf{r}') \\ h_{\downarrow\uparrow}(\mathbf{r})\delta(\mathbf{r} - \mathbf{r}') & h_{\downarrow\downarrow}(\mathbf{r})\delta(\mathbf{r} - \mathbf{r}') & \Delta(\mathbf{r}', \mathbf{r}) & 0 \\ 0 & \Delta^*(\mathbf{r}, \mathbf{r}') & -h_{\uparrow\uparrow}^*(\mathbf{r})\delta(\mathbf{r} - \mathbf{r}') & h_{\uparrow\downarrow}^*(\mathbf{r})\delta(\mathbf{r} - \mathbf{r}') \\ \Delta^*(\mathbf{r}', \mathbf{r}) & 0 & h_{\downarrow\uparrow}^*(\mathbf{r})\delta(\mathbf{r} - \mathbf{r}') & -h_{\downarrow\downarrow}^*(\mathbf{r})\delta(\mathbf{r} - \mathbf{r}') \end{bmatrix}. \quad (3.21)$$

Solving this eigenvalue problem is equivalent to solving the full Bogoliubov-de Gennes equations. This form is also given without proof in [47].

We can further study the structure of (3.21) by explicitly writing it in block form

$$\check{H}_1(\mathbf{r}, \mathbf{r}') = \begin{bmatrix} \hat{h} & \hat{\Delta} \\ \hat{\Delta}^* & -\sigma_z \hat{h}^* \sigma_z \end{bmatrix}, \quad (3.22)$$

where  $\hat{h}$  is the single particle Hamiltonian given in (3.9) (multiplied by  $\delta(\mathbf{r} - \mathbf{r}')$ , and  $\hat{\Delta} = \Delta(\mathbf{r}, \mathbf{r}') \sigma_x$ . Please note that in the current form (3.20) the integrals make the eigenproblem somewhat intimidating. It simplifies a lot since for  $s$ -wave superconductors the integral over the superconducting gap gives a constant  $\Delta_0 e^{i\varphi}$  term, where  $\Delta_0 \in \mathbb{R}$  and  $\varphi$  being the superconducting phase. Moreover, the integral over the Dirac-delta distribution also collapses the integral to a single spatial dependence and in fact, on our domain of computation, where we assume homogeneous materials, the spatial is not present anymore.

In the form (3.22) the underlying structure becomes apparent. In absence of the superconductivity induced pair potential, there is no coupling between the electron-like and hole-like character of the quasiparticles. The top-left  $2 \times 2$  single-particle Hamiltonian then acts only on the electron-like

quasiparticles  $u_\uparrow, u_\downarrow$  and the bottom right  $2 \times 2$  block on the hole-like quasiparticles  $v_\uparrow, v_\downarrow$ . Moreover, as the topology induced spin-orbit coupling terms are contained within each single-particle Hamiltonian, they only introduce a coupling between two spin branches, but not a coupling between the electron-like and hole-like branches. The resulting matrix will be block diagonal. So in absence of superconductivity, we can utilize this apparent structure and solve the two  $2 \times 2$  blocks for electron- and hole-like quasiparticles separately, reducing the (algebraic) complexity. When there is a finite superconducting gap present, there is a coupling between the electron- and hole-like quasiparticle weights. The  $\hat{\Delta}$  terms in the upper right or lower left  $2 \times 2$  blocks to introduce the mixing of  $u$  and  $v$  terms. In this case, the  $4 \times 4$  eigenvalue problem has to be solved at once, and it can not be split into two separate  $2 \times 2$  problems.

The basis (3.19) that was used to cast the set of BdG equations in (3.18) to the matrix form in (3.21) is not the only feasible choice of basis we could have made. We shall refer to (3.19) as basis 1, but another basis will be discussed in section 3.3. The choice of basis will not affect possible derived physical observables, but it will prove to ease computations and certain interpretations.

## 3.2 Solutions to the Bogoliubov-de Gennes equations

Given the basis-dependent<sup>11</sup> matrix associated with the effective Hamiltonian, we now solve for plane wave eigensolutions for different single-particle Hamiltonians  $h_{\alpha\beta}$  corresponding to different types of quantum materials. First, we describe the plane-wave basis choice and introduce the procedure to solve the associated eigenproblem. In subsection 3.2.1 we consider the solutions for a topological insulator(TI) in absence of a magnetic field or superconductivity. After that in subsection 3.2.2 we introduce magnetic effects and consider a magnetic topological insulator (MTI). Finally, we study a superconducting topological insulator (STI) by introducing a nonzero  $s$ -wave superconducting energy gap in subsection 3.2.3. Since each BdG matrix has multiple eigensolutions, we distinguish each solution using a (set of) label(s). In the last part of this section (section 3.2.4), we combine and discuss all dispersion relations for the various materials and clarify these labels.

We consider a plane wave basis to go from real space to momentum

---

<sup>11</sup>In this section we work in basis 1. Basis 2 is discussed in section 3.3 and the plane-wave solutions to the BdG equation in basis 2 are given in the appendix A.

space. Until now, the discussion of superconductivity relied on the notion of momentum states, as seen in the introductory sections on superconductivity in 2.1.2 to 2.2. In chapter 3 however, we derived the Bogoliubov-de Gennes equations, the corresponding effective Hamiltonian and its associated matrix, which were all described in real space. To realize the transition from real space to momentum space we next expand our wave function in a plane wave basis

$$\phi(\mathbf{r}) = \begin{pmatrix} u_{\uparrow}(\mathbf{r}) \\ u_{\downarrow}(\mathbf{r}) \\ v_{\uparrow}(\mathbf{r}) \\ v_{\downarrow}(\mathbf{r}) \end{pmatrix} = \sum_{\mathbf{k}} \phi_{\mathbf{k}} e^{i\mathbf{k}\cdot\mathbf{r}}, \quad (3.23)$$

where we shift the space dependency to the exponential wave term  $e^{i\mathbf{k}\cdot\mathbf{r}}$ , and we are left with a (constant) coefficients  $\phi_{\mathbf{k}}$ . Mathematically speaking this is equivalent to a Fourier series expansion. A formal mathematical treatment of Fourier series is given [85] and a discussion in the context of solid-state physics is given in [70]. We will solve for the eigensolutions of matrices obtained after acting with matrices of the form (3.21) on plane-wave (3.23). The domain of computation is a two dimensional rectangle consisting of vertical interfaces between materials that extend infinitely far in the  $\pm y$  direction, this creates horizontally isolated slabs of connected materials. The material properties are assumed to be homogeneous in each isolated material, i.e. per material the Hamiltonian will be independent of  $\mathbf{r}$ .

Individual energy solutions are going to be of interest. We fix an energy  $E$  and through the dispersion relations we relate these to a  $\mathbf{k}$ -state. In the expansion (3.23), we will therefore consider the coefficient vector<sup>12</sup>,

$$\phi_{\mathbf{k}} = \begin{pmatrix} u_{0\uparrow} \\ u_{0\downarrow} \\ v_{0\uparrow} \\ v_{0\downarrow} \end{pmatrix}. \quad (3.24)$$

The full solution (3.23) will be a summation over the individual solutions for a fixed energy  $E$ . By examining the individual energy solutions, we will gain insight into the specific energies at which certain interesting features, e.g. resonances, might occur.

Recall that a hole(-like quasiparticle) propagates in the opposite direction. Here propagation refers to the plane waves moving for a fixed energy governed by  $e^{(i\mathbf{k}\cdot\mathbf{r} - Et/\hbar)}$ , so for the negative energy holes, the momentum is opposite to

---

<sup>12</sup>The label  $E(\mathbf{k})$  will be clear from context.

the direction of motion, in the coming we shall omit the  $Et$  term. To describe a hole(-like quasiparticle) traveling in the  $+\mathbf{k}$  direction, we therefore should consider  $e^{-i\mathbf{k}\cdot\mathbf{r}}$  in (3.24). Through the use the plane wave expansion, we have transformed (3.20) to an eigenproblem of the form

$$\begin{pmatrix} h_{\uparrow\uparrow} & h_{\uparrow\downarrow} & 0 & \Delta \\ h_{\downarrow\uparrow} & h_{\downarrow\downarrow} & \Delta & 0 \\ 0 & \Delta^* & -h_{\uparrow\uparrow}^* & h_{\uparrow\downarrow}^* \\ \Delta^* & 0 & h_{\downarrow\uparrow}^* & -h_{\downarrow\downarrow}^* \end{pmatrix} \begin{pmatrix} u_{0\uparrow} \\ u_{0\downarrow} \\ v_{0\uparrow} \\ v_{0\downarrow} \end{pmatrix} e^{i\mathbf{k}\cdot\mathbf{r}} = E \begin{pmatrix} u_{0\uparrow} \\ u_{0\downarrow} \\ v_{0\uparrow} \\ v_{0\downarrow} \end{pmatrix} e^{i\mathbf{k}\cdot\mathbf{r}}. \quad (3.25)$$

Recall that to get to this matrix form, the integrals in (3.20) and (3.21) all become trivial as mentioned in the supporting text. In the following sections, we will solve the Hamiltonian derived (in basis 1) from the Bogoliubov-de Gennes equations in a plane wave basis for the three mentioned materials, TI, MTI and STI. Note that here, we will derive the eigenfunctions in the case of a right moving (quasi)particle. Since a hole's momentum is opposite to its propagation direction, we get a minus sign difference between the electron- and hole-like quasiparticles in the wavevector in the exponential for the plane wave term in (3.25).

### 3.2.1 Topological insulator

Consider the eigenproblem (3.25) in two dimensions in absence of magnetic and superconducting effects. This means  $\Delta(\mathbf{r}) = 0$  and the magnetic term in the single particle Hamiltonian (3.9) vanishes. Moreover, we have the two-dimensional momentum vector with components  $k_x = k_{e,h} \cos \theta$  and  $k_y = k_{e,h} \sin \theta$ , where  $\theta$  denotes the positive angle between the  $x$  and  $y$  direction and  $k_{e,h} = |E \pm \mu|/(\hbar v_f)$  where the subscript  $e, h$  indicates the electron(-like) or hole(-like) excitations. Here the energy  $E$  is the energy of the excitation relative to the Fermi energy  $E_f$ . The eigenproblem reduces to two separate problems. For the electron block we find

$$\begin{pmatrix} -\mu & \hbar k_e v_f e^{-i\theta} \\ \hbar k_e v_f e^{i\theta} & -\mu \end{pmatrix} \begin{pmatrix} u_{0\uparrow} \\ u_{0\downarrow} \end{pmatrix} = E \begin{pmatrix} u_{0\uparrow} \\ u_{0\downarrow} \end{pmatrix}. \quad (3.26)$$

To illustrate the origin of the exponential term we consider the (1,2) entry. From the single particle Hamiltonian we have  $-i\hbar v_f(\sigma_x d/dx + \sigma_y d/dy)$  the (1,2) entry therein is,  $-i\hbar v_f(d/dx - id/dy)$ . This acts on  $e^{i(k_x x + k_y y)}$ , giving  $\hbar v_f(k_x - ik_y) = \hbar v_f k_e(\cos \theta - i \sin \theta) = \hbar k_e v_f e^{-i\theta}$ . This problem has two energy eigensolutions with corresponding eigenvectors

$$E_{e\pm}^{TI} = \pm \hbar k_e v_f - \mu \leftrightarrow \phi_{e\pm}^{TI}(x, y) = \frac{1}{\sqrt{2}} \begin{pmatrix} 1 \\ \pm e^{i\theta} \end{pmatrix} e^{ik_x x + ik_y y}. \quad (3.27)$$

where  $k_e = |E + \mu|/(\hbar v_f)$ . For the hole block we have

$$\begin{pmatrix} \mu & -\hbar k_h v_f e^{i\theta} \\ -\hbar k_h v_f e^{-i\theta} & \mu \end{pmatrix} \begin{pmatrix} v_{0\uparrow} \\ v_{0\downarrow} \end{pmatrix} = E \begin{pmatrix} v_{0\uparrow} \\ v_{0\downarrow} \end{pmatrix}, \quad (3.28)$$

with eigensolutions,

$$E_{h\mp}^{TI} = \mp \hbar k_h v_f + \mu \leftrightarrow \phi_{h\mp}^{TI}(x, y) = \frac{1}{\sqrt{2}} \begin{pmatrix} 1 \\ \pm e^{-i\theta} \end{pmatrix} e^{-ik_x x - ik_y y}, \quad (3.29)$$

where  $k_h = |E - \mu|/(\hbar v_f)$ . The  $\pm$  in the spinors and energy relations refers to the sign in front of the  $k$  term.

Later on, we will use the electron and hole (plane-)eigensolutions (3.27), (3.29) to represent wavefunctions. At an interface between two different materials we will construct a scattering problem by imposing the continuity of the wavefunctions on either side of the interface. Say we have a TI-MTI interface at  $(x, y) = (0, 0)$  and an electron coming in at an angle  $\theta$  and energy  $E$  from the TI-side, then to model e.g. normal reflection we equate

$$\phi_{e+}^{TI}(\theta) + r\phi_{e+}^{TI}(\pi - \theta) = t\phi_e^{MTI-}(\theta),$$

where  $r, t$  are the complex reflection and transmission coefficient associated with this reflection. The physical interpretation of all these labels is elaborated upon in section 3.2.4.

### 3.2.2 Magnetic topological insulator

Now we consider a nonzero magnetization oriented perpendicular to the two dimensional surface, i.e.  $\mathbf{m} = (0, 0, m_z)^T$ . The effect of the induced ferromagnetism on the 2D topological surface states leaves a notable imprint on the spinors. Correspondingly, the plane wave solutions do not propagate indefinitely in  $x$  anymore. For a sufficiently large magnetic energy gap, the plane waves will become evanescent in the  $x$ -direction. To allow for the possibility of evanescent waves, we now consider solutions proportional to  $e^{iq_j x + ik_y y}$ , where the label  $j$  indicates electrons or holes, and  $q_j$  is complex. When  $q_j$  has an imaginary part, say  $q_j = k_x + i\kappa$  (for two real numbers  $k_x$  and  $\kappa$ ), the exponential term becomes evanescent  $e^{ik_x x - \kappa x}$ . In this case, we obtain a decreasing wave in the positive  $x$ -direction. Strictly speaking, an evanescent wave is always decreasing, but we allow for increasing waves too. We shall refer to these as increasing evanescent waves to avoid confusion, with the caveat that this is linguistic nonsense. Recall that our domain

computation is a two-dimensional rectangle consisting of vertical interfaces between materials that extend sufficiently far in the  $\pm y$  direction, such that we can assume translation invariant in  $y$ , meaning that  $k_y$  is conserved. This creates horizontally isolated slabs of connected materials, so all interesting physics occurs along the  $x$ -direction.

The MTI electron eigenproblem is given by

$$\begin{pmatrix} m_z - \mu_m & \hbar v_f (-ik_e \sin(\theta) \mp q_e) \\ \hbar v_f (ik_e \sin(\theta) \mp q_e) & -m_z - \mu_m \end{pmatrix} \begin{pmatrix} u_{0\uparrow} \\ u_{0\downarrow} \end{pmatrix} = E \begin{pmatrix} u_{0\uparrow} \\ u_{0\downarrow} \end{pmatrix}. \quad (3.30)$$

There are two possible signs of  $\mp q_e$  corresponding to an increasing or decreasing evanescent MTI wave. The energy dispersion relations (eigenvalues) do not depend on this sign, but the spinors do. Taking these signs into consideration, each problem has two energy eigensolutions with corresponding eigenvectors

$$\begin{aligned} E_{e\pm}^{MTI} &= -\mu_m \pm \sqrt{m_z^2 + \hbar^2 k_e^2 v_f^2 \sin^2(\theta) + \hbar^2 q_e^2 v_f^2} \\ \leftrightarrow \phi_e^{MTI,\pm}(x,y) &= \frac{1}{\sqrt{A_{e\pm}}} \begin{pmatrix} -i\hbar k_e v_f \sin(\theta) \mp \hbar q_e v_f \\ E - m_z + \mu_m \end{pmatrix} e^{\mp i q_e x + i k_y y}, \end{aligned} \quad (3.31)$$

where  $A_{e\pm}$  is used for normalization and the  $\pm$  in the spinors corresponds to the increasing or decreasing evanescent waves. We solve for  $q_e$  in the dispersion relation and define

$$q_e = \frac{\sqrt{-m_z^2 - (\hbar v_f k_e \sin \theta)^2 + (E + \mu_m)^2}}{\hbar v_f}. \quad (3.32)$$

When  $m_z$  is large enough to make  $q_e$  complex, we can pick the plus (minus) sign to end up with a decreasing evanescent wave in the positive (negative)  $x$ -direction. Essentially we now have an additional two-fold branch of solutions, one for each sign we choose for  $q_e$ . The sign choice does not alter the dispersion relation, but it does change the sign of  $q_e$  in the spinor and in the exponential term. So we introduce the notation  $\phi_e^{MTI,\pm}(x,y)$  where the  $\pm$  corresponds to an increasing (decreasing) wave in the positive  $x$ -direction. We have dropped the lowercase  $\pm$  to distinguish between the two signs in  $E_{e\pm}^{MTI}$  because the two corresponding eigenvectors are identical. Please note that therefore the  $\pm$  sign in  $\phi_e^{MTI,\pm}(x,y)$  corresponds to the  $\mp$  sign in front of  $q_e$  which we then insert in the spinors in (3.31).

Similarly when analysing the hole block we find

$$\begin{pmatrix} -m_z + \mu_m & \hbar v_f (i k_h \sin(\theta) \pm q_h) \\ \hbar v_f (-i k_h \sin(\theta) \pm q_h) & m_z + \mu_m \end{pmatrix} \begin{pmatrix} v_{0\uparrow} \\ v_{0\downarrow} \end{pmatrix} = E \begin{pmatrix} v_{0\uparrow} \\ v_{0\downarrow} \end{pmatrix}. \quad (3.33)$$

Recall that the  $\pm$  sign indicates whether we work with an increasing or decreasing evanescent wavefunction. This problem has two energy eigen-solutions with corresponding eigenvectors

$$\begin{aligned} E_{h\pm}^{MTI} &= \mu_m \pm \sqrt{m_z^2 + \hbar^2 k_h^2 v_f^2 \sin^2(\theta) + \hbar^2 q_h^2 v_f^2} \\ \leftrightarrow \phi_h^{MTI,\pm}(x, y) &= \frac{1}{\sqrt{A_{h\pm}}} \begin{pmatrix} -i \hbar k_h v_f \sin(\theta) \mp \hbar q_h v_f \\ -E - m_z + \mu_m \end{pmatrix} e^{\mp i q_h x - i k_y y}, \end{aligned} \quad (3.34)$$

where  $A_{h\pm}$  is used for normalization and we solve for  $q_h$  in the dispersion relation

$$q_h = \pm \frac{\sqrt{-m_z^2 - (\hbar v_f k_h \sin \theta)^2 + (E - \mu_m)^2}}{\hbar v_f}. \quad (3.35)$$

Again the same sign convention for  $\phi_h^{MTI\pm}(x, y)$  as for the electrons will be used.

As a limiting case we take  $m_z \rightarrow 0$ , then the dispersion relations return to that of a TI. Moreover,  $q_{e,h} \rightarrow \pm k_{e,h} |\cos \theta| = k_x$  (for  $\theta \in (-\pi/2, \pi/2)$ ), then upon dividing the MTI spinors by  $k_{e,h} e^{\pm i\theta}$ , if we choose the appropriate sign depending on which branch we would like to compare, we retrieve the TI spinors.

### 3.2.3 Superconducting topological insulator

Next we consider a topological insulator in close contact with an  $s$ -wave superconductor. Due to the proximity effect superconductivity is induced into the 2D topological surface states. For a spin singlet  $s$ -wave superconductor, the superconducting energy gap is given by

$$\Delta = \Delta_0 e^{i\varphi}, \quad (3.36)$$

for a real valued  $\Delta_0$  and  $\varphi$ . The  $\varphi$  term is included to model the phase of the superconductor. As mentioned before,  $\Delta$  couples the electron- and hole-like components in the associated Hamiltonian matrix. For the STI eigenvectors one needs to solve the entire  $4 \times 4$  matrix eigenproblem (3.25). For STI this

problem reads

$$\begin{pmatrix} -\mu_s & \hbar k v_f e^{-i\theta_s} & 0 & \Delta_0 e^{i\varphi} \\ \hbar k v_f e^{i\theta_s} & -\mu_s & \Delta_0 e^{i\varphi} & 0 \\ 0 & \Delta_0 e^{-i\varphi} & \mu_s & -\hbar k v_f e^{i\theta_s} \\ \Delta_0 e^{-i\varphi} & 0 & -\hbar k v_f e^{-i\theta_s} & \mu_s \end{pmatrix} \begin{pmatrix} u_{0\uparrow} \\ u_{0\downarrow} \\ v_{0\uparrow} \\ v_{0\downarrow} \end{pmatrix} = E \begin{pmatrix} u_{0\uparrow} \\ u_{0\downarrow} \\ v_{0\uparrow} \\ v_{0\downarrow} \end{pmatrix}. \quad (3.37)$$

As frequently mentioned, the momenta considered in the superconducting regime are in relative distance close to  $k_f$ . The spread about  $k_f$  in the dispersion figures 10 is grossly exaggerated to illustrate the subtle features. To ease the discussion in the case of an STI we employ the so-called Andreev approximation, i.e., in momentum space the relevant processes occur approximately around  $k_f$  for both electron- and hole-like quasiparticles. Hence to the lowest order approximation, we describe them both by a single momentum  $\mathbf{k}$  with 2-norm  $k$ . This means that now we take the wavevectors equal in magnitude for the electron- and hole-like quasiparticle blocks in the matrix. Moreover, we have introduced  $\theta_s$ , which similar to  $\theta$  in the TI, is the angle between the  $x$  and  $y$  momenta. The angle  $\theta_s$  depends on the chemical potential in the STI,  $\mu_s$ . The two geometrical angles are related by their chemical potentials,  $\mu_s \sin \theta_s = \mu \sin \theta$ .

The above system can be simplified using a unitary transformation. We denote the matrix in (3.37) by  $\check{H}_{STI}$ . Consider the unitary matrix

$$\check{U}_1 = \text{diag}(U_1, U_2), \quad (3.38)$$

where the two unitary matrices  $U_1$  and  $U_2$  are given by.

$$U_1 = \frac{1}{\sqrt{2}} \begin{pmatrix} -1 & e^{-i\theta_s} \\ e^{i\theta_s} & 1 \end{pmatrix}, \quad (3.39)$$

$$U_2 = \frac{1}{\sqrt{2}} \begin{pmatrix} -1 & -e^{i\theta_s} \\ -e^{-i\theta_s} & 1 \end{pmatrix}. \quad (3.40)$$

The unitary transformation gives us the eigenproblem

$$\check{H}_{STI}^{Trans} = \check{U}_1 \check{H}_{STI} \check{U}_1 = \begin{pmatrix} -\hbar k v_f - \mu_s & 0 & 0 & -\Delta_0 e^{i\varphi} \\ 0 & \hbar k v_f - \mu_s & -\Delta_0 e^{i\varphi} & 0 \\ 0 & -\Delta_0 e^{-i\varphi} & -\hbar k v_f + \mu_s & 0 \\ -\Delta_0 e^{-i\varphi} & 0 & 0 & \hbar k v_f + \mu_s \end{pmatrix}. \quad (3.41)$$

All this essentially says is that  $\check{H}_{STI}^{Trans}$  and  $\check{H}_{STI}$  are similar matrices related by (3.41). It is a general property[86] of similar matrices that if  $\mathbf{x}$  is an eigenvector of (3.41), then  $\check{U}_1 \mathbf{x}$  is an eigenvector of the original problem (3.37)

with the same eigenvalue.

The transformed matrix (3.41) has more zero entries than the original matrix. In fact, we have decoupled the  $4 \times 4$  eigenproblem into two 2 eigenproblems. This is reflected by the fact that in the transformed form the first and fourth element in the basis representation (3.19)  $u_{0\uparrow}$  and  $v_{0\downarrow}$  get coupled, similarly for the second and third element. The algebraic complexity is reduced by this. We find the following four eigenvalues

$$E_{\pm\pm}^{STI} = \pm\sqrt{\Delta_0^2 + (\mu_s \pm \hbar k v_f)^2}, \quad (3.42)$$

with corresponding eigenvectors

$$\begin{aligned} & \left(-\frac{\Delta_0 e^{i\varphi}}{\chi_{\pm}}, 0, 0, 1\right)^T, \\ & \left(0, -\frac{\Delta_0 e^{i\varphi}}{\chi_{\pm}}, 1, 0\right)^T. \end{aligned} \quad (3.43)$$

The first and second set of  $\pm$  signs in the subscript indicate the sign of the energy and momentum respectively. Here we have defined

$$\chi_{\pm} := E \pm \chi = E \pm \sqrt{E^2 - \Delta_0^2}. \quad (3.44)$$

Transforming this back to the original problem we find

$$\begin{aligned} E_{\pm+}^{STI} = \pm\sqrt{\Delta_0^2 + (\mu_s - \hbar k v_f)^2} & \leftrightarrow \phi_{+}^{STI,\pm}(x, y) = \frac{1}{2} \begin{pmatrix} 1 \\ e^{i\theta_s} \\ \frac{\chi_{\pm}}{\Delta_0} e^{i\theta_s} e^{-i\varphi} \\ \frac{\chi_{\pm}}{\Delta_0} e^{-i\varphi} \end{pmatrix} e^{ik_x x + ik_y y} e^{\pm\chi x}, \\ E_{\pm-}^{STI} = \pm\sqrt{\Delta_0^2 + (\mu_s + \hbar k v_f)^2} & \leftrightarrow \phi_{-}^{STI,\pm}(x, y) = \frac{1}{2} \begin{pmatrix} 1 \\ -e^{i\theta_s} \\ -\frac{\chi_{\mp}}{\Delta_0} e^{i\theta_s} e^{-i\varphi} \\ \frac{\chi_{\mp}}{\Delta_0} e^{-i\varphi} \end{pmatrix} e^{ik_x x + ik_y y} e^{\pm\chi x}. \end{aligned} \quad (3.45)$$

The  $\pm$  sign labels in the eigenvectors superscript correspond to the increasing or decreasing nature of the wave term as function of  $x$ . Similar as in the MTI we have an increasing or decreasing evanescent wave in the  $x$ -direction. So this  $\pm$ -sign in the superscript corresponds to the sign of the  $\chi_{\pm}$  in the eigenvector and the sign in the  $e^{\pm\chi x}$  term. The  $\chi$  term comes from solving (3.42) for  $k$ :

$$\hbar k v_f = \pm\mu_s \pm \sqrt{E^2 - \Delta_0^2} := \pm\hbar k_x v_f \pm \chi, \quad (3.46)$$

where  $k_x = \mu_s \cos \theta$ . The subscript labeled sign indicates the  $k$ -branch, this will be elaborated in the next section when we discuss the dispersion relations.

As a sanity check, we take the limit  $\Delta_0 \rightarrow 0$ . In (3.42) we immediately see that we retrieve the linear TI dispersion relations. To compare the STI spinors to the TI spinors we have to consider  $\phi_+^{STI,-}(x, y)$  and  $\phi_-^{STI,+}(x, y)$ . The reason for this is that they describe an evanescent wave decreasing in their propagation directions. In the limit  $\Delta_0 \rightarrow 0$  we have  $\frac{\chi_-}{\Delta_0} e^{i\varphi} \rightarrow 1$ . We retrieve the two-dimensional electron and hole spinors but are now stacked vertically to form a single four-dimensional spinor. Next, we compare the dispersion relations in detail.

### 3.2.4 Dispersion relations

In the previous section, we derived the dispersion relations for a regular 3D topological insulator, one in the presence of a ferromagnetic insulator, and one close to a conventional superconductor, here we discuss and compare their notable features. Figure 19 shows from left to right the possible energy branches for a TI, MTI and STI. The solid (dashed) lines indicate electron-like quasiparticles (hole-like quasiparticles). The branches with the associated physically propagating (quasi)particle wavefunction are tabulated in 1. We note that the spinors associated with the negative and positive energy solutions derived in section 3.2 are identical. The reflection in the line  $E = 0$  in figure 19 thus leaves the solutions unchanged. This is a manifestation of the particle-hole symmetry briefly introduced in the section 1.2. There we noted that particle-hole symmetry is one of the main symmetries a condensed matter system should obey to potentially host Majorana modes, symmetries of the underlying Hamiltonian are discussed in section 3.3.

We first discuss the TI and then consider the MTI and STI dispersion relations as deviations from the TI. In section 2.3 the global features of a topological material were discussed, such as its linear dispersion relation and the Dirac point, which can be seen in the left panel in figure 19. Recall that the group velocity is defined by  $\mathbf{v}_g = \frac{1}{\hbar} \nabla_{\mathbf{k}} E_{\mathbf{k}}$ . Hence the sign of the slope (derivate) in figure 19 corresponds to the particle's travel direction. For the TI, the four branches we can identify are two electron branches (solid lines) and two hole (dashed lines) branches. A right travelling electron (hole) travelling would be situated on the right (left) green (orange) solid (dashed) branch. The corresponding eigenvalue (and related eigenvector) are  $E_{e+}^{TI}$  and  $E_{h-}^{TI}$  in (3.45) for the electron and the hole respectively. The difference in the  $k$ -branch subscript sign between the holes and electrons is because for holes

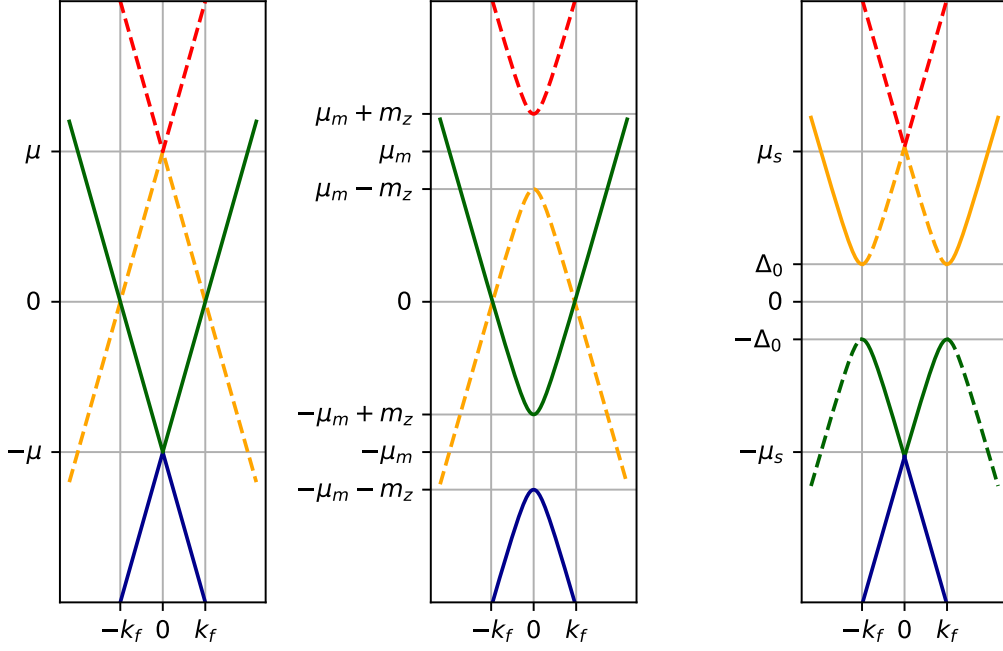


Figure 19: A figure showing the dispersion relations for a TI, MTI, and STI in the case  $k_y = 0$  with energy on the vertical axis and  $k_x$  on the horizontal axis. A vertical shift of  $-E_f$  is taken to bring the  $y$ -axis to the origin. The solid and dashed lines indicate an electron- or hole-like branch respectively. The dispersion relations for a topological insulator are from left to right in absence of external effects, in an external out of plane magnetic field and near a conventional superconductor. Note the effect of the particle-hole symmetry under the reflection in  $E = 0$  positive and negative  $E$  branches.

their momenta are opposite to their travel direction.

As we introduce ferromagnetic effects, a magnetic energy gap of  $m_z$  around the chemical potential is induced in the MTI. For a sufficiently large  $m_z$  there is an energy range where no states are allowed to reside. The absence of states in this energy range means that inbound electrons from a TI, in e.g. a TI-MTI bilayer, have a finite probability to undergo normal reflections at the interface. We can identify the same four branches and the corresponding propagating particles as described in the TI.

The superconducting energy gap,  $\Delta_0$ , also introduces a gap in the dispersion relation, but it is essentially different from the magnetic gap. The  $\Delta_0$  gap forms about the Fermi energy whereas the magnetic gap opened about the chemical potential. In the low energy limit  $\mu_s \gg \Delta_0$ , the STI spectra resemble that of a spinless  $p_x + ip_y$  superconductor [1], [43].

	TI	MTI	STI
<b>Right</b> $e$ (Green solid)	$\phi_{e+}^{TI}, (-E, k)$	$\phi_e^{MTI, \pm}, (-E, k)$	$\phi_+^{STI, \pm}, (-E, k)$
<b>Right</b> $h$ (Orange dashed)	$\phi_{h-}^{TI}, (E, -k)$	$\phi_h^{MTI, \pm}, (E, -k)$	$\phi_-^{STI, \pm}, (E, -k)$
<b>Left</b> $e$ (Green solid)	$\phi_{e-}^{TI}, (-E, -k)$	$\phi_e^{MTI, \pm}, (-E, -k)$	$\phi_-^{STI, \pm}, (-E, -k)$
<b>Left</b> $h$ (Orange dashed)	$\phi_{h-}^{TI}, (E, k)$	$\phi_h^{MTI, \pm}, (-E, k)$	$\phi_-^{STI, \pm}, (E, k)$

Table 1: The correspondence between the branches shown in figure 19, and the propagation direction of electron- and hole-like (quasi) particles. We consider both left (negative  $x$ -direction) and right (positive  $x$ -direction) moving electrons and holes. The indicated  $(\pm E, \pm k)$  label corresponds to the global sign of both quantities, i.e. as a mean to distinguish the four quadrants in the figure.

Also, we see that in both the TI and MTI there is a clear distinction between electron and hole branches, yet in the STI case this distinction is lost and we see that in the right panel in figure 19 at an energy of  $E_f \pm \Delta$ , there is a transition from the electron-like to a hole-like quasiparticle branch. We can therefore only identify the electron- and hole-like branches in the limiting behaviour (far) away from this transition point. Per energy sign, we can identify two STI branches, one centred about each sign of  $\pm k_f$ .

A notable difference between the two STI branches is their group velocity,  $\mathbf{v}_g = \frac{1}{\hbar} \frac{\partial E}{\partial \mathbf{k}}$ . Note that for electron-like excitations the group velocity has the same sign as  $k_x$ , but for holes, the group velocity is opposite to the momentum. Considering this, we see in the range of  $E_f \pm \Delta$ , around the energies where the branch transition occurs, the group velocity is reversed. This gives rise to Andreev Reflections which we considered in section 2.2. We can identify an electron (hole) propagating in the positive  $x$  direction situated on the right (left) green solid (orange dashed) branch. The corresponding eigenvector is  $\phi_+^{STI, \pm}$  and  $\phi_-^{STI, \pm}$  in (3.45) for the electron and the hole respectively.

To summarize, we derived the BdG equations for superconducting magnetic topological materials and retrieved a set of equations equivalent to [47]. Furthermore, by solving for the eigensolutions in plane-wave basis to the BdG equations in matrix form, we found the TI, MTI, and STI dispersion relations we predicted to find based on literature [66] [78] [1]. In particular, it was shown that  $s$ -wave superconductivity induces a  $p$ -wave-like dispersion relation in a 3D TI. In the remaining chapters, we will use the derived wavefunctions to solve scattering problems by imposing the continuity of the wavefunctions at the interfaces present in the scattering problem.

### 3.3 Time reversal- and particle-hole symmetry

We close the discussion on the BdG equations by studying the symmetries of the Hamiltonian. The symmetries of Hamiltonians in condensed matter physics allow for the complete ten-fold classification of the topological invariants [87]. Without going into too much detail here, we focus on the particle-hole symmetry and time-reversal symmetry because, as stated in the introduction, Read and Green [31] showed that Majorana modes emerge in spinless  $p$ -wave superconductors with broken time-reversal symmetry. Particle-hole symmetry is required to get symmetric energy states about the Fermi level, such that as the energy (relative to  $E_f$ ) goes to zero, there are states at zero energy [88].

To facilitate the analysis and to help with the interpretation of the findings we switch to an alternative basis. The BdG equations expressed in basis 1 as shown in (3.19)-(3.21) can be written in a different basis, which we call basis 2. Mathematically speaking, there is a unitary transformation relating both bases. Hence the resulting mathematics, and thus observable physics, should be the same. The benefit of this change of basis is twofold. On the one hand, the physical interpretation of the quasiparticle charge carriers can be made explicit, i.e., in this alternative basis the time-reversal symmetry is made apparent [89]. On the other hand, certain results derived in this second basis will become simpler (as will be shown and discussed in the results chapter later on). In this section, we will first establish the mathematical relationship between the two bases and then reflect on the interpretation of the basis in light of the symmetries of the resulting BdG Hamiltonian.

#### 3.3.1 Basis 2

We wrote the BdG equation (3.18) in a matrix-vector form using basis vector (3.19). Similarly we can use an alternative basis

$$\phi_2(\mathbf{r}) = \begin{pmatrix} u_\uparrow(\mathbf{r}) \\ u_\downarrow(\mathbf{r}) \\ v_\downarrow(\mathbf{r}) \\ -v_\uparrow(\mathbf{r}) \end{pmatrix}. \quad (3.47)$$

In blue we indicate the difference to basis 1. We shall refer to this as basis 2, and it is related to basis 1 as follows

$$\boldsymbol{\phi}_2 = \text{diag} [\hat{\sigma}_0, i\hat{\sigma}_y] \boldsymbol{\phi}_1. \quad (3.48)$$

Using basis 2, we can write

$$\int d\mathbf{r}' \check{H}_2(\mathbf{r}, \mathbf{r}') \boldsymbol{\phi}_2(\mathbf{r}') = E \boldsymbol{\phi}_2(\mathbf{r}), \quad (3.49)$$

with the Hamiltonian in matrix form

$$\check{H}_2(\mathbf{r}, \mathbf{r}') = \begin{bmatrix} h_{\uparrow\uparrow}(\mathbf{r})\delta(\mathbf{r}-\mathbf{r}') & h_{\uparrow\downarrow}(\mathbf{r})\delta(\mathbf{r}-\mathbf{r}') & \Delta(\mathbf{r}, \mathbf{r}') & 0 \\ h_{\downarrow\uparrow}(\mathbf{r})\delta(\mathbf{r}-\mathbf{r}') & h_{\downarrow\downarrow}(\mathbf{r})\delta(\mathbf{r}-\mathbf{r}') & 0 & -\Delta(\mathbf{r}', \mathbf{r}) \\ \Delta^*(\mathbf{r}, \mathbf{r}') & 0 & -h_{\uparrow\uparrow}^*(\mathbf{r})\delta(\mathbf{r}-\mathbf{r}') & -h_{\downarrow\uparrow}^*(\mathbf{r})\delta(\mathbf{r}-\mathbf{r}') \\ 0 & -\Delta^*(\mathbf{r}', \mathbf{r}) & -h_{\uparrow\downarrow}^*(\mathbf{r})\delta(\mathbf{r}-\mathbf{r}') & -h_{\downarrow\downarrow}^*(\mathbf{r})\delta(\mathbf{r}-\mathbf{r}') \end{bmatrix}. \quad (3.50)$$

We observe that if the relation (3.49) holds for the corresponding matrix (3.50), the alternative formulation is equivalent to the original BdG equations (3.18). A thorough analysis as done for basis 1 in section 3.1.6 shows that the matrix  $\check{H}_2(\mathbf{r}, \mathbf{r}')$  is indeed of the right form, but we can simply verify this by applying the basis transformation (3.48). Let  $T_{1 \rightarrow 2} := \text{diag} [\hat{\sigma}_0, i\hat{\sigma}_y]$  be the invertible change of basis matrix, and consider the Hamiltonian in matrix form expressed in basis 1 in (3.22). Then, dropping spatial labels, the BdG Hamiltonian expressed in basis 2 is given by.

$$\check{H}_2 = T_{1 \rightarrow 2} \check{H}_2 T_{1 \rightarrow 2}^{-1} = \begin{bmatrix} \hat{h} & \Delta \sigma_z \\ \sigma_z \Delta^* & -\sigma_x \hat{h}^* \sigma_x \end{bmatrix} \quad (3.51)$$

This is equal to (3.50) if we recall that  $\hat{h}$  is the single-particle Hamiltonian (3.9) and  $\sigma_{x,z}$  are the Pauli spin matrices. The spinors described in basis 2 will change according to the transformation (3.48). We note that in absence of the coupling of the electron- and hole-like terms due to a superconducting energy gap term  $\Delta_0$  the identity operator in (3.48) acts trivially on the 'electron (1,1) block' in (3.51). Thus the resulting TI and MTI electron spinors in both bases will be the same in absence of superconductivity. However, the hole spinors and the STI spinors will look different in basis 2, but describe the equivalent physics. In fact they are related by (3.48). In appendix A we give these spinors in basis 2.

### 3.3.2 Symmetries of the Hamiltonian

In the alternative basis (3.47) we can consider the hole operators as time-reversed electron operators [90]. Time reversal is the process of flipping the

sign of the time in the governing equations, i.e.  $t \rightarrow -t$ . Physically speaking the time-reversed process of, e.g., an electron reflection at an interface is simply the same process but with the arrow of time-reversed. All processes in particle physics were long considered to be symmetric under time reversal, i.e., the dynamical evolution of a process forward in time is equivalent to the same process backwards in time. However, the weak interaction was shown to violate time-reversal symmetry [91]. Magnetic effects, consider for instance induced ferromagnetism, break time-reversal symmetry, lifting degeneracies in the system [92].

To make this explicit [87]: "time reversal symmetry can be expressed in terms of  $\check{H}$  : a system is invariant under time reversal symmetry if and only if the complex conjugate of the first quantized Hamiltonian  $\check{H}^*$  is equal to  $\check{H}$  up to a unitary rotation  $U$ , i.e."

$$\mathcal{T} : U_T^\dagger \check{H}^* U_T = +\check{H}. \quad (3.52)$$

For the case  $U_T = \sigma_x \otimes \sigma_x$ , where  $\otimes$  denotes the tensor product, we have,

$$\mathcal{T} : U_T^\dagger \check{H}_2^* U_T = -\check{H}_2, \quad (3.53)$$

which means that the Hamiltonian breaks time reversal symmetry (TRS). Magnetism breaks TRS [91], and we model induced ferromagnetism in the MTI, it comes as no surprise that the Hamiltonian breaks TRS.

The dispersion relation in section 3.2.4 were shown to be symmetric under the reflection of the curves in figure 19 in the line  $E = 0$ , which is the manifestation of particle-hole symmetry (PHS). Similar to TRS, [87]: "a system is invariant under particle-hole (or:charge-conjugation) symmetry if and only if the complex conjugate of the Hamiltonian  $\check{H}^* = \check{H}^T$  is equal to minus  $\check{H}$  up to a unitary rotation  $U_C$ , i.e."

$$\mathcal{C} : U_C^\dagger \check{H}^* U_C = -\check{H}. \quad (3.54)$$

By using the same unitary matrix  $U_C = U_T$  as in (3.52) we show,

$$\mathcal{C} : U_C^\dagger \check{H}_2^* U_C = -\check{H}_2, \quad (3.55)$$

which means that the Hamiltonian obeys PHS. Following the classification scheme [87], the breaking of TRS and obeying of PHS (with  $U_C^2 = +I_{4 \times 4}$ ) the BdG Hamiltonian falls in the  $D$ -symmetry-class.

Particle hole symmetry can be phrased as the notion that creating a quasiparticle with energy  $E$  or removing one with energy  $-E$  are identical operations. Suppose there is a solution  $\phi_i$  with a positive energy solution  $E_i$  then PHS enforces the existence of a solution with energy  $E_j = -E_i$  and corresponding  $\phi_j$  for some  $j$  with the relation  $\phi_j = \mathcal{C}\phi_i$  and  $\phi_j = \phi_i^\dagger$  [43].

As an illustration we consider the TI spinors in (3.27) and (3.29). We see that if we ignore normalization and set  $\hbar k_e v_f = \hbar k_h v_f \equiv \tilde{k}$  (which is valid since  $\mu \gg E$ ) that given the electron dispersion relations  $E_{e\pm}^{TI} = \pm\tilde{k} - \mu$  with corresponding eigenvectors  $\phi_{e\pm}^{TI} = (1, \pm e^{i\theta})^T$  that we have the particle(electron) hole symmetric pairs with opposing energies for the holes:  $E_{h\pm}^{TI} = -(\pm\tilde{k} - \mu)$  with the eigenvectors  $\phi_{h\pm}^{TI} = (1, \pm e^{-i\theta})^T = \mathcal{C}\phi_{e\pm}^{TI}$ . The same can be shown for the MTI and STI spinors. Thus the BdG Hamiltonian indeed has PHS.

The importance of TRS and PHS are paramount in the discussion of potential Majorana states in a system described by the BdG Hamiltonian. Since we defined the Majorana operator as the simultaneous creation and annihilation operator of a Majorana state ( $\gamma = \gamma^\dagger$ ), PHS restricts the existence of a Majorana state to be only possible at  $E = 0$  (because  $E = 0$  is, trivially, the only energy s.t.  $\gamma(-E) = \gamma^\dagger(E)$ ). Following the work by Read and Green [31] the emergence of Majorana modes requires the breaking of TRS. The fact that the derived BdG Hamiltonian in matrix form simultaneously obeys PHS but breaks TRS validates the choice to study heterostructures described by this Hamiltonian. For elaborate discussions on TRS and PHS in the context of condensed matter physics, the reader is referred to [30], [43], [69], [87], [88], or [89].

## 4 Designing and implementing a symbolic tool

The previous chapter set the complete theoretical stage for the further quantitative analysis in this thesis. In this chapter we describe the custom made tool that, given a superconducting topological junction, automates the various steps required to go from the equations (BdG in chapter 3) and processes (Andreev scattering in section 2.2.1) to the computation of physical quantities. The goal is to be able to compute quantities such as the reflection coefficient of electronic wavefunctions at an interface or the transmission of an incoming electron through a complete superconducting topological junction, consisting of several slabs of varying material, as a function of various tune-able parameters. These theoretical results could then for instance be used to obtain a prediction of certain resonance peaks in an  $I, V$  (current vs voltage) curve in an experimental realization of the studied junctions.

The tool consists of three main parts. First we solve for the complex wavefunctions per material under investigation based on the BdG equations. Next we piece together the various materials at the vertical interfaces by requiring the continuity of the wavefunctions at each interface. Finally, the resulting set of equations acquired by imposing continuity are cast into a linear system and solved for the complex wavefunction amplitudes. These can be considered as reflection or transmission coefficients as will be detailed momentarily.

Before we describe the working of the tool in detail, we first sketch the route (section 4.1) from the equations and processes to physical predictions we have automated using the tool. Here, we discuss the vast amount of various steps, which individually might be simple, but due to their extensive length are tedious, prone to error, and time consuming to manually execute if that is even possible in any manner. Next we elaborate on the tool's motivation and the underlying assumptions and resulting limitations in section 4.2. The tool itself is described in section 4.3. In the last section (4.4) we validate the tool's working by comparing intermediate results (e.g. wavefunctions) to results found in literature or derived by hand. For further validation various results in literature are re-derived using the tool, moreover in the upcoming results (chapter 5) the tool is used to derive a number of entirely novel results.

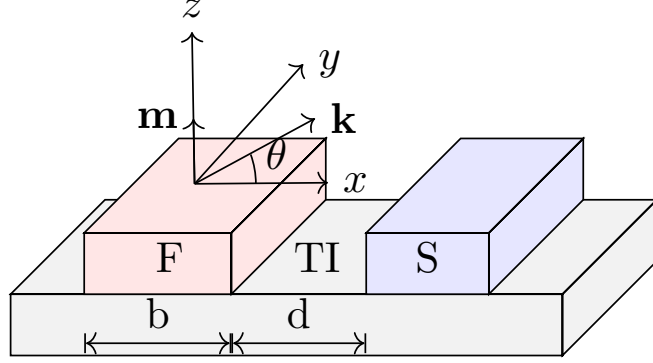


Figure 20: Simplistic schematic of a superconducting topological junction. From left to right the system consists of a MTI, TI and STI. The STI and MTI are formed through the proximity effect by the ferromagnetic insulator (F) and s-wave superconductor (S) stacked vertically on top of the 3D topological insulator (TI). The width of the MTI and the middle TI segment are indicated. The axis system is illustrated such that  $\mathbf{k}$  is in the 2D  $xy$ -plane and the magnetic orientation in F is along  $z$ .

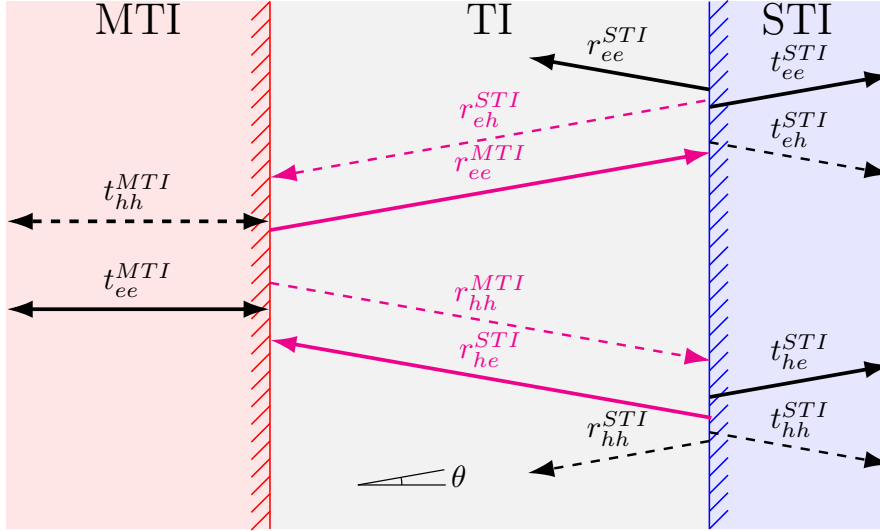


Figure 21: The schematic representation showing the 2D  $(x, y)$  top-view of the topological insulator ‘set-up’ depicted in figure 20. We focus here on the MTI-TI-STI part of figure 20, in principle there can still be TI slab on the left side of the MTI. This figure illustrates the possible types of reflections and transmission occurring in a ballistic 2D MTI-TI-STI junction. The solid and dashed lines refer to electron and hole transport respectively. The indicated angle  $\theta$  is defined for electrons relative to the positive  $x$ -direction. The Andreev bound state is indicated by the magenta colored reflection coefficients in the middle TI. At the MTI side normal reflection for both electrons and holes can occur, whereas at the STI side both normal and Andreev reflections are possible.

## 4.1 Calculation route

All systems we try to model are made up of various quantum materials bordering vertically in a 2D domain. We model the wavefunctions in each material separately using the Bogoliubov-de Gennes equations (see chapter 3). We connect the separate wavefunctions by requiring continuity at each interface. To sketch the kind of computations automated using the tool, we consider for example the system (figure 20) consisting of a 3D topological insulator with a ferromagnetic insulator and a superconductor on top of it. This induces ferromagnetism and  $s$ -wave superconductivity in the 2D TI surface states, forming a MTI-TI-STI system. It is obtained by replacing the left superconducting lead in the Josephson junction 3. The TI part extending on the left side now acts as a lead. In particular, we are interested in the formation of Andreev bound states due to charge carriers entering the middle TI slab, of width  $d$ , by tunneling in from the left.

Figure 21 is the top-view of figure 20 showing the scattering processes occurring in the 2D surface states. The angle  $\theta$  is defined w.r.t. the positive  $x$ -axis, i.e.  $\tan(\theta) = \frac{k_y}{k_x}$  is the ratio of the momentum components. Due to the Andreev reflection at the TI-STI-interface and the normal reflection at the MTI-TI-interface an Andreev bound state (see section 2.2.1) can occur. The computations, manipulations, and steps needed to go from the system, its constituent materials to possible scattering mechanisms are:

1. For each unique material  $m$  in the system we specify the BdG equations in matrix form (equation (3.20)) and solve them algebraically in plane wave basis for the eigensolutions  $\{(E_0^m, \phi_0^m), (E_1^m, \phi_1^m), \dots\}$ . In general we find algebraic expressions for the wavefunction eigensolutions to a specified material. In case the materials are an TI, MTI and STI, their wavefunctions are given in section 3.2 (basis 1) and appendix A (basis 2).
2. Per material  $m$  we categorize the set of eigensolutions  $\{(E_0^m, \phi_0^m), (E_1^m, \phi_1^m), \dots\}$  based on the sign of the energy, and group velocity ( $\mathbf{v}_g = \partial E / \partial \mathbf{k}$ ). By this categorization we can differentiate between left and right propagating particle wavefunctions. The various dispersion relations are discussed in detail in section 3.2.4.
3. Identify the particles taking part in the reflection and transmission processes at the various interfaces. That is, consider the incoming particle undergoing normal reflection and the resulting reflected particle; and the particles undergoing Andreev reflection or transmission. These

scattering methods are described in section 2.2. Categorize the particles based on their particle type (quasi- electron or hole), their travel direction (identified by an angle), and of course their host material.

4. For each identified particle in step 3 pick the right dispersion branch corresponding to the categorization in step 2. Then based on this dispersion branch, use the corresponding eigensolution derived in step 1 to form the complex normalized wavefunctions  $\phi_j^m(x, y) \sim A_j^m \phi_j^m e^{i\mathbf{k}\cdot\mathbf{r}}$ . Here,  $j$  indicates the correct energy branch. That is we assign each particle the appropriate wavefunction solution derived in section 3.2.
5. At each interface we impose the proper boundary conditions for the particles identified in step 3 undertaking some form of reflection or transmission using the appropriate wavefunctions found in step 4. We impose the wave functions to be square integrable <sup>13</sup>, i.e.

$$\int |\phi(x)|^2 dx < \infty, \quad (4.1)$$

for arbitrary integration limits. The plane-wave solutions to the BdG equations are assumed continuous in a homogeneous material. We impose the continuity of the wavefunction at the interfaces. Suppose we have an interface at  $x = x_0$  between an TI and MTI. We consider the electrons (solid lines) at the left interface in figure 21 and normalize by the norm of the incoming electron. The electron wavefunction is then given by

$$\phi(x, y) = \begin{cases} t\phi_e^{MTI,+}(\pi - \theta, x, y) & \text{for } x < x_0, \\ \phi_{e,+}^{TI}(\pi - \theta, x, y) + r\phi_{e,+}^{TI}(\theta, x, y) & \text{for } x > x_0, \end{cases} \quad (4.2)$$

left and right of the interface. The continuity of  $\phi$  at the interface imposes

$$\lim_{x \rightarrow x_0^-} t\phi_e^{MTI,+}(\pi - \theta, x, y) = \lim_{x \rightarrow x_0^+} (\phi_{e,+}^{TI}(\pi - \theta, x, y) + r\phi_{e,+}^{TI}(\theta, x, y)). \quad (4.3)$$

By imposing the continuity in this for all interfaces in the system, way we get a set of equations for the unknown complex coefficients like the

---

<sup>13</sup>Since  $|\phi(x_0)|^2$  is the probability of finding the particle at location  $x_0$ , the interpretation of this condition is simply that the probability of finding the particle within these integration limit cannot change abruptly. Physically speaking this condition is the mathematical statement that the wavefunction describing a physical state does not change abruptly, i.e. it describes a state that can be prepared with finite energy in finite time [46].

transmission  $t$  and the reflection  $r$ . In the coming work we will drop the limit notation and the  $(x, y)$  labels and simply equate the material specific BdG wavefunctions at the interfaces. Concretely we will write

$$t\phi_e^{MTI,+}(\pi - \theta) = \phi_{e,+}^{TI}(\pi - \theta) + r\phi_{e,+}^{TI}(\theta), \quad (4.4)$$

evaluated at  $x = x_0$ . The fact that we would form the wavefunction piece-wise such as in (4.2) and impose continuity through (4.3) is then implied, and valid by the continuity of the plane-wave eigensolutions to BdG equations in each homogeneous material.

We only require the continuity of the  $\phi$  itself rather than the 'usual' additional continuity of the derivative of  $\phi$ . This is because the BdG equations contain a single differential operator in (3.9) and are thus first order in space, whereas the Schrödinger equation is second order.

6. The equations in step 5 arising from the continuity of  $\phi$  (4.3) at each interface are then combined and written in a matrix vector form. Each spinor has a complex amplitude and is, in principle, of dimension four. The equation resulting from imposing continuity of the wavefunction at the interfaces provide sufficiently many equations (accounting for each component in the four dimensional spinors) for the unknown complex wavefunction amplitudes to be determined. We cast the equations into a linear system  $M\mathbf{c} = \mathbf{b}$  where  $\mathbf{c}$  is a vector containing all complex amplitudes,  $M$  contains the  $\phi$ 's row-wise, and  $\mathbf{b}$  contains the incoming particle's wavefunction.
7. The resulting linear system is then solved algebraically for the complex wavefunction amplitudes stored in  $\mathbf{c} = (A_1^m, A_2^m, \dots, A_1^k, \dots)^T$ . We considered the plane-wave modes for a single fixed energy  $E$ . So, the complex coefficients computed here are also for a fixed energy.

The resulting wave amplitudes (or reflection coefficients) are then used for further study of the system in a post-processing phase. To make the explicit connection from the complex amplitudes to reflection and transmission coefficients we point to (4.3). Here the complex amplitudes  $r, t$  are interpreted as the complex pre-factors an incoming electron with energy  $E$  relative to  $E_f$  with norm 1 obtains after either normal reflection  $r$  and transmission  $t$ . The reflection probability' is then  $|r|^2$ . Again these coefficients are for a fixed energy. So, say we have obtained  $t(E)$ , then the electron transmission

probability current one might observe experimentally when applying a voltage of  $eV$  would be proportional to  $\int_0^{eV} t(E)t^*(E)dE$ . To improve one might include a density of states in the integral, c.q. [3].

The steps are summarized in the algorithm flowchart shown in figure 22. At various locations in the diagram, relevant sections in the main text are referenced to indicate a derivation or further explanation of that step or result.

## 4.2 Tool motivation & assumptions

The motivation and assumptions underlying the tool should all be considered in light of this thesis's physical background, i.e. studying the behaviour of charge carriers in a system of various junctions between superconducting and magnetic materials on top of a 3D topological insulator. We now first state the motivation for the tool before addressing its underlying assumptions and corresponding limitations.

In principle each of the computations and steps described in the flowchart (see figure 22) can be done algebraically by hand. Hence we would arrive at an algebraic expression for e.g. the reflection coefficient for an incoming electron in a MTI-TI-STI system. The individual steps are simple. However, as the system's size grows, the amount of manipulations quickly becomes infeasible without suitable computational support. In fact, executing these steps by hand becomes an increasingly lengthy task prone to error. Moreover, the effect of a small correction or change somewhere at the start of the calculations is difficult to keep track off. Consequently the subset of problems we can study (algebraically) is limited by their size and complexity as this is bound by the time and accuracy with which one can execute these steps by hand. To remedy this, a tool was made to automate the indicated steps. Initially we build and use the tool to model MTI-TI-STI systems, but already when we consider STI-TI-MTI-TI-STI Josephson junction, as shown in figure 3, computations by hand were no-longer possible. The reason for our interest in the behaviour of such larger systems is evident in light of the the (chiral) Majorana modes it is predicted to host [1][31].

The limitations of the tool arise from (i) the type of systems we aim to solve, (ii) the assumption set by using the BdG equations, and (iii) are linked to the way we piece together the wavefunctions at each interface. The type of problems we aim to solve dictate a 2D domain with vertical boundaries spaced in the  $x$ -direction. Also, the system is assumed to extend much more

in the  $y$ -direction than the  $x$ -direction, such that we may ignore boundary effects in the  $y$ -direction. The tool was constructed with the application to topological insulators in mind, hence no impurity scattering effects are considered, this limits this approach to the clean limit (ballistic). The usage of the BdG equations gives rise to the corresponding assumptions as mentioned in chapter 3, i.e. sufficiently low temperature.

Final, the assumption that we require the continuity of the wavefunction at each interface might not capture all subtle physics occurring at the interface. For instance, the proximity effect in the  $x$ -direction between two neighbouring materials yields that the superconducting gap  $\Delta(x)$  is not strictly a step function. Nevertheless, this approach proves successful in predicting the most prominent effects. This method was pioneered by Blonder Tinker and Klapwijk (BTK) [3] already in 1982. The validity of this assumption is based on the fact that the BTK method is still widespread in the study of superconductivity ever since, for instance see the recent paper [93].

### 4.3 How to use the tool

The numbered steps illustrated in the algorithm flow diagram in figure 22 can broadly be categorized in three groups, i.e. elementary computation, categorization, and construction steps. After identifying each group, we discuss the way these steps are (partially) automated. In steps 1 and 7 we solve an eigenvalue problem and a linear system respectively. These steps can be considered as elementary computations. Depending on the size of the problem and the complexity of the matrices used, the computations can be difficult and lengthy, but a (symbolic) solver is suitable to do these tasks. Steps 2, 3 and 5 can be considered as categorization steps, here the solution branches, particles and wavefunctions on either side of an interface in the system are ordered. This categorization of the wavefunctions is based on the categorization of the solution branches discussed in section 3.2.4. When the particles, corresponding eigensolutions, and continuity requirements are well categorized, we automate the process of building the mathematical objects (wavefunctions or matrices) in the steps 4 and 6. We consider these steps as construction steps.

The group of elementary computational steps is most trivially automated by a symbolic solver<sup>14</sup>. The eigensolutions to the input Hamiltonians in ma-

---

<sup>14</sup>In this thesis the computer algebra system SymPy[94] is used.

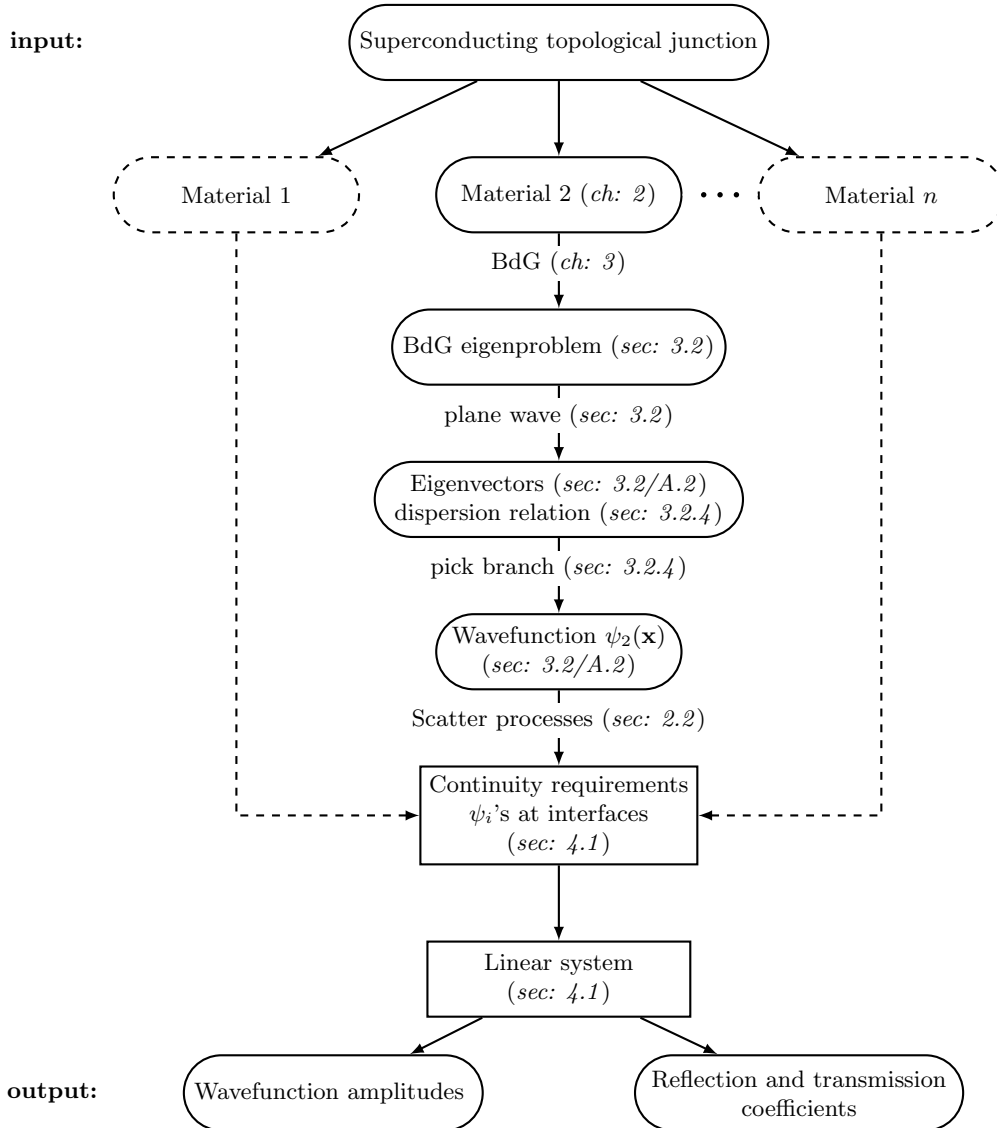


Figure 22: A schematic representing the working of the tool. At each step and block in the schematic a reference is placed to the corresponding section in the thesis where this step or block is discussed. The dashed columns left and right indicate that the steps shown in the middle column are also done in other columns. The input is a superconducting topological junction consisting of  $n$  bordering domains in which we each have a specific (quantum) material. In each domain, the material specific Bogoliubov-de Gennes equations are solved in a plane wave basis. From the multiple eigenvector solutions to the eigenproblem form of the BdG equations the appropriate energy solution branches are picked together with their corresponding wavefunctions. At each interface the various scattering processes that can occur are modelled, and then based on the continuity of the wavefunctions a scattering matrix is build. The scattering matrix is solved for the (complex) wavefunction amplitudes. These can be considered as reflection and transmission coefficients.

trix from, such as the ones shown in section 3.2, are readily found. To ease the interpretation of the resulting normalized eigenvectors, they are further simplified by substituting the symbol  $E$  into the eigenvector in places where the expression found for  $E$  (the eigenvalue) was encountered in the eigenvector. These type of simplifications are difficult to automate fully so they require some form of interaction between the user and the tool if the tool is to be extended beyond the currently implemented materials. There is always a limit to what we can (make the computer) do algebraically. When the number of unknown complex amplitudes grows beyond an order of  $\sim 10$ , closed form algebraic expressions for the amplitudes are no longer comprehensible and we can then simply evaluate them numerically and plot the result.

The categorization and building steps mentioned above are automated but do require some physical understanding of the problem at hand. In particular, given a completely new type of material and/or different junction, the tool does not simply compute the reflection coefficient automatically. The user is expected to implement new forms of reflection or transmission accordingly, and use the tool as a framework to automate all of the subsequent work.

## 4.4 Validation

The proposed automation might sound promising in reducing the risk of computational errors whilst decreasing the temporal burden of all these manual steps, but it all stands or falls by the validity of its output. To study the validity of the tool we compare known results from literature to various (intermediate) output. In this section we will compare known wavefunction eigensolutions to the tool's output. Similarly we will show that using the tool we re-obtain reflection coefficients known from literature for specific systems. Finally, we will look forward to some results in this thesis which highlight that using the tool enables to re-calculate various well-established findings in literature. This increases the confidence in the results without actually proving correctness.

### 4.4.1 Equivalent wavefunctions in literature

The BdG equations derived in this work (section 3.1) combine topological insulators with superconducting or magnetic materials. As an intermediate check, we compare the wavefunctions derived using the tool in section 3.2 to the theoretical work by Jian-Xin Zhu [47]. We show in appendix B that the

TI, MTI, STI spinors are equivalent up to a spin rotation to the ones derived by Zhu. The spin orientation is set by the way we couple the spin to the momentum, i.e. the form of  $\boldsymbol{\sigma}$  in the  $\mathbf{p} \cdot \boldsymbol{\sigma}$  term in (3.3) [69]. We work in a spin basis consisting of eigenstates of the Pauli spin matrix  $\sigma_x$ . This choice is somewhat arbitrary, because we can equivalently work in an eigenspace of  $\sigma_y$  or in that of the actual intrinsic spin of the system [68]. The explicit equivalence between the spinors in basis 1 given in section 3.2 to those in [47] is established in appendix B. This equivalence serves as a validation of the correctness of the tool's ability to derive the algebraic eigensolutions to the BdG equations.

#### 4.4.2 Manual reflection coefficient computation

The steps automated by the tool can in some selected cases be done by hand to check tool's results manually. This of course defeats the purpose of the tool, but it serves as a mean for further validation of the tool. To illustrate this, we consider the tunneling through a topological barrier in a TI-TI'-TI system (figure 23). Here the prime for the middle TI indicates a Fermi surface mismatch relative to its neighbours. That is, there is a non-matching chemical potential at both interfaces, resulting in an incomplete overlap of the Fermi surfaces in  $k$ -space on either side of the barrier. This gives rise to an imperfect conduction and hence we get an effective barrier. The mismatch is modelled by a different spatial angle, i.e., we introduce an angle  $\theta' \neq \theta$  describing the angle between the  $x$  and  $y$  component of the momentum in the middle region. In literature this system is already derived by hand [46].

We first derive the required electron TI wavefunction manually. We consider the single particle Hamiltonian

$$\hat{h}_{TI} = v_f \mathbf{p} \cdot \boldsymbol{\sigma} - \mu = \begin{pmatrix} -\mu & -i\hbar v_f(\partial/\partial x - i\partial/\partial y) \\ -i\hbar v_f(\partial/\partial x + i\partial/\partial y) & -\mu \end{pmatrix}, \quad (4.5)$$

and a wavefunction of the form

$$\phi(x, y) = \begin{pmatrix} u_{0\uparrow} \\ u_{0\downarrow} \end{pmatrix} e^{ik_x x + ik_y y}, \quad (4.6)$$

to arrive at eigenproblem (3.26)

$$\begin{pmatrix} -\mu & \hbar k_e v_f e^{-i\theta} \\ \hbar k_e v_f e^{i\theta} & -\mu \end{pmatrix} \begin{pmatrix} u_{0\uparrow} \\ u_{0\downarrow} \end{pmatrix} = E \begin{pmatrix} u_{0\uparrow} \\ u_{0\downarrow} \end{pmatrix}, \quad (4.7)$$

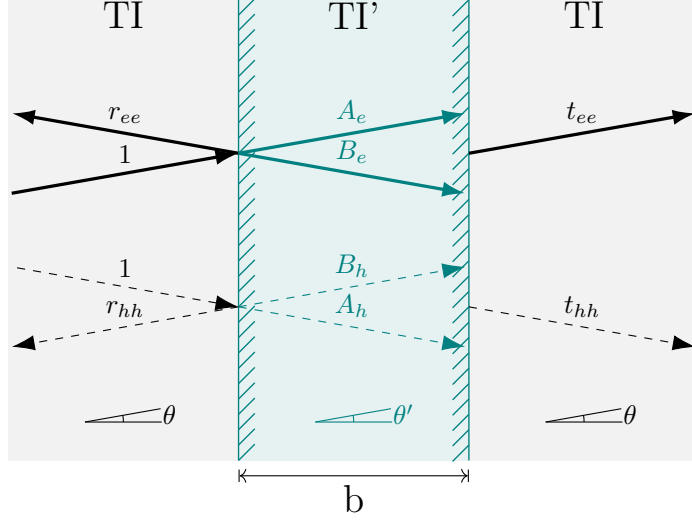


Figure 23: A schematic illustration of an incoming electron (hole) from a TI traveling under an angle  $\theta$  ( $-\theta$ ) undergoing normal reflection  $r_{ee}$  ( $r_{hh}$ ) or transmission  $t_{ee}$  ( $t_{hh}$ ) for a double barrier system consisting for three TI's. The middle TI is held at a different chemical potential, giving rise to a Fermi surface mismatch relative to the other two TI's. The Fermi surface mismatch could result in a nonzero transparency ( $D := 1 - rr^*$ ). The middle TI is  $b$  wide.

with eigenvalues

$$(E + \mu)^2 = (\hbar v_f k_e)^2 \rightarrow E_{\pm} = \pm \hbar v_f k_e - \mu.$$

This result reflects the known linear dispersion of a topological insulator. For  $E_+$  we rewrite (4.7), using the definition of  $k_e$ , to

$$\begin{pmatrix} -1 & e^{-i\theta} \\ e^{i\theta} & -1 \end{pmatrix} \begin{pmatrix} u_{0\uparrow} \\ u_{0\downarrow} \end{pmatrix} = \mathbf{0} \rightarrow \frac{u_{0\uparrow}}{u_{0\downarrow}} = e^{i\theta} \\ \rightarrow \phi_{e+}^{TI}(\theta) = \frac{1}{\sqrt{2}} \begin{pmatrix} 1 \\ e^{i\theta} \end{pmatrix} e^{ik_x x + ik_y y}.$$

The negative  $k_e$ -branch would give  $\frac{1}{\sqrt{2}}(1, -e^{i\theta})^T$ .

Now we consider the middle TI-TI'-TI subsystem illustrated in figure 23. An initial electron from the left TI is inbound on the middle TI' under an angle of  $\theta$ . By imposing continuity of the spinors at each interface (we take the first interface at  $x = 0$  and hence the second at  $x = b$ ), we can build a system corresponding to these two requirements. We get the following two

continuity requirements

$$\begin{aligned} \phi_{e+}^{TI}(\theta) + r_{ee}\phi_{e+}^{TI}(\pi - \theta) &= A_e\phi_{e+}^{TI}(\theta') + B_e\phi_{e+}^{TI}(\pi - \theta'), & \text{at } (x, y) = (0, 0), \\ A_e\phi_{e+}^{TI}(\theta') + B_e\phi_{e+}^{TI}(\pi - \theta') &= t_{ee}\phi_{e+}^{TI}(\theta), & \text{at } (x, y) = (b, 0). \end{aligned}$$

The first equation describes the imposed continuity of an electron incoming from the left TI under an angle  $\theta$  undergoing either normal reflection  $r_{ee}$  or transmission  $A_e$ . The second ( $B_e$ ) term is required here to describe an electron resulting from the normal reflection at the second interface traveling towards the first interface again. At the second interface the transmitted electron  $A_e$  in the middle TI' can either reflect normally  $B_e$  or transmit,  $t_{ee}$ , to the right TI.

The imposed continuity gives us  $2 \times 2$  equations describing the four unknowns  $r_{ee}$ ,  $A_e$ ,  $B_e$ , and  $t_{ee}$ . By eliminating  $A_e$  and  $B_e$  we can solve this system for, in particular,  $r_{ee}$ . These (trivial) elimination steps are omitted, but they result in [46]:

$$r_{ee}(\theta) = \frac{2e^{i\theta} \sin(k_{xe}b) (\sin \theta - \sin \theta')}{e^{-ik_{xe}b} \cos(\theta + \theta') + e^{ik_{xe}b} \cos(\theta - \theta') - 2i \sin(k_{xe}b)}. \quad (4.8)$$

Using the tool we find exactly the same reflection coefficient (4.8). Moreover, this expression has been derived before for Klein tunneling in graphene [62] and in Dirac semimetals [95]. Anyone who has solved such a scattering problem knows the patience and focus required to avoid small computational errors, but we have shown that the tool quickly and correctly computes results such as (4.8). By comparing not only the final reflection coefficient, but also the to-be solved linear system to the work [46], this example illustrates the validity of the tool in all its steps, from finding the wavefunctions, to piecing them together correctly and then deriving the (correct) reflection coefficient.

Now that we have some confidence in the validity of the tool, we can use it to compute reflection and transmission coefficients and post-process them to (re)derive various results. We briefly mention here a few results that were re-derived using the tool before we look at some novel results. In the coming results chapter 5 we employ the tool to compute a result on the occurrence of chiral Majorana modes in the form of Andreev bound states in an MTI-TI-STI system by Tanaka [38]. Additionally, the angle dependent transmission coefficient for a TI-MTI-TI tunnel barrier system is computed for which the 1D limit agrees with literature [41]. Moreover, a novel mechanism to invert the chirality of Majorana modes in a MTI-TI-STI

system is proposed and studied. Finally, the re-derived result by Tanaka is combined with the two dimensional transmission coefficient to study the multiple Andreev reflections in a symmetric STI-TI-MTI-TI-STI Josephson junction. Since the last results are novel, they can not be checked against literature to validate the working of the tool. We can however investigate the implication of the tool's output and check whether the results make physical sense, e.g., under specific asymptotic conditions.

## 5 Results

The reason to automate the computations using the tool described in chapter 4 was to correctly and efficiently compute the reflection and transmission of (electronic) wavefunctions in a system consisting of multiple interfaces between quantum materials of varying kinds. In this chapter, we focus on the topological Josephson junction consisting of two superconducting leads inducing s-wave superconductivity into the 2D topological surface states in a 2D topological insulator. The two superconducting leads are connected by a (magnetic) constriction acting as a tunnel barrier. The resulting STI-TI-MTI-TI-STI system is depicted in figure 3. We will analyse the quantum transport through the system as a whole, in parts, and its constituent bilayers using the tool. In doing so we re-derive results from literature as limiting cases of the full 2D system that has never been analysed in full detail before.

First we consider the isolated MTI-TI-STI subsystem, top view shown in figure 20 and 21, obtained by removing the left STI from the Josephson junction in figure 3. For this system we re-derive a result by Tanaka [38] in section 5.1. This section can be considered as further validation of the tool. The coefficients  $r_{ee}^{MTI}$  etc in figure 21 are indicated to show all possible wavefunctions in the system. The solid and dashed lines indicate electron- and hole-like quasiparticles. The second TI hosts an Andreev bound state, and as the width,  $d \rightarrow 0$ , this system describes an interface between an MTI and STI in which, as predicted by Fu and Kane[1], zero-energy Majorana bound states in the form of chiral Majoranas can appear.

The conditions are derived under which this chiral Majorana mode (CMM) emerge in the form of an ABS, as well as the corresponding energy. Concretely, a phase coherence condition is formulated (section 5.1.4) to predict the existence of a possible zero-energy structure in the density of states. Recall that (zero) energy here, is relative to the  $E_f$ . Moreover, using the results on the CMM we can predict the shift away from zero energy of this structure as a function of the incidence angle  $\theta$  and magnetic energy gap  $m_z$ . After this in section 5.2, a novel way is demonstrated to manipulate the direction of motion of the CMM in the system.

After studying the CMM in the form of Andreev bound states in an MTI-TI-STI system, we use the tool to study the multiple Andreev reflections in the full topological Josephson junction shown in figure 3. In the figure, a magnetic tunnel barrier is drawn, but in section 5.3 we consider a ferromag-

netic insulating or Fermi surface mismatch tunnel barrier. First, we compute the reflection at- and transmission through both barriers. Based on these calculations and the phase coherence criterion derived in section 5.1.4 we can predict the existence of certain resonance features in the current that arises from the found Andreev bound states in the (two) isolated subsystems. Since the full Josephson junction in figure 3 can be formed by connecting the two (STI-TI-MTI and MTI-TI-STI) sub-systems by a tunnel barrier, the bound states<sup>15</sup> on either side can open novel conduction channels that would be visible in a measured or simulated  $I, V$  curve.

Next, we compute the DC current through the entire Josephson junction by solving the so-called recurrence relations. Here we extend the work of Olde Olthof[46] on what the effect is of the tunnel barrier's type (magnetic or a Fermi surface mismatch barrier) on the DC current as a function of the applied voltage bias (i.e. the simulated  $I, V$  curves). We relate the results derived for the CMM in the form of ABS in the MTI-TI-STI system studied in section 5.1 to the simulated MAR  $I, V$  curves as shown in section 5.3. Concretely, the voltages for which the peaks occur in the MAR's  $I, V$  curves can be fitted by the predicted locations based on the phase coherence predictions in section 5.1.4. That is, the energies at which a CMM is predicted to exist are related to the voltages at which steps and peaks occur in the simulated  $I, V$  MAR spectra.

## 5.1 Chiral Majorana modes as Andreev bound states

Following Fu and Kane [1], Tanaka [38] modelled the MTI-TI-STI system shown in figure 20 and 21, and showed the emergence of chiral Majorana modes as Andreev bound states occurring in this system. The goal of this section here is to re-derive the ABS's dependency on the incoming particle's energy and angle, and the magnetic energy gap's size. We study this by considering the phase gain associated with the types of reflection possible per particle at each interface in figure 21. An ABS occurs when the wavefunctions responsible for the bound state add up constructively after successive (Andreev) reflections, i.e. the phase gains obey (2.6). If we have all relevant phases, we can transform the phase condition to a relation between the incoming particle's energy and angle for a fixed  $m_z$ . Meaning that for a specified magnetic energy gap and incoming angle, we can predict the energy

---

<sup>15</sup>When the two systems hosting bound states are connected by a tunnel barrier the bound states are no-longer isolated and become delocalized, so in principle, the current predictions based on these bound states are valid only in the strong barrier (low transmission) limit.

at which a CMM in the form of an ABS is likely to occur based on the phase coherence criterion. We not only re-derive the results by Tanaka, but we also study the transmission through the system and demonstrate a novel way to manipulate the CMM.

The MTI-TI-STI system can be broken down into two distinct bilayers, an MTI-TI, and a TI-STI one. In the coming two subsections we will compute the relevant reflection coefficients for each bilayer for an incoming electron and hole. That is, we need to solve four distinct but similarly structured scattering problems. The tool described in chapter 4 is well equipped to swiftly and systematically solve these four problems. To model the bilayers such that pieced together they form the full MTI-TI-STI system we should be careful in using the appropriate angle under which the charge carriers are inbound on the interfaces. The angles need to be such that together they model the full systems that allow an ABS. We therefore, consider a TI-STI interface with an electron inbound under an angle that we define as  $\theta$ . The holes should then be inbound with angle  $-\theta$ . For the MTI-TI interface, the angles should be  $\pi - \theta$  and  $\pi + \theta$  for the electron and hole respectively.

### 5.1.1 TI-STI bilayer

We now consider a TI-STI bilayer as shown in figure 24. An electron (hole) inbound under angle  $\theta$  ( $-\theta$ ) from the TI side undergoes a scattering event at the TI-STI interface. The four possible channels are, normal reflection,  $r_{ee}(r_{hh})$ ; Andreev reflection  $r_{eh}(r_{he})$  and corresponding transmission  $t_{ee}(t_{hh})$ ; or Branch crossing transmission  $t_{eh}(t_{he})$ . The calculations are all automated by the tool, here we still show intermediate results to illustrate the tool's working, but in later sections we shall omit these intermediate steps. The shown eigenfunctions in this section are given in section 3.2, and appendix A for basis 1 and 2 respectively. Details on further labeling of the spinors can also be found there.

We set up a system of equations based on the continuity of the spinors at the interface, which is taken at  $x = 0$ , and solve this system for the reflection and transmission coefficients. For an electron under angle  $\theta$  from the TI's side traveling towards the STI we have the following continuity requirement

$$\phi_{e+}^{TI,(i)}(\theta) + r_{ee}^{(i)} \phi_{e+}^{TI,(i)}(\pi - \theta) + r_{eh}^{(i)} \phi_{h-}^{TI,(i)}(\pi + \theta) = t_{ee}^{(i)} \phi_{+}^{STI,-(i)}(\theta_s) + t_{eh}^{(i)} \phi_{-}^{STI,-(i)}(-\theta_s). \quad (5.1)$$

The label  $(i)$  refers to the basis we use. The equation describes an incoming

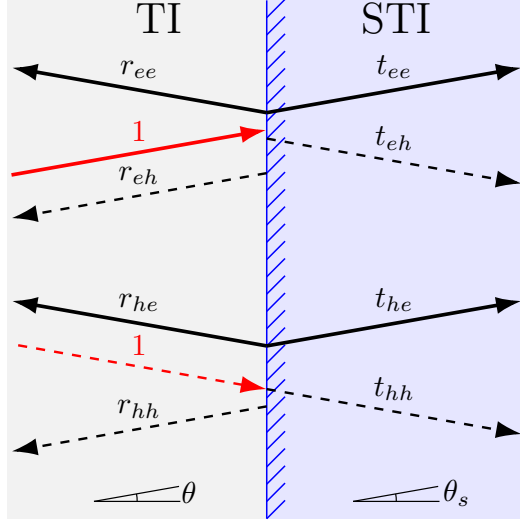


Figure 24: A schematic illustration of an incoming electron (hole) from a TI traveling under an angle  $\theta$  ( $-\theta$ ) undergoing normal reflection  $r_{ee}$  ( $r_{hh}$ ), Andreev reflection  $r_{eh}$  ( $r_{he}$ ), transmission  $t_{ee}$  ( $t_{ee}$ ), or branch crossed transmission  $t_{eh}$  ( $t_{he}$ ) for a TI-STI bilayer. We consider the possibility of a Fermi surface mismatch between the TI and STI by introducing a different angle  $\theta_s$  in the STI.

electron in the TI traveling under an angle  $\theta$  undergoing either normal reflection  $r_{ee}^{(i)}$  or Andreev reflection  $r_{eh}^{(i)}$  and remaining in the TI or transmitting into the STI as either an electron-like ( $t_{ee}^{(i)}$ ) or hole-like ( $t_{eh}^{(i)}$ ) quasiparticle. For a hole traveling with an angle  $-\theta$  we arrive at an analogous equation

$$\phi_{h-}^{TI,(i)}(-\theta) + r_{hh}^{(i)} \phi_{h-}^{TI,(i)}(\pi+\theta) + r_{he}^{(i)} \phi_{e+}^{TI,(i)}(\pi-\theta) = t_{hh}^{(i)} \phi_{-}^{STI,-(i)}(-\theta_s) + t_{he}^{(i)} \phi_{+}^{STI,-(i)}(\theta_s). \quad (5.2)$$

Per incoming particle type and basis, we can cast this continuity requirement into a system of equations. The four unknown quantities are the reflection and transmission coefficients. This single equation is actually a vector equation consisting of four equations element-wise, i.e. we have four equations for four unknowns.

### Basis 1

For an electron under angle  $\theta$  inbound on the TI-STI interface, we find the following system

$$\begin{bmatrix} \frac{1}{\sqrt{2}} & 0 & -\frac{1}{2} & -\frac{1}{2} \\ \frac{-e^{-i\theta}}{\sqrt{2}} & 0 & -\frac{e^{i\theta_s}}{2} & \frac{e^{-i\theta_s}}{2} \\ 0 & \frac{1}{\sqrt{2}} & -\frac{\chi - e^{i\theta_s} e^{-i\varphi}}{2\Delta_0} & \frac{\chi + e^{-i\theta_s} e^{-i\varphi}}{2\Delta_0} \\ 0 & \frac{e^{-i\theta}}{\sqrt{2}} & -\frac{\chi - e^{-i\varphi}}{2\Delta_0} & -\frac{\chi + e^{-i\varphi}}{2\Delta_0} \end{bmatrix} \begin{bmatrix} r_{ee}^{(1)} \\ r_{eh}^{(1)} \\ t_{ee}^{(1)} \\ t_{eh}^{(1)} \end{bmatrix} = \begin{bmatrix} \frac{1}{\sqrt{2}} \\ \frac{e^{i\theta}}{\sqrt{2}} \\ 0 \\ 0 \end{bmatrix}. \quad (5.3)$$

We solve the four by four linear system for the electron-hole Andreev reflection coefficient in basis 1

$$r_{eh}^{(1)} = \frac{\chi_-}{\Delta_0} e^{i\theta} e^{-i\varphi} g(\theta, \theta_s), \quad (5.4)$$

where we define

$$g(\theta, \theta_s) = \frac{\cos(\theta_s - \theta) + \cos(\theta_s + \theta)}{\frac{\chi_-}{\chi_+} \cos(\theta_s - \theta) + \cos(\theta_s + \theta) + (1 - \frac{\chi_-}{\chi_+})}. \quad (5.5)$$

This function will pop up in all Andreev reflection coefficients, so that is why we explicitly mention it here. Moreover in the limit  $\mu = \mu_s \rightarrow \theta = \theta_s$  where there is no Fermi surface mismatch between the TI and STI we have

$$\lim_{\theta \rightarrow \theta_s} g(\theta, \theta_s) = 1. \quad (5.6)$$

To be precise, this limit also holds for all  $\mu$  when  $\theta = 0 \rightarrow \theta_s = 0$ . The quantities  $\chi_{\pm}$  are defined in (3.44), and they essentially describe the relationship between the incoming particle's energy and the superconducting energy gap. In the sub-gap range, i.e.  $|E| < |\Delta_0|$ , the  $\chi$ 's are complex.

For a hole incoming under an angle  $-\theta$  we find

$$\begin{bmatrix} 0 & \frac{1}{\sqrt{2}} & -\frac{1}{2} & -\frac{1}{2} \\ 0 & \frac{-e^{-i\theta}}{\sqrt{2}} & \frac{e^{-i\theta_s}}{2} & -\frac{e^{i\theta_s}}{2} \\ \frac{1}{\sqrt{2}} & 0 & \frac{\chi_+ e^{-i\theta_s} e^{-i\varphi}}{2\Delta_0} & -\frac{\chi_- e^{i\theta_s} e^{-i\varphi}}{2\Delta_0} \\ \frac{e^{-i\theta}}{\sqrt{2}} & 0 & -\frac{\chi_+ e^{-i\varphi}}{2\Delta_0} & -\frac{\chi_- e^{-i\varphi}}{2\Delta_0} \end{bmatrix} \begin{bmatrix} r_{hh}^{(1)} \\ r_{he}^{(1)} \\ t_{hh}^{(1)} \\ t_{he}^{(1)} \end{bmatrix} = \begin{bmatrix} 0 \\ 0 \\ \frac{1}{\sqrt{2}} \\ -\frac{e^{i\theta}}{\sqrt{2}} \end{bmatrix}, \quad (5.7)$$

with a corresponding hole-electron Andreev reflection coefficient

$$r_{he}^{(1)} = -\frac{\chi_-}{\Delta_0} e^{i\theta} e^{i\varphi} g(\theta, \theta_s). \quad (5.8)$$

So, we see that in basis 1 the following relation holds

$$r_{eh}^{(1)} = -r_{he}^{(1)} e^{-2i\varphi}. \quad (5.9)$$

## Basis 2

A completely analogous computation in basis 2 yields the following two Andreev reflection coefficients, for an electron incoming under angle  $\theta$

$$r_{eh}^{(2)} = \frac{\chi_-}{\Delta_0} e^{-i\varphi} g(\theta, \theta_s), \quad (5.10)$$

and for an incoming hole under  $-\theta$

$$r_{he}^{(2)} = \frac{\chi_-}{\Delta_0} e^{i\varphi} g(\theta, \theta_s). \quad (5.11)$$

So we actually see that in basis 2 the two Andreev reflection coefficients become equal up to a phase difference of  $2\varphi$

$$\boxed{r_{eh}^{(2)} = r_{he}^{(2)} e^{-2i\varphi}.} \quad (5.12)$$

Moreover, if we use the approximation,  $\mu = \mu_s \rightarrow \theta = \theta_s$ , we have  $g(\theta, \theta_s) = 1$  and the angle dependency drops out. Consequently in basis 2, the Andreev reflection coefficient are angle independent and equal for electrons and holes when  $\varphi = n\pi, n \in \mathbb{N}$ . This result further highlights the benefit of using basis 2, because if we want to do further calculations in systems with multiple superconducting interfaces, then we can simply use a single Andreev coefficient for all possible incident particles, when the superconducting phase is set to a multiple of  $\pi$ . This result will be useful in the study of multiple Andreev reflections 5.3. For the results to follow we will therefore adopt basis 2. We can thus define a single Andreev reflection coefficient in basis 2 (up to a superconducting phase  $\varphi$ )

$$\boxed{r_{AR}^{(2)} = \frac{E - \sqrt{E^2 - \Delta_0^2}}{\Delta_0} \rightarrow e^{-i \arccos(E/\Delta_0)} \quad \text{when} \quad -\Delta_0 < E < \Delta_0.} \quad (5.13)$$

The fact that something with a clear physical interpretation such as the reflection coefficients are shown to be different in a different basis might sound as if the physics has become basis dependent. However, it should be noted that one can not observe (read measure) a complex reflection coefficient. When studying for example a TI-STI bi-layer experimentally, one would look at for instance the current through the bi-layer. The current for one scales with the transparency,  $D$ , of the barrier. However,  $D$  is a real quantity given by  $D := 1 - rr^*$ , so if the reflection coefficient only differs by a complex phase between two bases, the resulting physical observable ( $D$ ) remains unchanged. Indeed, the reflection coefficients only differ by a complex phase between (5.4) and (5.10) and between (5.8) and (5.11).

### 5.1.2 MTI-TI bilayer

We now consider a MTI-TI bilayer as shown in figure 25. An electron (hole) inbound under angle  $\pi - \theta$  ( $\pi + \theta$ ) from the TI side undergoes a scattering

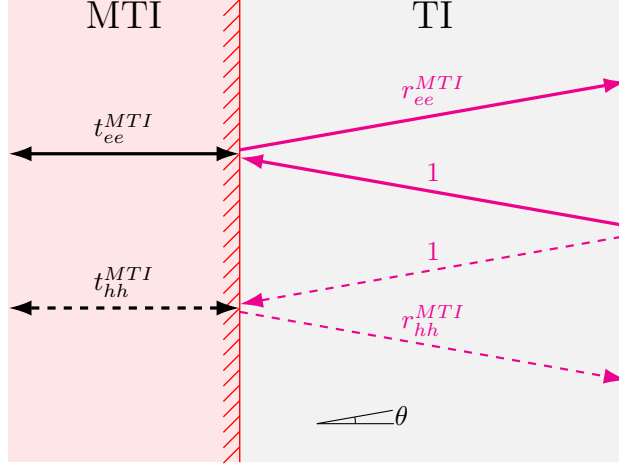


Figure 25: A schematic illustration of an incoming electron (hole) from a TI traveling under an angle  $\pi - \theta$  ( $\pi + \theta$ ) undergoing normal reflection  $r_{ee}^{MTI}$  ( $r_{hh}^{MTI}$ ) or transmission  $t_{ee}^{MTI}$  ( $t_{hh}^{MTI}$ ) for a MTI-TI bilayer.

event at the MTI-TI interface. The two possible channels are, normal reflection,  $r_{ee}^{MTI}$  ( $r_{hh}^{MTI}$ ); and the transmission into to the MTI  $t_{ee}^{MTI}$  ( $t_{hh}^{MTI}$ ) to a wavefunction that is decreasing in the negative  $x$ -direction. Similar to the previous section, we illustrate the tool's workings by showing intermediate steps. We show this case too because now there is a magnetic active material present. This introduces the usage of evanescent wavefunctions. To obey the physical requirement that the used wavefunctions remain normalisable on the given domain, we need to have that our MTI wavefunctions decrease to zero as  $x \rightarrow -\infty$ .

As before we set up a system of equations based on the continuity of the spinors at the interface, which is taken at zero, and solve this for the reflection and transmission coefficients. It should now be noted that due to the absence of superconductivity in this system, there is no coupling between electron-like and hole-like quasiparticles in the BdG matrix form of the Hamiltonian and consequently we can describe the system by spinors of dimension two. Hence the two continuity requirements both consist of two element-wise equations for two unknowns. Moreover, as seen in section 3.3, in absence of superconductivity, the wavefunctions for the electrons becomes the same for both bases. Hence we now need to solve three problems, one for an incoming electron, and two for an incoming hole (one per basis).

We consider an electron under angle  $\pi - \theta$  from the TI's side traveling

towards the MTI (in either basis)

$$\phi_{e+}^{TI,(i)}(\pi - \theta) + r_{ee}^{MTI,(i)} \phi_{e+}^{TI,(i)}(\theta) = t_{ee}^{MTI,(i)} \phi_e^{MTI,+,(i)}(\pi - \theta). \quad (5.14)$$

Again, the label  $(i)$  refers to the basis we use, and the spinors in basis 1 are given in sec 3.2, and for basis 2 we refer to the appendix A. For the incoming holes, we consider an initial hole traveling in the  $\pi + \theta$  direction. At  $(x, y) = (0, 0)$  we have

$$\phi_{h-}^{TI,(i)}(\pi + \theta) + r_{hh}^{MTI,(i)} \phi_{h-}^{TI,(i)}(-\theta) = t_{hh}^{MTI,(i)} \phi_h^{MTI,(i),+}(\pi + \theta). \quad (5.15)$$

The electron continuity requirement (5.14) gives rise to the follow system of equations

$$\begin{bmatrix} \frac{1}{\sqrt{2}} & \frac{ik_e v_f \sin(\theta) + \hbar q_e v_f}{\sqrt{A_{e-}}} \\ \frac{e^{-i\theta}}{\sqrt{2}} & \frac{-E + m_z - \mu_m}{\sqrt{A_{e-}}} \end{bmatrix} \begin{bmatrix} r_{ee}^{MTI} \\ t_{ee}^{MTI} \end{bmatrix} = \begin{bmatrix} -\frac{1}{\sqrt{2}} \\ \frac{e^{i\theta}}{\sqrt{2}} \end{bmatrix}, \quad (5.16)$$

We solve this system for the electron normal reflection coefficient

$$r_{ee}^{MTI}(\pi - \theta) = -\frac{E - m_z + \mu_m - (ik_e \sin(\theta) + q_e) \hbar v_f e^{-i\theta}}{E - m_z + \mu_m + (ik_e \sin(\theta) + q_e) \hbar v_f e^{i\theta}}. \quad (5.17)$$

### Basis 1

Next we consider the hole normal reflection coefficients in both bases. First a hole incoming under angle  $\pi + \theta$  in basis 1 gives rise to the follow system of equations

$$\begin{bmatrix} \frac{1}{\sqrt{2}} & -\frac{ik_h v_f \sin(\theta) + \hbar q_h v_f}{\sqrt{A_{h-}}} \\ \frac{e^{-i\theta}}{\sqrt{2}} & \frac{E + m_z - \mu_m}{\sqrt{A_{h-}}} \end{bmatrix} \begin{bmatrix} r_{hh}^{MTI,(1)} \\ t_{hh}^{MTI,(1)} \end{bmatrix} = \begin{bmatrix} \frac{1}{\sqrt{2}} \\ -\frac{e^{i\theta}}{\sqrt{2}} \end{bmatrix}, \quad (5.18)$$

which we solve for

$$r_{hh}^{MTI,(1)}(\pi + \theta) = -\frac{E + m_z - \mu_m + (ik_h \sin(\theta) - q_h) \hbar v_f e^{-i\theta}}{E + m_z - \mu_m - (ik_h \sin(\theta) - q_h) \hbar v_f e^{i\theta}}. \quad (5.19)$$

### Basis 2

We go through the analogous set of steps in basis 2. The resulting hole normal reflection coefficients is given by

$$r_{hh}^{MTI,(2)}(\pi + \theta) = -\frac{E - m_z - \mu_m - (ik_h \sin(\theta) + q_h) \hbar v_f e^{i\theta}}{E - m_z - \mu_m + (ik_h \sin(\theta) + q_h) \hbar v_f e^{-i\theta}}. \quad (5.20)$$

We compare the electron to the hole normal reflection coefficients because this relations will become important in the coming section when we study

multiple Andreev reflections, we however can not identify a simple relationship between the electron and hole normal reflection coefficients like we could for the TI-STI interface. We therefore will consider a physically logical limiting case. Namely, bound states occur in the overall MTI-TI-STI system when the MTI acts sufficiently well as a barrier. That is, the charge carriers moving in the the TI towards the MTI should be reflected much more than transmitted. The MTI's reflective behaviour is most pronounced when the magnetic field strength is large compared to the energy of the incoming particle ( $E$ ) and the chemical potential in the MTI  $\mu_m$ . So we now compare (5.17), (5.19), and (5.20) in the large  $m_z \gg E, \mu_m$  limit. In this limit,  $q_{e,h} \rightarrow im_z$ , i.e. the  $m_z$  and  $q_{e,h} \rightarrow im_z$  terms become dominant. We find

$$\begin{aligned} r_{ee}^{MTI}(\pi - \theta) &\rightarrow -ie^{-i\theta}, \\ r_{hh}^{MTI,(1)}(\pi + \theta) &\rightarrow ie^{-i\theta}, \\ r_{hh}^{MTI,(2)}(\pi + \theta) &\rightarrow -ie^{i\theta}. \end{aligned} \tag{5.21}$$

In this limit the reflection coefficients are related by

$$r_{hh}^{MTI,(1)}(\pi + \theta) = (r_{ee}^{MTI}(\pi - \theta))^* e^{-2i\theta}, \tag{5.22}$$

$$\boxed{r_{hh}^{MTI,(2)}(\pi + \theta) = - (r_{ee}^{MTI}(\pi - \theta))^*}. \tag{5.23}$$

### 5.1.3 Andreev bound state phase coherence condition

Now that we have computed all reflection coefficients that make up the Andreev bound state indicated in magenta in figure 21, we can compute their phases and study the ABS resonance criterion in (2.6). The procedure is as follows, for a fixed  $m_z$  we compute the sum of the phases,

$$\alpha_\Sigma = \alpha_{r_{eh}^{STI,(2)}} + \alpha_{r_{he}^{STI,(2)}} + \alpha_{r_{hh}^{MTI,(2)}} + \alpha_{r_{ee}^{MTI,(2)}},$$

for  $\theta \in (-\pi/2, \pi/2)$ . Then we solve for the  $E$  value such that  $\alpha_\Sigma$  crosses<sup>16</sup> a multiple of  $2\pi$ . This procedure traces a curve in  $(\theta, E)$ -space indicating the location of an Andreev bound state. Figure 26 shows this result for various values of  $m_z$  (relative to the chemical potential in the TI). The figure should be interpret as follows, for a given  $m_z$  and  $\theta$ , it shows the energy value for which a phase coherent Andreev bound state occurs.

---

<sup>16</sup>We find these 'zero' crossing up to some predefined tolerance.

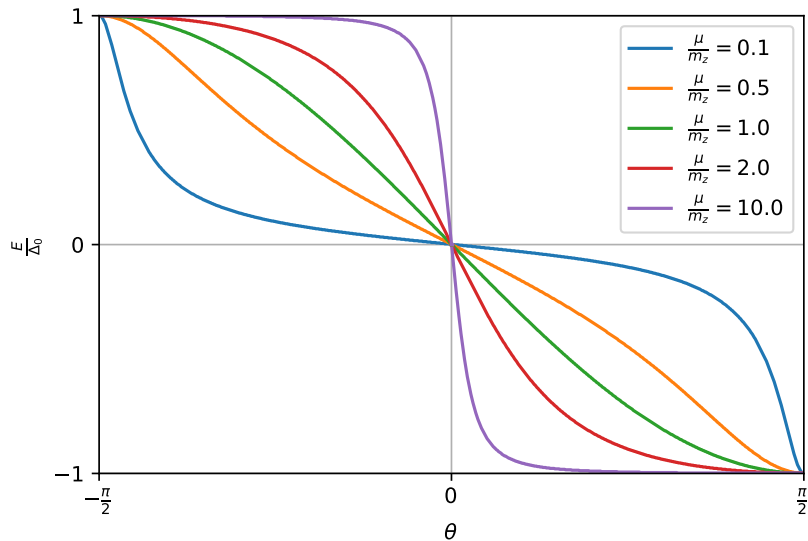


Figure 26: Chiral Majorana mode (CMM) bound state level  $E$  as a function of the incident angle  $\theta$ . Here,  $m_z = 800\Delta_0$ ,  $\mu_m = 0$ , and  $\mu = \mu_s$  is varied to get the ratios shown in the legend.

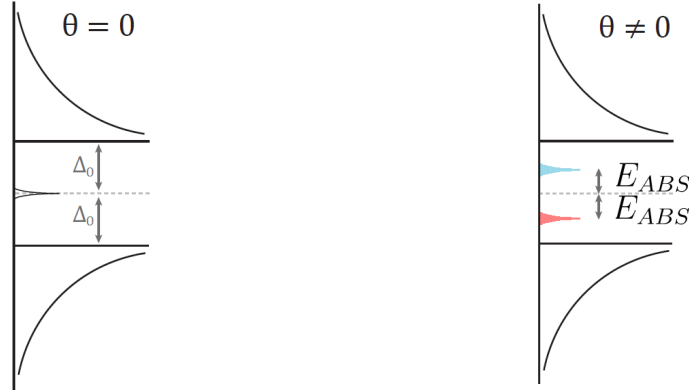
The notable characteristics of the curves in figure 26 can be described as a function of  $\theta$  and of  $m_z$ . For all  $m_z$ , the bound state occurs at zero energy in the 1D limit ( $\theta = 0$ ). For small finite angles, the bound state moves away from zero energy. As the angles increase in absolute value, to almost vertical incident angles, the bound state saturates to a value of  $E = \pm\Delta_0$ . For a fixed  $m_z$ , the angle-dependent behaviour can globally be explained by examining the normal and Andreev reflection coefficients. We showed that in basis 2, the Andreev reflection coefficients were given by (5.13) independent of the angle and particle type. They only vary with the energy for a fixed  $\Delta_0$ . The normal reflection coefficients are however angle-dependent, see (5.17) and (5.20).

To explain the angle dependency in detail we first look at the 1D limit for a sufficiently strong fixed  $m_z$ , and then we explain the angle-dependent effects. The normal reflections in basis 2 go to  $-i$ , this can be seen by taking  $\theta = 0$  in (5.21). The resulting normal reflection phases will thus be equal and sum to  $-\pi$ . A phase coherent ABS occurs when the normal and Andreev reflections give rise to a summed phase of an integer multiple of  $2\pi$ . This condition is met when the Andreev reflections contribute a phase of  $\pm\pi/2$  each. i.e. for  $E = 0$  in (5.13)  $r_{AR} \rightarrow -i$  and hence the electron and hole Andreev reflection together contribute the required  $-\pi$ . So in the 1D limit, there is an ABS at  $E = 0$ .

To meet the phase coherence criterion for the ABS for varying angles the alteration in the phase gain due to normal reflections has to be compensated by a phase gain change for the Andreev reflections. As the Andreev reflections only vary with energy, the bound state moves away from zero energy. The limiting behaviour  $E \rightarrow \pm\Delta_0$  for vertical incident angles can be explained similarly. For almost vertical incident angles ( $\theta \rightarrow \pm\pi/2$ ) the normal reflection coefficients, (5.21) become real, but the electron and hole phase gain cancel (because of the opposite sign in front of  $\theta$  in the exponent). This means that the Andreev reflection coefficient should give a combined contribution of an integer multiple of  $2\pi$ , which happens for  $r_{AR} \in \mathbb{R}$ . This condition is met only in the limit  $E \rightarrow \pm\Delta_0$ .

The angle dependency per drawn curve in figure 26 can be explained by the above, however, the effect of the strength of the magnetic barrier gives rise to the differences between the drawn curves. The larger  $m_z$ , the flatter the curves are around  $E = 0$ . i.e. by increasing  $m_z$  the ABS stay close to  $E = 0$  for a larger range of  $\theta$ . The results found and described here are identical to those found by Tanaka [38], the methods used to come to them are however different. Whereas we reasoned based on a phase coherence criterion, Tanaka derives the bound states' location in  $(\theta, E)$ -space from poles in the (angle-dependent) tunnelling conductance.

The difference between the curves as a function of the ratio  $\mu/m_z$  is best characterised by the observation that for a strong magnetic barrier,  $\mu/m_z \ll 1$ , the bound states at  $E = 0$  are robust against angle-dependent effects, whereas for a weak magnetic barrier,  $\mu/m_z \gg 1$ , the bound states depart from  $E = 0$  rapidly for small finite incident angles. Essentially we now have a mean to predict the energy location of an ABS in the system given an incidence angle and a (variable) ratio  $\mu/m_z$ . This means that by tuning chemical potential  $\mu$  relative to the size of the magnetic energy gap in the barrier by using some voltage gates, we can change the location of an Andreev bound state in a predictable way. In figure 27 this idea is formalized. Following the density of state pictures (figure 14) in 2.2.2 we now show how the potential structure initially at  $E = 0$  starts to shift away to a finite energy  $E_{ABS}$ . The size and direction of this shift are now predicted using the result in figure 26.



(a) Andreev bound state at  $E = 0$  for  $\theta = 0$

(b) Andreev bound state at  $E_{ABS}$  for  $\theta \neq 0$

Figure 27: The density of states illustrated on the superconducting side in a MTI-TI-STI system hosting an Andreev bound state. Due to the magnetic tunnel barrier we predict to have a structure in the density of states in the form of an Andreev bound state at zero energy in the 1D limit (a). Angle dependencies (b) move the ABS away from zero energy. The size of the energy shift  $E_{ABS}$  for  $\theta \neq 0$  is predicted based on figure 26. In (b) two peaks are drawn, but the red (blue) one corresponds to positive (negative) incidence angle  $\theta$ . Image is an adaptation of [46].

#### 5.1.4 Andreev bound state, a necessary phase condition

We can actually derive a more general condition for the occurrence of an Andreev bound state in a (ballistic) system consisting of a superconductor on one side, and some form of (tunnel) barrier on the opposite side where normal reflections can occur. Using the single Andreev reflection coefficient, in basis 2, given in (5.13) we can rewrite the phase condition to

$$-2 \arccos\left(\frac{E}{\Delta_0}\right) + (-\varphi + \varphi) + \alpha_{r_{hh}^{N,(2)}} + \alpha_{r_{ee}^{N,(2)}} = 2n\pi, \quad n \in \mathbb{Z}.$$

Where the label  $N$  indicates the normal reflection at said general (tunnel) barrier. We see that the superconducting phase gain by the electron and by the hole cancel. For  $E \in (-\Delta_0, \Delta_0)$  we have  $2 \arccos\left(\frac{E}{\Delta_0}\right) \in (0, 2\pi)$ . So when the two normal reflection phase gains sum to 0, the total phase never reaches the threshold of  $2n\pi$ . This means that no bound state can occur if the two normal reflection coefficients cancel. So we can phrase a necessary condition for the occurrence of a bound state as

$$\alpha_{r_{hh}^{N,(2)}} + \alpha_{r_{ee}^{N,(2)}} \neq 0. \quad (5.24)$$

We now translate this condition on the phase gains to a condition on the reflection coefficients. As seen in the MTI-TI bi-layer, we can relate the

electron and hole normal reflections coefficients by conjugation and a general complex function with unit norm (for example  $\pm 1$ ). This result generalizes to other bi-layers or tunnel barriers, so for some complex unit norm function  $F$  we have

$$r_{hh}^{N,(2)} = F (r_{ee}^{N,(2)})^* . \quad (5.25)$$

The reason why we compare the conjugated electron reflection coefficient to the hole reflection coefficients is based on time-reversal symmetry, for details see [45] and chapter 1 in [96].

Conjugation of a complex number reverses the sign of its complex argument:  $z = |z|e^{i\alpha} \rightarrow z^* = |z|e^{-i\alpha}$ , for  $z \in \mathbb{C}$ . So the condition on the phase gains (5.24) translates to

$$\begin{aligned} \alpha_{r_{hh}^{N,(2)}} + \alpha_{r_{ee}^{N,(2)}} &= \text{Arg}(r_{hh}^{N,(2)}) + \text{Arg}(r_{ee}^{N,(2)}) \\ &= \text{Arg}(F(r_{ee}^{N,(2)})^*) + \text{Arg}(r_{ee}^{N,(2)}) \\ &= \text{Arg}(F) - \alpha_{r_{ee}} + \alpha_{r_{ee}} \\ &= \text{Arg}(F) = \begin{cases} 2 \arctan \left( \frac{\sqrt{\Re(F)^2 + \Im(F)^2} - \Re(F)}{\Im(F)} \right) & \text{if } \Im(F) \neq 0, \\ 0 & \text{if } F = 1, \\ \pi & \text{if } F = -1, \\ \text{undefined} & \text{if } F = 0. \end{cases} \end{aligned}$$

The phase criterion (5.24) tells us that this sum should be non-vanishing, hence for  $F = 1$  we do not get a bound state. This gives rise to the following necessary condition for the presence of an ABS on the relationship between the two reflections coefficients

$$r_{hh}^{N,(2)} \neq (r_{ee}^{N,(2)})^* . \quad (5.26)$$

Please note that this is a *necessary* condition for an ABS to exist in the system i.e. if a system is such that it violates the condition an ABS will not be present in the system (based on phase coherence). Meeting the condition (5.26) does not mean that an ABS is necessarily present. Badiane et al.[41] however found that in a 1D magnetic tunnel barrier, where they assumed a value of  $F = -1$  based on TRS, a non-trivial MAR  $I, V$  spectrum is expected. Their MAR results showed steps in the conduction at voltages for integer submultiples of  $\Delta_0$ . This non-trivial spectrum would, c.q. the discussion in section 2.2.2, originate from a bound state at zero energy structure in the DOS. We shall validate this finding later on by studying said 1D magnetic tunnel barrier. This means that for both 'limiting values'  $F = \pm 1$  we

have now formulated an expected relationship between the value of  $F$  and the resulting MAR spectrum and underlying zero-energy structure. So we now formulate a sharpened prediction based on the value of  $F$ :

Given a superconducting topological Josephson junction consisting of a tunnel barrier we define the ratio of the normal reflection coefficients at the tunnel barrier by

$$F := \frac{r_{hh}}{r_{ee}^*}.$$

Then the modelled multiple Andreev reflection  $I, V$  spectrum is predicted to show steps at voltage biases of

$$eV = \begin{cases} \frac{2\Delta_0}{n}, & \text{if } F = 1, \\ \frac{\Delta_0}{n}, & \text{if } F = -1, \end{cases}$$

for  $n \in \mathbb{N}$ .

Using this prediction we can link the Andreev bound states energies in the isolated systems making up the Josephson junction (e.g. the STI-TI-MTI and MTI-TI-STI making up the STI-TI-MTI-TI-STI system) to resonances in the current for the combined Josephson junction. The limiting behaviour of the MAR spectra based on  $F$  is now formulated concretely, but for intermediate (complex) values a smooth transition between the two is expected. The power of this result is that by simply computing the ratio of the normal reflection coefficients in the tunnel barrier, we can predict striking features of the complete complex Josephson junction hosting multiple Andreev reflections.

### 5.1.5 TI-MTI-TI-STI transmission

Another interesting quantity to model is the conduction through a system that allows Andreev bound states, e.g. a TI-MTI-TI-STI system as shown in figure 20. As seen in figure 26, the MTI-TI-STI sub-system allows for Andreev bound states. A natural question would be in what way these Andreev bound states would show up in for instance a conduction measurement. Since we model systems by using steady-state solutions to the BdG equations, temporal effects are not taken into consideration. This means that modelling a non-equilibrium effect such as conduction is not possible. We can however compute the transmission of an electronic wavefunction through a full TI-MTI-TI-STI system. The transmission can be seen as the probability of an

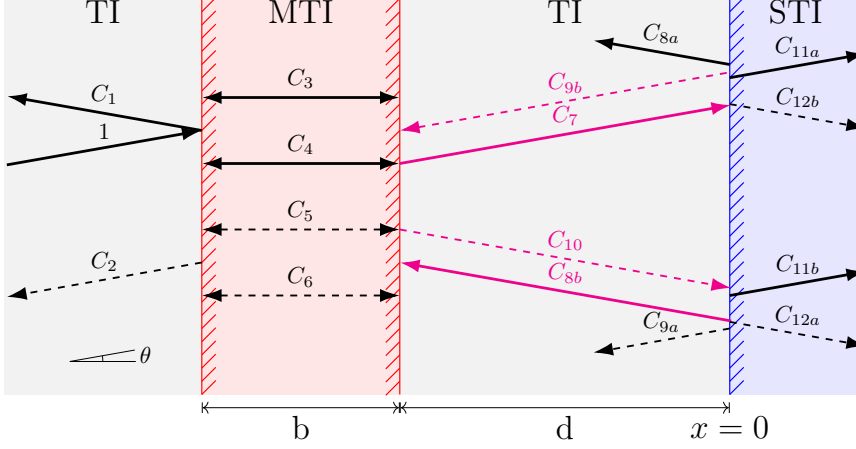


Figure 28: The schematic representation showing the 2D  $(x, y)$  top-view of the topological insulator 'set-up' depicted in figure 20. This figure illustrates the possible types of reflections and transmission occurring in a ballistic 2D TI-MTI-TI-STI junction. The solid and dashed lines refer to electron and hole wavefunctions respectively. The indicated angle  $\theta$  is defined for electrons positive x-direction respectively. The system essentially consists of two parts, on the left we consider charge carriers tunnelling from the left-most TI through the magnetic tunnel barrier into the MTI-TI-STI sub-system. In this right sub-system, the Andreev bound states can occur, as is indicated by the magenta-coloured wavefunctions in the middle TI.

incident electron propagating through the entire system. We take the transmission as an analogy to the conduction  $G$ .

To model the transmission through the system illustrated in figure 28 we consider the left TI as an electrode from which charge carriers (electrons) tunnel into to MTI-TI-STI system that hosts ABS. The 'experiment' we simulate is the effect of the ABS on the reflection or transmission of an incoming electronic wavefunction (indicated by the amplitude 1). We compute the transmission by imposing the continuity of each wavefunction indicated in the figure 28 at each relevant interface, solving the associated matrix for the complex wave amplitudes and then computing the transmission based on these coefficients. The set of continuity requirements that form the to be solved linear system and the meaning of the coefficients in figure 28 is given in appendix C.1.

By charge conservation, we can calculate the transmission at any physical location (vertical cross-section) in the system, the most convenient place is just inside the left TI region[65]. With that choice, we start with an electronic wavefunction of amplitude 1 and we wish to compute the probability

of its charge passing through the entire system and leaving it at the right STI. It can either pass through entirely or scatter around in the system and get reflected back as an electron (negative contribution to the charge transmission) or as a hole (positive contribution to the charge transmission). The transmission of charge can thus be modelled solely by two coefficients,  $C_1$ , and  $C_2$  being the complex amplitudes of the reflected electron and hole wavefunctions in figure 28 respectively

$$T = (1 - |C_1|^2 + |C_2|^2). \quad (5.27)$$

The route towards finding the complex amplitudes is similar to solving the two bi-layer problems above, however, we now have three interfaces that we can not solve separately. For instance, the coefficient  $C_7$  in figure 28 would be present in the continuity requirement at the MTI-TI interface as well as in the one at the TI-STI interface. This means we arrive at three coupled linear equations of dimension four. That is, we have twelve equations for 12 unknowns ( $12a$  and  $12b$  describe the same wavefunction, but result from a different process, so they can be described by a single unknown coefficient). In appendix C.1 we give the specific continuity requirements and the wavefunctions considered. We then solve the  $12 \times 12$  associated matrix for the unknown coefficients and compute the transmission according to (5.27).

The transmission is solved as a function of the incoming electron's energy ( $E$ ) and angle of incidence ( $\theta$ ), this gives rise to a two-dimensional heat map with the transmission shown as a colour gradient. The results are shown in figures 29a through 29d. In each 2D heatmap, the phase coherence ABS curves are shown in figure 26 are drawn on top of the 2D heatmap for the same inputs. The charge transmission through the system goes to 2 (transmission has no physical units), as is typical for Andreev bound state conductance [97], at exactly the locations traced out by the phase coherence criterion curves indicated by the overlaid green lines. The transmission then gradually drops to 0 away from this curve. When we consider the parameters precisely such that the ABS occurs, an incoming charge is fully transmitted and a charge carrier with opposite charge is reflected, giving rise to the transmission of 2. Hence these 2D transmission heatmaps exactly agree with the predicted locations of the ABS in figure 26.

Experimentally it is not straightforward<sup>17</sup> to compute a single angle component of the conduction, so when we naively measure the conduction through

---

<sup>17</sup>It is most certainly possible to study the angle dependency in a conduction experiment by e.g. varying the vertical extend ( $y$  thickness) of the system.

our system we would measure an angle averaged conduction. Since we take the transmission as an analogy to the conduction, we consider the angle averaged transmission given by

$$\bar{T}(E) = \frac{1}{\pi} \int_{-\pi/2}^{\pi/2} T(\theta, E) \cos \theta d\theta. \quad (5.28)$$

Figure 29e shows the angle averaged transmission for the various values of  $m_z$ . This result agrees with Tanaka's observation [38] that "the resulting transmission has a zero-bias peak originating from the peak of  $T$  at resonance energies. As seen from figure 26, the slope of the curve around  $E = 0$  becomes gradual with the decrease of  $\mu/m_z$ . Then, the contribution around  $E = 0$  becomes significant in the integral in (5.28) and the resulting height of the zero-bias peak is enhanced with the decrease of the magnitude of  $\mu/m_z$  as shown in figure 29e".

## 5.2 Majorana mode chirality inversion

The demonstrated chiral Majorana modes emerging in the form of ABS in the MTI-STI system shown in figure 26 are sensitive to perturbations of parameters of the system. Even though these predicted CMM on the interface between an MTI and STI by Fu and Kane[1] are protected by the bulk gap and its topological property it was demonstrated by Tanaka [38] and recently by Vela et al. [39] that by changing certain parameters these CMM can be inverted. That is, the direction of motion of these chiral Majorana fermions is inverted when altering specific quantities. As pointed out by [39], "The chirality inversion is a unique signature of chiral Majorana fermions in a spinful topological superconductor: it does not exist for spinless chiral  $p$ -wave pairing. Moreover, the inversion can be detected in a transport experiment, both in thermal and in electrical conduction". This opens up the possibility for experimental studies of CMMs in topological superconducting devices.

It was shown that by flipping the sign of the magnetic energy gap  $m_z \rightarrow -m_z$  in the MTI the CMM propagation directions are inverted [38]. Alternatively [39] demonstrated that a counterflow of supercurrent inverts the propagation direction of the chiral Majorana fermions. In this work, we first consider the mirrored version of the MTI-TI-STI system and study the CMM emerging as Andreev bound states therein. Next we validate [38] by showing the inversion of the curve in 26 upon flipping the direction of the magnetization  $\mathbf{m}$  in the ferromagnet. After that, we demonstrate an alternative yet simple procedure to inverse the CMM by tuning the ratio of the

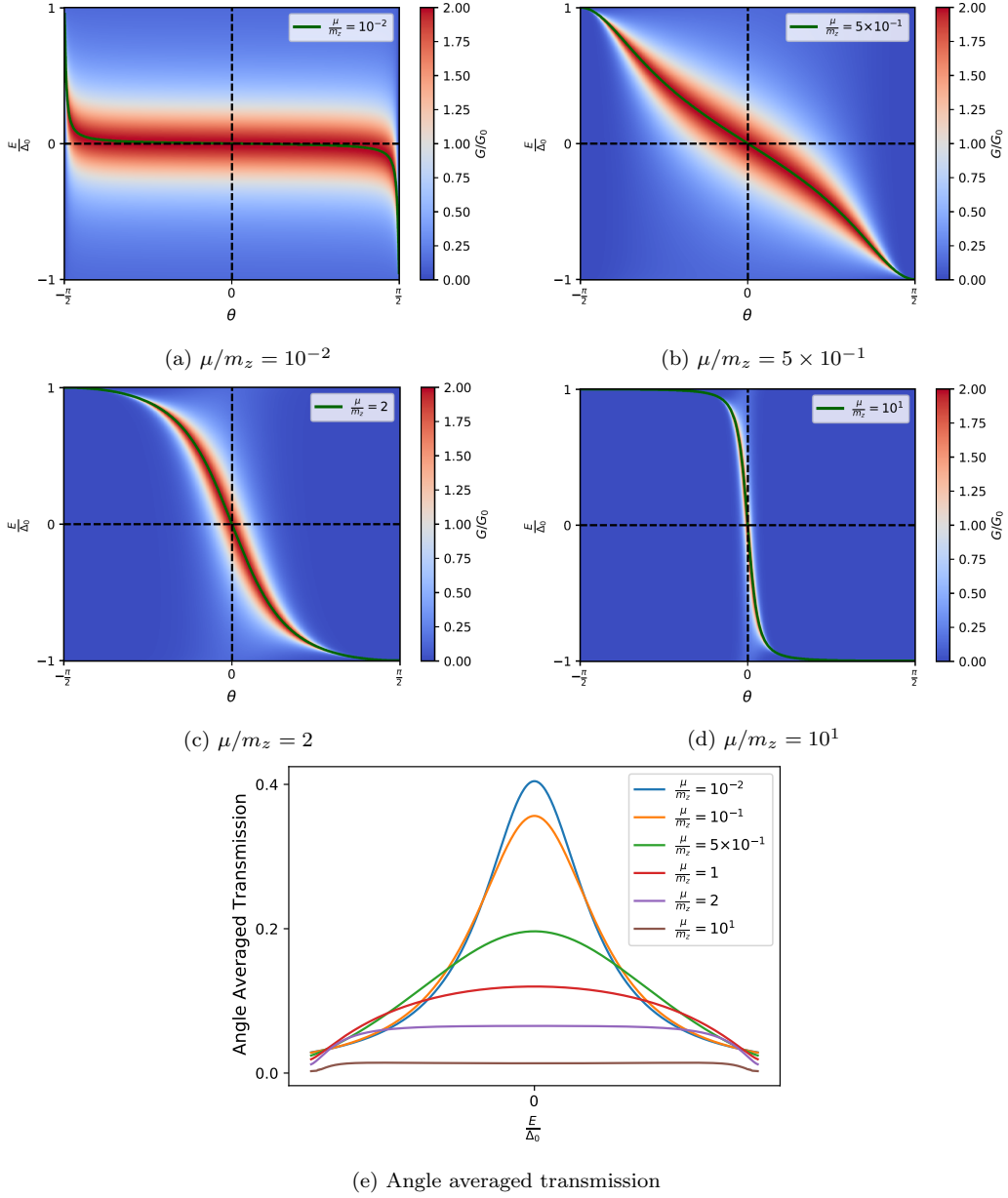


Figure 29: The four figures (a-d) showing the transmission (as analogy to the conductance  $G$ ) of an electron through the system shown in figure 28 for various values ratios of the chemical potential in the TIs over the strength of the magnetic gap in the MTI ( $\mu/m_z$ ). The curves are drawn for a vanishing chemical potential in the MTI,  $\mu_m = 0$ , an equal chemical potential in the TIs and STI,  $\mu_s = \mu$  that is a varied relative to  $m_z = 800\Delta_0$  to get the shown ratios, the width of the tunnel barrier is  $b = \hbar v_f/m_z$ . The 'conductance'  $G$  is normalized by  $G_0 = \frac{2e^2}{h}$ . The additional green line in each subfigure is the phase coherence condition curve for equal parameters, i.e. the curves in figure 26. Figure e shows the angle averaged transmission for various ratios  $\frac{\mu}{m_z}$ .

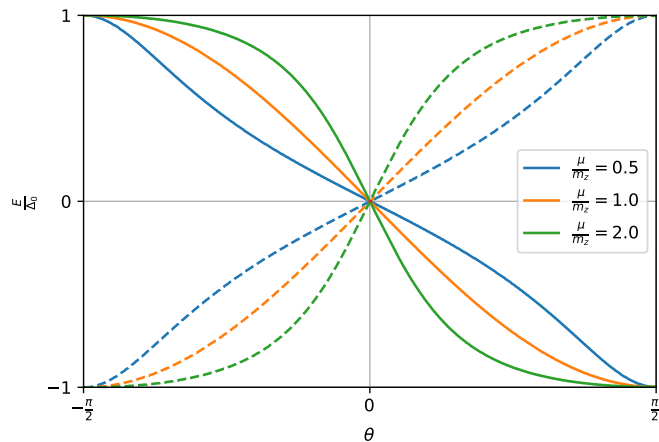


Figure 30: The chiral Majorana mode bound state energies as a function of the angle of incidence for a MTI-TI-STI system drawn as solid lines and its mirror STI-TI-MTI in dashed lines. Here,  $m_z = 800\Delta_0$ ,  $\mu_m = 0$ , and  $\mu = \mu_s$  is varied to get the ratios shown in the legend.

chemical potentials in the TI and MTI:  $\frac{\mu}{\mu_m}$ .

In the considered the MTI-TI-STI system, CMM emerge at energies and angles indicated by the solid lines in figure 30. When we mirror this system and study an STI-TI-MTI system, we would expect that the bound state energies do not change, since geometrically speaking this would be equivalent to a  $\pi$  rotation of the original system. If we apply a  $\pi$  shift to the result in figure 26 we get the same result. Moreover in basis 2 it was shown that under the assumption  $\mu = \mu_s$  (which we take in all the results in this work) that the Andreev reflection coefficients were angle independent, and it is easily checked that for  $\theta \rightarrow \theta + \pi$  the normal reflections (5.17), (5.20) at the MTI remain unchanged.

This geometric argument is valid, but we should be careful what angles we compare in the full Josephson junction. We are trying to model the full STI-TI-MTI-TI-STI system, where the two separated systems are coupled by a magnetic tunnel barrier. To implement the coupling correctly we have to match the angles of the particles tunnelling between the two systems such that they remain travelling under the same angle. Compare for instance the incidence angles of the wavefunctions in figure 28 marked by  $C_1$  and  $C_8$ . We need to do an additional  $\theta \rightarrow -\theta$  transformation to accommodate the fact that we now parametrize the entire compound system for a fixed single theta. Upon the change  $\theta \rightarrow \pi - \theta$  we do see the inversion of energies in the ABS

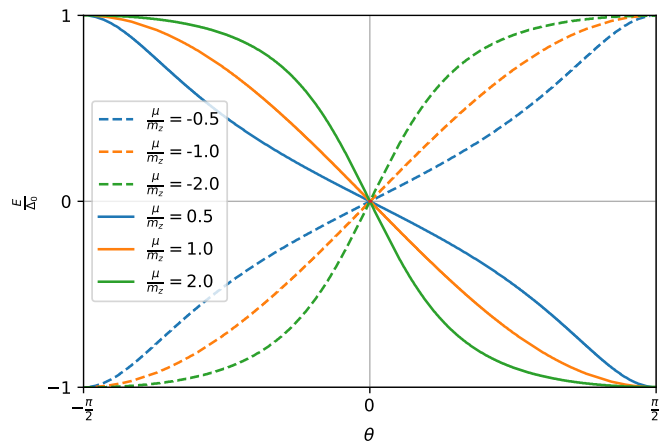


Figure 31: The chiral Majorana mode bound state energies as a function of the angle of incidence for a MTI-TI-STI system drawn as solid (dashed) lines for  $m_z > 0$  ( $m_z < 0$ ). It shows chiral Majorana mode inversion under the flip  $m_z \rightarrow -m_z$ . Here,  $|m_z| = 800\Delta_0$ ,  $\mu_m = 0$ , and  $\mu = \mu_s$  is varied to get the ratios shown in the legend.

curve.

When we solve the same problem as for the MTI-TI-STI system documented in section 5.1, but now for an STI-TI-MTI system with a left moving electron inbound on the STI-TI interface under angle  $\pi - \theta$  we get the dashed curve in figure 30. This means that indeed if we considered the mirrored system with the additional requirement that we invert the travel direction of the bound state, the CMM bound state energies invert too. This result should not be considered as an inversion of CMM due to some perturbation of a parameter, because the CMM simply propagate in an opposite direction  $\theta \rightarrow \pi - \theta$  because we have defined them to do so to make a fair comparison in the compound Josephson junction. This example illustrates the fact that reversing the propagation direction of the CMM gives rise to the inversion of the sign of the  $E_{ABS}$  vs  $\theta$  curve.

In figure 31 the dashed (solid) curves show the bound state energies in a MTI-TI-STI system for a negative (positive) value of  $m_z$  as a function the incidence angle  $\theta$ . As we flip the orientation of the magnetisation in the ferromagnet we see that the bound state energies change sign, which is equivalent to the inversion of their propagation direction. That is, upon reversing the direction of the induced magnetisation we invert the direction of motion of the CMMs, as was previously found by [38].

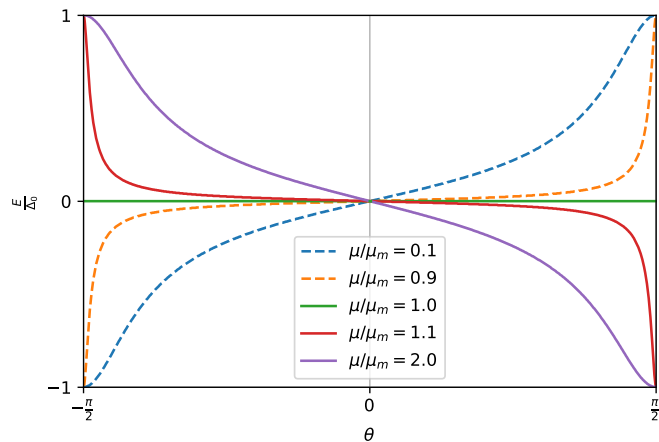


Figure 32: The chiral Majorana mode bound state energies as a function of the angle of incidence for a MTI-TI-STI system drawn as solid (dashed) lines for  $\frac{\mu}{\mu_m} > 0$  ( $\frac{\mu}{\mu_m} < 0$ ). It shows chiral Majorana mode inversion under the gradual change  $1 > \frac{\mu}{\mu_m} > 1$ . Here,  $m_z = 4\mu_m = 800\Delta_0$ , and we vary  $\mu = \mu_s$  to get the ratios in the legend.

An alternative method to achieve the observed CMM inversion in an MTI-TI-STI system proposed here is by tuning the ratio of the chemical potentials of the TIs and MTI. Figure 32 shows the Andreev bound state energies for a decreasing ratio  $\frac{\mu}{\mu_m}$ . The magnetic energy gap is chosen sufficiently large ( $4\mu$ ) to guarantee that the MTI acts reflectively. As the ratio surpasses the threshold  $\frac{\mu}{\mu_m} = 1$  the chiral Majorana modes get inverted and their propagation direction is altered. When the ratio is exactly 1 the bound state remains fixed at zero energy for all incidence angles.

An analogous situation can help to illustrate the reason for the observed instantaneous chiral inversion as the ratio of the chemical potential surpasses unity. We can consider the situation  $\mu/\mu_m > 1$  ( $\mu/\mu_m < 1$ ) as the reflection of an incident traveling wave in a material towards a potential drop (barrier). The former gives no phase gain, whereas the latter has a  $\pi$  phase gain. In the pedagogical example of a  $V_0$  step-function potential for a 1D Schrödinger equation [25] this instantaneous phase dependence is also observed. This phenomenon is similar to a travelling wave on a rope meeting either a loose or fixed boundary condition. A fixed boundary condition reflects the travelling wave, and a loose one does not. The reflection reflected wave gets a  $\pi$  phase gain.

In the MTI-TI-STI system, we see that at the transition point  $\frac{\mu}{\mu_m} = 1$  a sudden phase shift is observed. This effect is most notable in the comparison

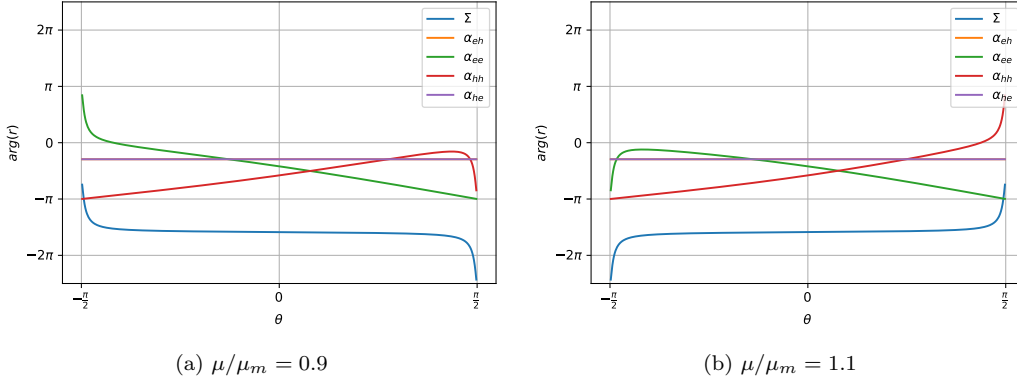


Figure 33: Complex argument of the calculated reflection coefficients in a MTI-TI-STI system as a function of the incidence angle. The curves are drawn for a fixed energy and we have  $m_z = 4\mu_m = 800\Delta_0$ , and we vary  $\mu = \mu_s$  to get the ratio in (a) or (b). The blue curve labeled by  $\Sigma$  is the sum of the other four. When the blue line crosses  $2n\pi$ ,  $n \in \mathbb{N}$  the reflection coefficients add up phase coherently.

of the complex arguments of the normal reflection coefficients for the ratio  $\frac{\mu}{\mu_m}$  being lesser and greater than unity. Figure 33 shows the complex arguments of the relevant reflection coefficients that make up the bound state. The Andreev coefficients  $r_{eh}, r_{he}$  are indeed equal for all  $\theta$  and only shift laterally for changing energies. The normal reflections  $r_{ee}$  and  $r_{hh}$  show a global linear slope of  $\pm\theta$ , except for the sudden drop or rise near  $\theta \rightarrow \pm\frac{\pi}{2}$ . Observe that when comparing the phases before and after the transition point (figures 33.(a) and (b)) that the sudden phase shift in the normal reflections near  $\theta = \pm\frac{\pi}{2}$  is inverted. Effectively the summed blue curve flips, consequently, the bound state energies are inverted too. This sudden transition is responsible for the observed inversion.

### 5.3 Multiple Andreev reflections

We now focus on the multiple Andreev reflections possible in the topological Josephson junction consisting of two superconducting leads connected by a tunnel barrier. Figure 3 serves as an illustration of the system when the tunnel barrier is due to a ferromagnetic insulator inducing a magnetic energy gap into a region of the TI. Essentially this system is the symmetric realization obtained by connecting the MTI-TI-STI system (figures 20 and 21) studied in the previous section with its mirrored image: STI-TI-MTI. As explained in section 2.2.2, the  $I, V$  curves for a system hosting MAR are greatly influenced by the potential structure at  $E = 0$ . Here we investigate two types of barriers, i.e. a tunnel barrier due to a Fermi surface mismatch and a

magnetic tunnel barrier, and study the resulting  $I, V$  curves by numerically solving the so-called recurrence relations (detailed descriptions in [40], [46], and [41]). The approach shown here is general, in the sense that, by solving the recurrence relations for the resulting MAR  $I, V$  spectra and using those to probe a potential structure around  $E = 0$  in the density of states, is also applicable to non topological Josephson junctions (e.g. a superconductor-ferromagnetic insulator-superconductor).

First in sections 5.3.1 and 5.3.2 we study the reflection and transmission through each barriers and compare these properties for electrons and holes by computing the complex factor  $F$ . Based on (the real part of)  $F$  for each barrier we use the phase coherence result from section 5.1.4 to predict the global shape of the MAR  $I, V$  spectra of the Josephson junctions consisting of such a barrier. Next in section 5.3.3 we generalize and solve the recurrence relations derived in [46] to also accommodate this factor  $F$ . The factor  $F$  introduces the non-trivial difference between the electron and hole interaction with the tunnel barrier to the recurrence relations. Next, the adapted recurrence relations are solved numerically to reveal the (asymmetric)  $I, V$  curves, which are then analysed to reveal the potential structure in the DOS around  $E = 0$  for both types of barriers. Final, we relate the peaks in the  $I, V$  curves for a 2D MTI tunnel barrier to the CMM bound state energies found in section 5.1. Concretely, we relate the bound state energies obtained from the two isolated systems (see figure 30) to the entire Josephson junction when now the two systems communicate through the tunnel barrier. This coupling could delocalize the bound state energies as predicted by [45], but this effect is discussed later on (section 6).

### 5.3.1 Fermi surface mismatch tunnel barrier

Consider a system of the form STI-TI-TI'-TI-STI. The prime in the middle TI indicates a Fermi surface mismatch (FSM) relative to its neighbours, which makes it act as a (tunnel) barrier. The middle tunnel barrier TI-TI'-TI system was already introduced and studied in section 4.4.2 to illustrate the tool's functioning. There we introduced the propagation angle  $\theta'$  in the middle TI' barrier, different from  $\theta$  in its neighbouring sites to model the FSM effect. We derived the electron normal reflection coefficient, (4.8), for an electron incoming from the left TI under an angle of  $\theta$ , here we study the equivalent scattering process for an incoming hole under angle  $-\theta$ , in basis 2.

Since the electron case was derived in section 4.4.2 we now consider an inbound hole. The continuity of the hole spinors is imposed at  $x = 0$  and

$x = b$  giving

$$\phi_{h-}^{TI,(2)}(-\theta) + r_{hh}^{(2)} \phi_{e-}^{TI,(2)}(\pi + \theta) = A_h^{(2)} \phi_{h-}^{TI,(2)}(-\theta') + B_h^{(2)} \phi_{h-}^{TI,(2)}(\pi + \theta'), \quad (5.29)$$

evaluated at the origin, and

$$A_h^{(2)} \phi_{h-}^{TI,(2)}(-\theta') + B_h^{(2)} \phi_{h-}^{TI,(2)}(\pi + \theta') = t_{ee}^{(2)} \phi_{h-}^{TI,(2)}(-\theta), \quad (5.30)$$

evaluated at  $(x, y) = (b, 0)$ . Again we cast the set of continuity requirements to a matrix-vector system that we then algebraically solve for the hole hole normal reflection coefficient

$$r_{hh}^{(2)}(-\theta) = \frac{2e^{-i\theta} \sin(k_{xh}b) (\sin \theta - \sin \theta')}{e^{ik_{xh}b} \cos(\theta + \theta') + e^{-ik_{xh}b} \cos(\theta - \theta') + 2i \sin(k_{xh}b)}. \quad (5.31)$$

This results is strikingly similar to the previously derived electron electron normal reflection (4.8). In fact we can relate the two by

$$\boxed{r_{hh}^{(2)}(-\theta) = r_{ee}^*(\theta)}. \quad (5.32)$$

To phrase it in terms of the complex function  $F$  introduced to study the phase coherence criterion in section 5.1.3, we find that  $F_{TI} = 1$ . So based on the prediction formulated there, a FSM tunnel barrier violates the necessary condition for the formation of an ABS. Hence we predict that there will be no structure in the DOS around  $E = 0$  on either side of a system comprising of a FSM tunnel barrier. The resulting  $I, V$  curve should therefore be trivial, i.e. it will globally obey (2.7) and thus show prominent steps in the current for biases of  $eV = 2\Delta_0/n, n \in \mathbb{N}$ .

### 5.3.2 Magnetic tunnel barrier

We now consider the topological Josephson junction comprising of a magnetic tunnel barrier, i.e. a STI-TI-MTI-TI-STI system. Through this change, we introduce normal reflections in the middle TI-MTI-TI sub-system for energies in the forbidden region in the MTI band structure. The forbidden energy range in the MTI's band structure is parameterized by the induced magnetic energy gap  $m_z$ . The barrier is illustrated in figure 34. Again we solve for the electron and hole normal reflection coefficients  $r_{ee}$  and  $r_{hh}$ .

An incoming electron (hole) from the left TI is inbound on MTI under an angle of  $\theta$  ( $-\theta$ ). By imposing the continuity of the spinors at each interface (we take the first interface at  $x = 0$  and hence the second at  $x = b$ ), we

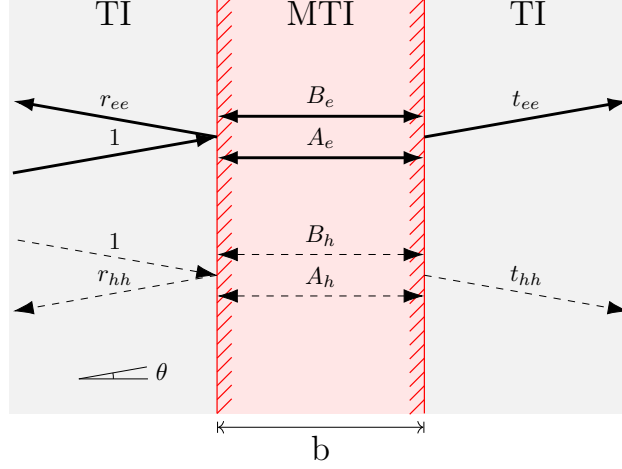


Figure 34: A schematic illustration of an incoming electron (hole) from a TI traveling under an angle  $\theta$  ( $-\theta$ ) undergoing normal reflection  $r_{ee}$  ( $r_{hh}$ ) or transmission  $t_{ee}$  ( $t_{hh}$ ) for a double barrier system consisting of a MTI. The magnetic field in the middle MTI results in a nonzero possibility for normal reflection to occur, and an exponentially decaying tunneling probability is present giving rise to a finite transparency ( $D := 1 - rr^*$ ). In the MTI the spinors become evanescent waves, so we consider the superposition of an increasing and decreasing evanescent wave.

can build a system corresponding to these two requirements. For an initial electron we evaluate the following equations

$$\phi_{e+}^{TI,(2)}(\theta) + r_{ee}^{(2)} \phi_{e+}^{TI,(2)}(\pi - \theta) = A_e^{(2)} \phi_e^{MTI,+,(2)}(\theta) + B_e^{(2)} \phi_e^{MTI,-,(2)}(\theta), \quad (5.33)$$

$$A_e^{(2)} \phi_e^{MTI,+,(2)}(\theta) + B_e^{(2)} \phi_e^{MTI,-,(2)}(\theta) = t_{ee}^{(2)} \phi_{e+}^{TI,(2)}(\theta), \quad (5.34)$$

at the origin and at  $(x, y) = (b, 0)$  respectively. We arrive at similar<sup>18</sup> continuity requirements for an incoming hole travelling in the  $-\theta$  direction. We solve this set of equations for the electron and hole normal reflection coefficients. Due to the enhanced complexity of the MTI spinors, a comprehensible algebraic expression can not be given for the reflection coefficients. We therefore, need to reduce the complexity algebraically and study limiting behaviour, or study the original outcome graphically.

First we plot the real and imaginary part of the complex ratio  $F_{MTI}^{(2)}(\theta, \mu)$  defined by

$$r_{hh}^{(2)}(-\theta) = r_{ee}^*(\theta) F_{MTI}^{(2)}(\theta, \mu), \quad (5.35)$$

<sup>18</sup>Simply change the subscript  $e$  to  $h$  and choose the  $-$  solution rather than the  $+$  for the TI wavefunctions and evaluate it for  $\theta \rightarrow -\theta$

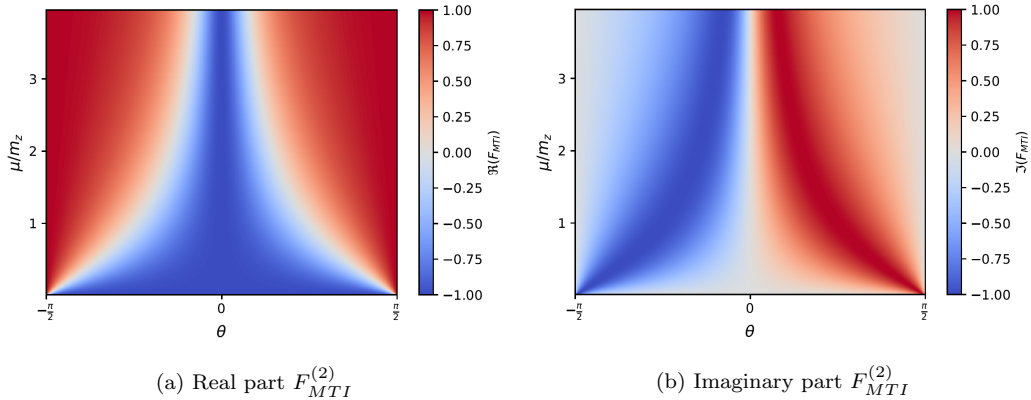


Figure 35: The the real (a) and imaginary part (b) of the ratio  $F_{MTI}^{(2)} = r_{hh}(-\theta)/r_{ee}^*(\theta)$  as a function of the incoming angle  $\theta$  and the chemical potential in the TIs over the magnetic energy gap ( $\mu/m_z$ ) for the double barrier junction given in figure 34. The chemical potential in the MTI is zero, and the width of the barrier is  $b = \hbar v_f/m_z$ . Here,  $m_z = 800\Delta_0$  and  $\mu = \mu_s$  is varied to get the ratios shown on the  $y$ -axis.

to graphically quantify the relationship between them. Figure 35 shows the real and imaginary part of this ratio as a function of  $\theta$  and the chemical potential in the TI relative to the magnetic energy gap in the MTI. The chemical potential in the MTI is taken to be zero, and the width of the barrier is of the order of  $\hbar v_f/m_z$ . We consider the real part  $F$  first for two limiting values  $(-1,1)$  in the figure 35a. In the 1D limit for a weak magnetic barrier  $\Re(F_{MTI}^{(2)}) = -1$ , but for sufficiently strong magnetisation and finite incidence angles the real part of  $F_{MTI}^{(2)}$  goes to -1. Moreover, there is a smooth transition from  $F_{MTI}^{(2)} = -1$  around  $\theta = 0$  and for small values of  $\mu$  relative to  $m_z$  to  $F_{MTI}^{(2)} = 1$  for almost vertical incidence angles.

To reiterate, the value of  $F_{MTI}^{(2)}$  can be used to predict the possibility of the system having a nontrivial  $I, V$  spectrum due to a structure at  $E = 0$  on the DOS based on the prediction formulated in section 5.1.4. A value of +1 corresponds to the violation of the necessary Andreev bound state phase criterion (5.26) whereas a value of -1 is a strong indication of a potential nontrivial  $I, V$  curve. Based on this, we predict that in the STI-TI-MTI-TI-STI system we can smoothly transition from a trivial  $I, V$  curve ( $F_{MTI}^{(2)} = 1$ ) to a nontrivial  $I, V$  curve ( $F_{MTI}^{(2)} = -1$ ) by changing the incidence angle.

From the graphical survey using figure 35 we could already observe that in the 1D limit ( $\theta = 0$  cross-section)  $F_{MTI}^{(2)} = -1$ , but now we further study the system by considering the 1D limit algebraically. In a 1D limit,  $\theta \rightarrow 0$ ,

we reduce the length of the algebraic expression for the electron and hole normal reflection coefficients considerably. From the 1D reflection coefficients, we can moreover study the transparency  $D := 1 - rr^*$  of a magnetic topological tunnel barrier and compare it to literature [41]. Hence this limit could further validate the correctness of the tool's implementation.

We take the lengthy algebraic relations for the reflection coefficients that give rise to figure 35 and set  $\theta = 0$ . For the  $r_{ee}(\theta = 0)$  coefficient we find

$$r_{ee}(\theta = 0) = \frac{-A \sinh b\kappa_e}{C \sinh b\kappa_e - iB \frac{\hbar v_f \kappa_e}{m_z} \cosh b\kappa_e}, \quad (5.36)$$

where the terms  $A, B$  and  $C$  are given by

$$\begin{aligned} A &= m_z + 2 \frac{E\mu_m}{m_z} - (E + \mu_m), \\ B &= m_z - (E + \mu_m), \\ C &= \frac{E^2}{m_z} + \frac{\mu_m^2}{m_z} - (E + \mu_m). \end{aligned}$$

For  $r_{hh}(\theta = 0)$  we arrive at

$$r_{hh}^{(2)}(\theta = 0) = \frac{A^{(2)} \sinh b\kappa_h}{-C^{(2)} \sinh b\kappa_h + iB^{(2)} \frac{\hbar v_f \kappa_h}{m_z} \cosh b\kappa_h}, \quad (5.37)$$

with the terms

$$\begin{aligned} A^{(2)} &= m_z - 2 \frac{E\mu_m}{m_z} - (E - \mu_m), \\ B^{(2)} &= m_z - (E - \mu_m), \\ C^{(2)} &= \frac{E^2}{m_z} + \frac{\mu_m^2}{m_z} - (E - \mu_m). \end{aligned}$$

For a fair comparison to the result in figure 35 we take  $\mu_m = 0$  here too. Based on the order magnitudes of the energy scales  $E, \Delta_0, \mu$  and  $m_z$  in section 3.2.4, terms of order  $m_z$  or  $\mu$  dominate over those of order  $E$ . We recall that since  $\hbar v_f \kappa_{e,h}(\theta = 0) = \sqrt{m_z^2 - (E \pm \mu_m)^2} = -iq_{e,h}(\theta = 0)$  the  $\hbar v_f \kappa_{e,h}$  terms approximately equal  $m_z$ . This means that the terms with  $C$  and  $C^{(2)}$  are small and we can safely neglect them. Using this we find in the large  $m_z$  limit

$$\boxed{r_{hh}^{(2)}(\theta = 0) = -r_{ee}^*(\theta = 0)}. \quad (5.38)$$

So in the 1D limit, we retrieve  $F_{MTI}^{(2)} = -1$ , as we found graphically in the 2D case given in figure (5.35). In literature this value was assumed of a 1D

magnetic topological junction based on time reversal symmetry [41].

As a final check, we compute the transparency in the 1D limit and compare it to literature [41]. From the reflection coefficients, we can derive the transparency in the 1D limit, since the two reflection coefficients are related by a unit one factor (-1) we can pick either coefficient to compute  $D$ . We find

$$R = r_{ee}^*(\theta)r_{ee}(\theta) = \frac{A^2 m_z^2 \sinh^2 b\kappa_e}{C^2 m_z^2 \sinh^2 b\kappa_e + m_z^2 \hbar v_f \kappa_e^2 \cosh^2 b\kappa_e} \rightarrow \tanh^2 b\kappa_e$$

in the 1D limit. So we retrieve the transparency found by Badiane et al. [41]

$$D(\theta = 0) = [1 + \sinh^2(b\kappa)]^{-1}. \quad (5.39)$$

### 5.3.3 Recurrence relations

In quantum transport, a key physical observable to model is the conduction through a quantum device. Since conduction arises from a non-equilibrium situation (voltage bias) and the BdG equations considered in this work are solved in a steady-state, we can not directly model the conduction. We therefore, resort to the so-called recurrence relations. Here we briefly introduce the physical origin of the recurrence relations and refer to [40] and [46] for a derivation. Then we show in detail how the recurrence relations change when introducing the complex factor  $F$  to account for a non-trivial tunnel barrier. Then we solve and analyse the adapted recurrence relations and relate the results to the prediction based on the phase coherence criterion for the ABS formulated in section 5.1.4.

As explained in section 2.2.2 charge carriers in a system hosting MAR gain energy when traversing through the applied external electric field resulting from an applied voltage difference over the superconducting leads. Each consecutive scattering event changes the complex amplitude of the electron's (or hole's) wavefunction. This means we get a sequence of complex amplitudes,  $(A_n)_{n \in \mathbb{N}}$  for right-moving electrons and  $(B_n)_{n \in \mathbb{N}}$  for left moving electrons, based on the number of times,  $n$ , Andreev reflections has taken place. The recurrence relations in short arise from matching the various wavefunctions for all comprising charge carriers in the system, accounting for these energy gains, at the interface by using so-called scattering matrices. By matching the wavefunctions, we get a set of equations expressing the amplitude of the  $j$ th term in  $(A_n)_{n \in \mathbb{N}}$  in terms of previous terms in the sequence. Similarly for  $(B_n)_{n \in \mathbb{N}}$ . The recurrence relations are derived for a SNS junction in [40]

and for a topological junction in [46].

The reason for the focus on the ratio  $F$  between the electron- and hole normal reflection coefficients for the tunnel barriers is because this term enters the recurrence relations through the so-called scattering matrices used to derive them. In literature [40],[41] derivations of the recurrence relations always assumed a 'simple' value of  $F = \pm 1$  depending on the type of tunnel barrier. In this work we showed (section 5.3.2) that in 2D systems using a magnetic barrier the value of  $F_{MTI}^{(2)}$  is complex and transitions between these two limiting values for varying parameters. In fact, we showed in section 5.1.4 that the factor is used as a mean to predict whether a certain system would have a non-trivial  $I, V$  spectrum and hence act as a strong indication for the existence of a zero-energy bound state. To study non-equilibrium effects, we thus need to adapt the recurrence relations to accompany this factor.

The way  $F$  enters the equations is through the scattering matrices. A derivation of the recurrence relations is given in the appendix D. There we highlight where  $F$  enters and how it changes the original recurrence relations.  $(B_n)_{n \in \mathbb{N}}$  is described by a non-homogeneous three-term recurrence of the form

$$B_{n+1} + \gamma_n B_n + \chi_n B_{n-1} = \zeta_n \delta_{n0}, \quad (5.40)$$

where the terms  $\gamma_n, \chi_n$  and  $\zeta_n$  are given in the appendix D. These coefficients are made up of the energy dependent Andreev coefficient after successive reflections,  $a_n = a(E + neV)$  for  $a$  given in (5.13), the factor  $F$  and the transparency of the tunnel barrier defined by  $D := 1 - r_{ee} r_{ee}^*$ .  $(A_n)_{n \in \mathbb{N}}$  is described by a non-homogeneous two term recurrence of the form

$$A_{n+1} + \gamma'_n A_n = f(n), \quad (5.41)$$

where again  $\gamma'_n$  and  $f(n)$  are given in the appendix D. For (5.41) we should note that the  $f(n)$  is dependent on the sequence  $(B_n)_{n \in \mathbb{N}}$ , thus we should solve (5.40) before (5.41).

We shortly describe the (three and two-term) recurrence relations and the stability of possible algorithms. A two-term recurrence relation is a linear first-order equation whereas a three-term recurrence relation is of second order. Hence the former has only one solution, but the latter has two linearly independent solutions. Thus if we're not careful we could numerically land on either solution. This fact makes constructing a stable algorithm for finding a specific single solution to a three-term recurrence relation non-trivial.

The reader is referred to [46] for an excellent analysis of the stability of solutions to and possible algorithms for non-homogeneous two and three-term recurrence relations.

The recurrence relations analysed in [46] are the ones given in (5.40) and (5.41) for the case  $F = -1$ . In the current work, we allow for a general complex  $F \in \mathbb{C}$  in the recurrence relations. The stability analysis in [46] remains valid in this case, with one caveat that the matrix inversion method (implemented through the use of the Matlab backslash operator) is no longer stable. The matrix inversion method was the fastest algorithm studied in [46], but fortunately, it was shown that the slower so-called backwards recurrence algorithm remains usable. As concluded by the author: "the backslash operator algorithm turns out to be much faster than the backward recurrence algorithm, however, when using the backward recurrence algorithm, we can be absolutely sure that the numerical solution is the solution we are looking for. The backslash operator might still give a diverging solution for certain (unknown) parameter sets." The recurrence relations are solved numerically in this work by the method of forward elimination, by backward substitution [98],[99].

After obtaining  $(B_n)_{n \in \mathbb{N}}$  and then  $(A_n)_{n \in \mathbb{N}}$  numerically by solving (5.40), and (5.41) we compute the DC current using [46]

$$I_{DC} = \frac{e}{\pi \hbar} \left[ eVD - \int J(E) \left\{ a_0^* A_0^* + a_0 A_0 + \sum_n (1 + |a_{2n}|^2) (|A_n|^2 - |B_n|^2) \right\} dE \right]. \quad (5.42)$$

Note that  $J(E) = \sqrt{1 - a_0^2}$ . By repeating this process for varying biases  $eV$  we get the DC current as a function of the applied voltage. We normalize the current by the conductance quantum  $G_0 = \frac{2e^2}{h}$  and the tunnel barrier's transparency  $D$ ,  $\overline{I_{DC}} = \frac{I_{DC}}{DG_0}$  and draw the  $I, V$  curves.

### 5.3.4 Fermi surface mismatch tunnel barrier spectrum

We derived that  $F_{TI} = 1$ , and thus hypothesized that a system comprising of a Fermi surface mismatch tunnel barrier would have a trivial  $I, V$  spectrum, i.e. show increases in the current at integer submultiples of  $2\Delta_0$ . In this section, we test this hypothesis by computing the DC current (5.42) for a bias  $eV$  sweep. Figure 36 shows the  $I, V$  curves for various transparencies  $D$ . As indicated by the dashed lines, we see the current has steps at values of  $2\Delta_0/n$  for  $n = 1, 2, 3$ . Moreover, the higher-order ( $n > 2$ ) steps are visible too. Thus the  $I, V$  curves for a Fermi surface mismatch tunnel barrier

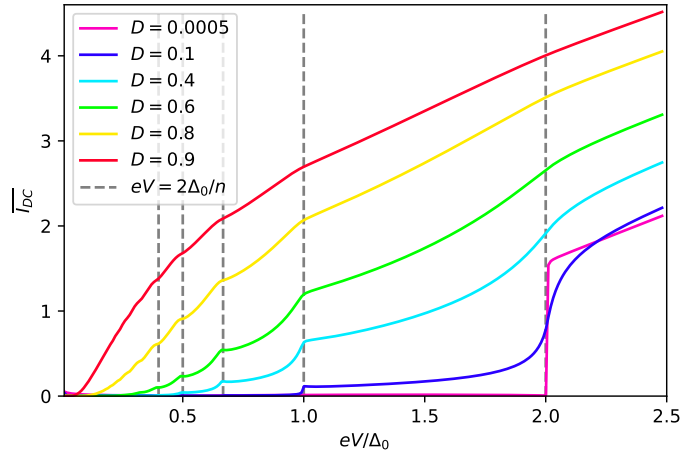


Figure 36: The MAR  $I, V$  spectra, normalized by  $G_0 = \frac{2e^2}{h}$  and tunnel barrier's transparency  $D$ , for a system consisting of a Fermi surface mismatch tunnel barrier. The dashed lines highlight the voltages  $eV = 2\Delta_0/n, n \in \mathbb{N}$  for a few values of  $n$ . Various curves are drawn for different values of  $D$ . Here  $F = 1$  for all parameters values.

are as predicted, trivial. This serves as a strong indication of the absence of any exotic structure at zero energy in a topological superconducting junction consisting of a Fermi surface mismatch tunnel barrier.

To discuss the effect of the transparency  $D$ , we note that the lower the transparency the harder it is for charge carriers to pass through the tunnel barrier. So in general the overall current is suppressed for smaller values of  $D$ , as can be observed in figure 36. Due to the MAR charge carriers can gain high energies when traversing the field increasing the tunnelling probability thus creating resonances in the current. So even for low transparencies the steps in current still occur at resonance biases. The effect is the steps become more apparent for a lower transparency due to the suppressed background. For sufficiently small transparencies, we see vertical steps for increasing bias when the continuum level on one side aligns with an integer submultiple of  $2\Delta_0$ . The reason for the formation of the steps is that charge carriers start to flow when the energy levels (or integer multiples of that) align for the first time and continue to get replenished through the leads. For a subsequent increasing bias, the current will not increase until a new energy level aligns and a new channel for conduction is opened up.

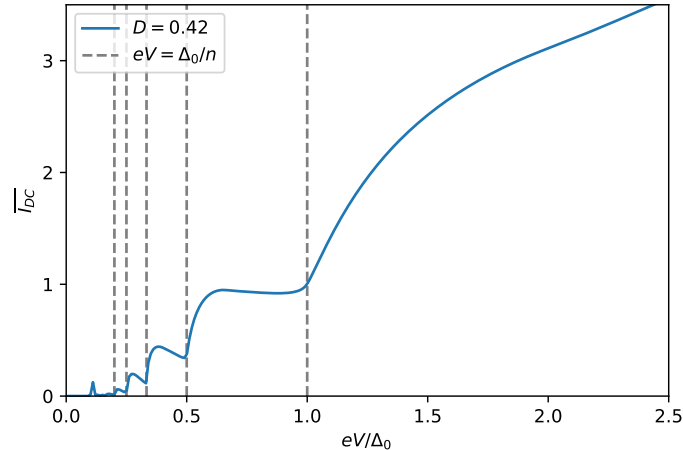


Figure 37: The MAR  $I, V$  spectrum, normalized by  $G_0 = \frac{2e^2}{h}$  and the tunnel barrier's transparency  $D$ , for a system with a magnetic tunnel barrier in the 1D ( $\theta = 0$ ) limit for  $D = 0.42$ . The dashed lines highlight the biases  $eV = \Delta_0/n$  for  $n = 1, 2, 3, 4$ . In the 1D limit  $F = -1$  for all parameters.

### 5.3.5 Magnetic tunnel barrier spectra

The existence of CMMs in the form of ABS in a MTI-TI-STI system in section 5.1.3 together with the computed factor  $F_{MTI}^{(2)}$  in figure 35a allows us to predict that a topological Josephson junction consisting of a magnetic tunnel barrier should show a non-trivial  $I, V$  spectrum. Figure 37 shows the  $I, V$  spectrum for a 1D magnetic tunnel barrier and figures 38 and 40 show the 2D case. By comparing the MTI spectra to the Fermi surface mismatch case in figure 36 it is immediately clear that the MTI tunnel barrier junction displays of a much richer DOS structure resulting in various peaks and steps in the current that were previously absent. We focus on three aspects in the  $I, V$  spectra. First we discuss the 1D ( $\theta = 0$ ) case in the figure 37, then we discuss the features in a single (asymmetry)  $I, V$  curves for a nonzero  $\theta$  in figure 38, and finally relate the features in the 2D spectra in figure 40 to the Andreev bound state energies of the two isolated STI-TI-STI and MTI-TI-STI systems.

#### 1D MTI tunnel barrier

We first consider the 1D magnetic tunnel barrier MAR results shown in figure 37. As illustrated by the dashed lines, the steps occur at integer submultiples

of  $\Delta_0$ . This result is in line with the observed existence of an ABS in the MTI-TI-STI system at  $E = 0$  in the 1D limit for all values of the magnetic energy gap  $m_z$  in figure 26, as well as with the prediction on the existence of an ABS in the sub-system formulated in section 5.1.4 for  $F_{MTI}^{(2)} = -1$ . This result was also found by Badiane, Houzet, and Meyer [41]. We have now observed that for both limiting cases  $F = \pm 1$  for the FSM tunnel barrier and the 1D MTI tunnel barrier the feature in the  $I, V$  spectra are as we predicted.

## 2D MTI tunnel barrier

The 2D magnetic tunnel barrier topological Josephson junction allows for the study of the intermediate regime between the  $F_{MTI} = 1$  and  $F_{MTI} = -1$  cases. This 2D regime has never been modelled in this much detail before. Recall that for a fixed ratio  $\mu/m_z$  we get a horizontal cross-section in figure 35a along which the real part of  $F_{MTI}$  transitions smoothly from the limiting values 1 to -1 and back to 1 again by varying  $\theta$  from  $-\pi/2$  to  $\pi/2$ . Hence we predicted a smooth transition from the  $2\Delta_0/n$  to the  $\Delta_0/n$ , for  $n \in \mathbb{N}$ , resonance features in the  $I, V$  curves.

We first consider a single  $I, V$  curve in figure 38 for a finite  $\theta$  with a corresponding non-trivial  $F$ , and describe its main features before studying the overall behaviour for a changing  $\theta$  and thus  $F_{MTI}$ . It shows the absolute current as a function of the (negative) applied bias voltage. The figure drawn is for  $\Re(F_{MTI}) = 0.3$ , a positive  $\theta$  with corresponding bound state energy of  $E_{ABS} = -0.8\Delta_0$ . Right away it is clear that an intermediate complex value of  $F_{MTI}$  gives rise to a much richer MAR spectrum than the limiting cases. For instance, the  $I, V$  becomes asymmetric in the voltage and shows steps and peaks at locations different from integer submultiples of  $(2)\Delta_0$ . The dashed green and red lines indicate biases of interest.

First of all we observe a shift in the current steps initially at biases of  $(2)\Delta_0/n, n \in \mathbb{N}$ . In fact we can relate this shift to the energy of the Andreev bound state of the (right) isolated MTI-TI-STI system computed shown in figure 26. The steps occur at biases of

$$eV = \frac{\Delta_0 + |E_{ABS}|}{n}, n \in \mathbb{N}, \quad (5.43)$$

as indicated by the green dashed lines at biases of  $|eV| = 1.8\Delta_0$  and  $|eV| = 0.9\Delta_0$ . Peaks rather than steps are present in the spectrum for a biases indicated by the red dashed line at. Again these broad peaks can be related

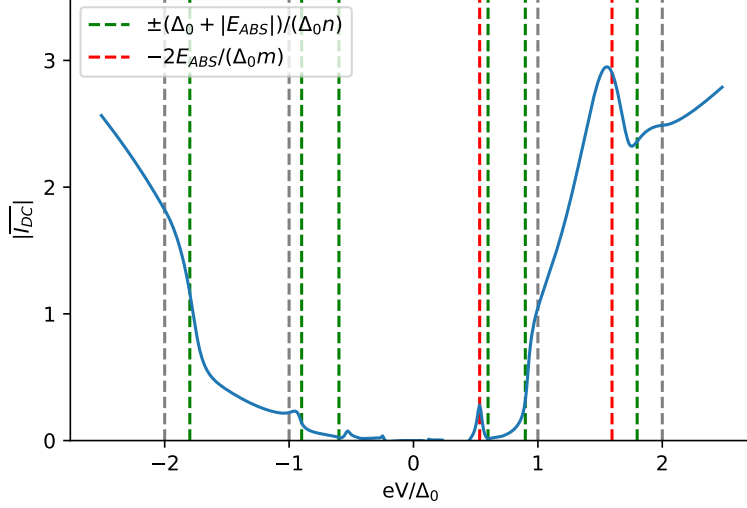


Figure 38: A figure showing the asymmetric MAR  $I, V$  spectrum, normalized by  $G_0 = \frac{2e^2}{h}$  and the tunnel barrier's transparency  $D$ , for a topological Josephson junction consisting of a magnetic tunnel barrier in 2D. The absolute current is drawn, but the left hand side of the spectrum would have been negative. The drawn curve is drawn for a fixed positive angle with the corresponding negative bound state energy of  $E_{ABS} = -0.8\Delta_0$  from figure 26, here  $\Re(F_{MTI}) = 0.3$ . The dashed lines ( $n = 1, 2, m = 1, 3$ ) highlight bias voltages of interest. The parameters corresponding to the  $F_{MTI}$  values used here are,  $\mu_m = 0$ ,  $m_z = 800\Delta_0$ ,  $\mu = \mu_s = 240\Delta_0$ ,  $\theta = 0.4\pi$ , and the width of the barrier is  $b = \hbar v_f/m_z$ .

to the bound state energy

$$eV = \frac{-2E_{ABS}}{m}, \quad \text{for positive odd } m. \quad (5.44)$$

Consider e.g. the two peaks at  $eV = 1.6\Delta_0$  and  $eV = 0.53\Delta_0$ . It should be noted that the  $-2E_{ABS}$  peaks are best fitted by (5.44) for sufficiently small transparencies. The reason for only odd  $m$  in (5.44) is due to the asymmetry of the opposing energy levels, this will be discussed momentarily.

The observed asymmetry and the location of the peaks (5.43), and (5.44) in the Josephson junction's MAR spectra are best explained by considering the bound state energies on either side of the junction for varying biases shown in figure 39. The asymmetric bound state energies for the STI-TI-MTI (dashed curve) and the MTI-TI-STI system (solid curve) in figure 39a are drawn for a fixed positive (negative)  $\theta$  by a red (blue) structure in the density of states in the Josephson junction (figure 39b). Due to this asymmetry applying a negative bias (figure 39c-e) is different from applying a positive

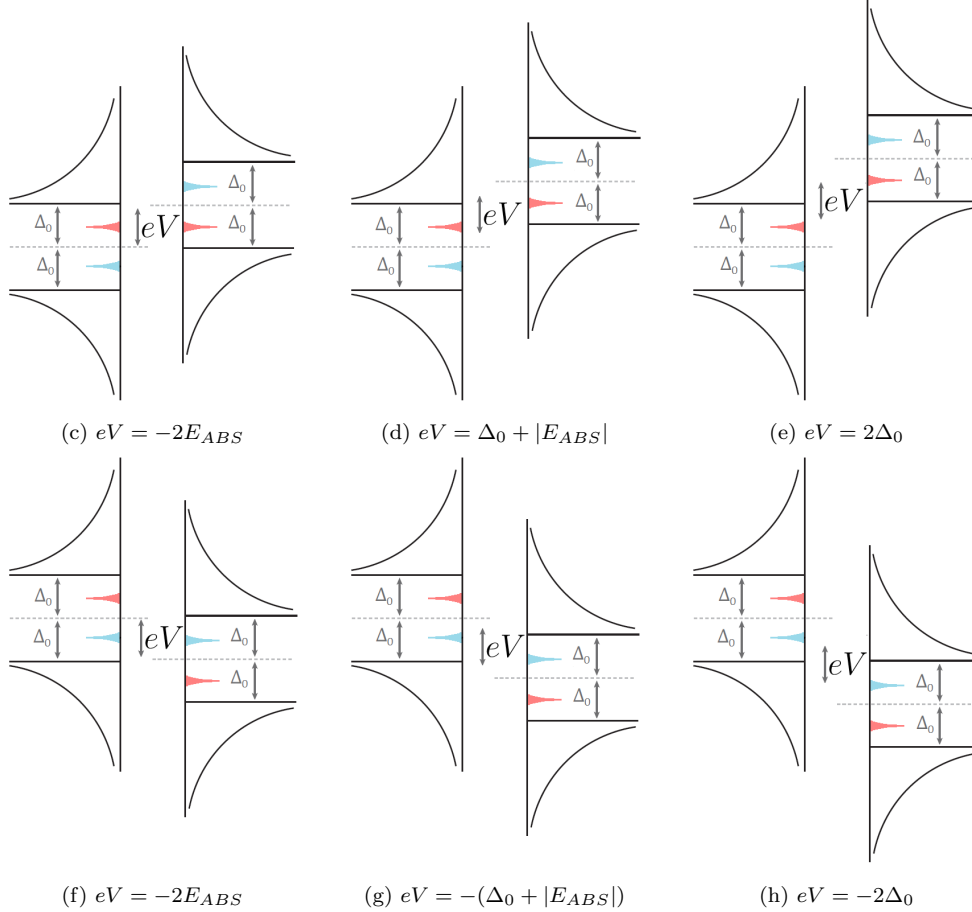
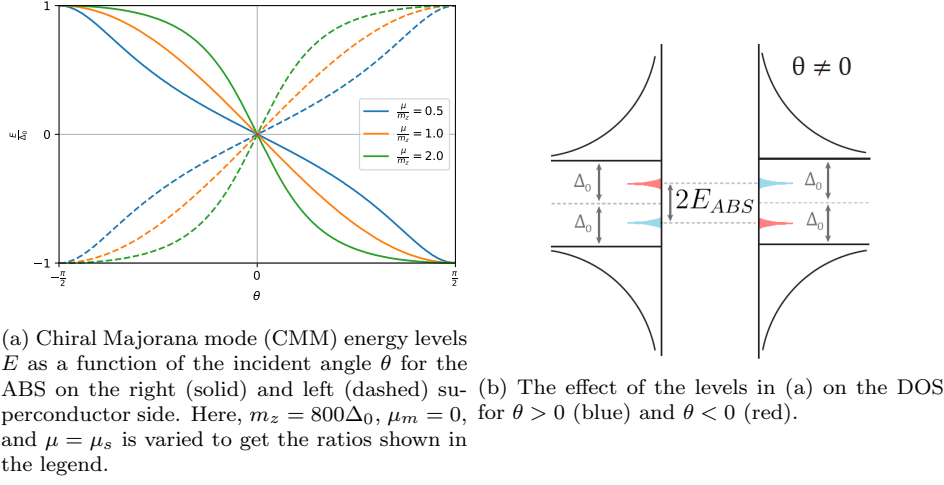


Figure 39: (a) The the Andreev bound state energy levels of CMM for  $\theta \neq 0$  in an isolated STI-TI-MTI (MTI-TI-STI) system are drawn as dashed (solid) lines on the left. (b) The density of states on the superconducting sides in the full STI-TI-MTI-TI-STI Josephson junction obtained by connecting the two isolated STI-TI-MTI and MTI-TI-STI systems. The red states correspond to a positive incidence angle. A positive bias (c-e) results in the alignment of different levels (and subsequent higher order MAR resonances) than a negative bias (f-h).

bias (figure 39f-h). By applying a voltage bias over the levels illustrated in figure 39b we identify the biases at which empty and occupied levels align and hence MAR features occur in the  $I, V$  spectra. Note that for integer sub-multiples of these biases peaks and steps are already observed due to MAR.

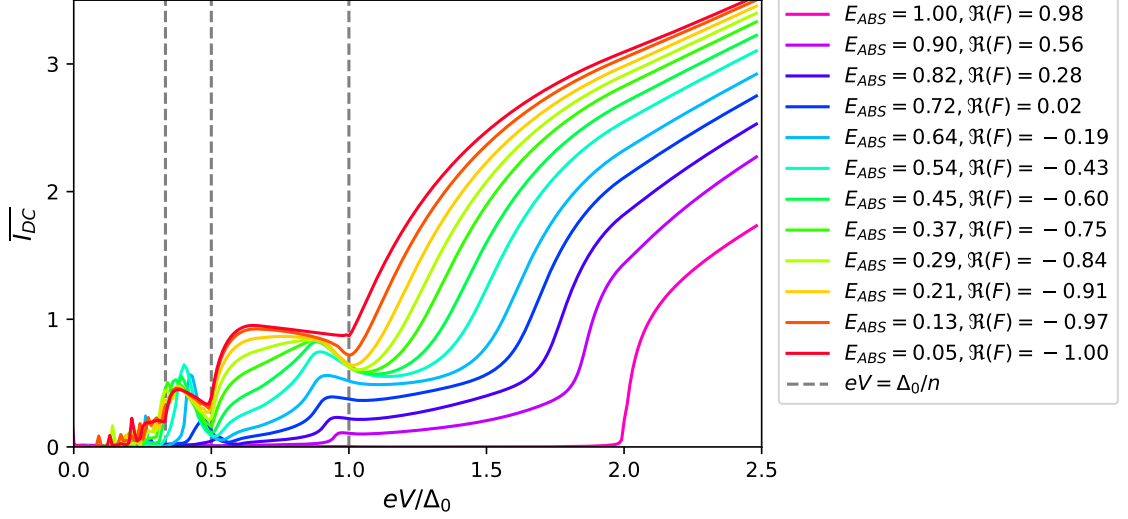
Consider the red structure in figure 39 present for a negative incidence angle, then for positive biases we get the consecutive alignment of empty and occupied levels biases of  $eV = -2E_{ABS}$  (c),  $eV = \Delta_0 + |E_{ABS}|$  (d), and  $eV = 2\Delta_0$  (e). These aligned levels (with corresponding integer submultiple modes) explain the structure observed in figure 38 for a positive voltage bias. For negative voltage biases, the aligned levels are different, because now the blue levels align rather than the red levels. This together with the fact that we only have the red or the blue structure of a given value of  $\theta$  gives rise to the asymmetry in the MAR spectra. We now come back to the reason for the odd  $m$  in (5.44). Consider a charge carrier in the left blue peak in the density of states in figure 39b, by traversing the electric field (and gaining energy along the way), the charge carrier's energy level may align with the opposing blue level after an even number of Andreev reflections. For an odd number of reflections, the initial charge carrier arrives back at the left side but, because of the asymmetry of these energy levels, there is no empty state to scatter to on this side. The fact that only an even number of Andreev reflections are admissible means that the charge carrier has gained an odd multiple of  $eV$  in energy, explaining the odd  $m$  in (5.44).

## 2D MTI tunnel barrier transition

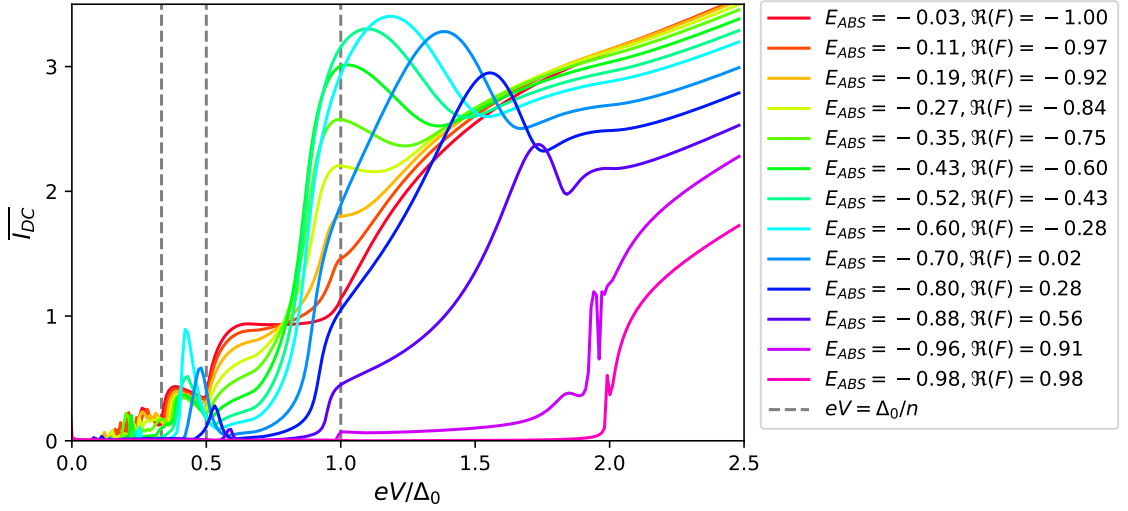
Now we study the effect of varying  $\Re(F_{MTI})$  by plotting the  $I, V$  curves for a horizontal cross section in figure 35a. For such a cross section we draw the curves shown in figures 40a and 40b. The former shows the MAR spectra for negative  $\theta$  and the latter for positive  $\theta$ . The purple line for  $E_{ABS} = 1$  in 40a and  $\Re(F) = 0.98$  is the  $I, V$  curve for a (negative) almost vertical incidence angle. We see that for this parameter choice that we get a pronounced resonance step at (almost)  $2\Delta_0$ . This case is similar to the FSM results for  $F = 1$  in figure 36. As we increase  $\theta$  we decrease  $\Re(F)$  gradually towards the red curve for  $E_{ABS} = 0.05$  and  $\Re(F) = -1$ . The red curve is (almost) identical to the 1D MTI limit shown in figure 37. In fact in the legend in figure 40a we see that for  $\Re(F) \approx 1$  we have that  $E_{ABS} \approx \Delta_0$  this transitions to  $\Re(F) \approx -1$  and  $E_{ABS} \approx 0$ . In all the intermediate curves  $|E_{ABS}|$  transitions from  $\Delta$  to 0 as  $\Re(F) = 1 \rightarrow -1$ , so c.q. (5.43) the locations of the biases shifts from integer sub-multiples of  $2\Delta_0$  to those of  $\Delta_0$ .

Similar to figure 40a, figure 40b shows the  $I, V$  spectra for positive incidence angles with corresponding negative bound state energies. The latter figure might be less clean than the former, but it is certainly not less exciting. We first consider the limiting behavior for the purple (red) curve for  $E_{ABS}/\Delta_0 \approx -1(0)$  and  $\Re(F) = 1(-1)$ . The purple curve shows the characteristic  $2\Delta_0/n, n \in \mathbb{N}$  steps we observed for the FSM tunnel barrier ( $F=1$ ). Similar to the 1D magnetic tunnel barrier limit ( $F = -1$ ), the red curve displays steps at biases of integer submultiples of  $\Delta_0$ . As well as for negative incidence angles, figure 40b shows the transition from these two limiting regimes for varying  $\theta$ . The striking difference between the two figures is that for positive incidence angles in figure 40b we see pronounced broad peaks in the spectrum, which are absent in figure 40a. The broad peaks occur at biases following 5.44, consider e.g. the two peaks in the dark blue curve at  $\frac{eV}{\Delta_0} = \frac{2 \times 0.8}{1} = 1.6$  and  $\frac{eV}{\Delta_0} = \frac{2 \times 0.8}{3} = 0.53$ .

Experimentally we observe angle averaged conduction rather than the shown  $I, V$  curves per single  $\theta$  value observed asymmetry in figure 40, so we now consider the angle average in figure 41. The asymmetry in  $I, V$  curves for single  $\theta$  values is lost when we take the angle averaged current ( $\int \overline{I_{DC}}(\theta) \cos \theta d\theta$ ) as can be seen in the green solid curve in figure 41. When we compute the angle average over either only positive or negative angles we retrieve the asymmetry as can be observed in the dashed blue and orange curve.



(a)  $\theta < 0$



(b)  $\theta > 0$

Figure 40: The MAR  $I, V$  curves, normalized by  $G_0 = \frac{2e^2}{h}$  and the tunnel barrier's transparency  $D$ , for a topological Josephson junction consisting of a magnetic tunnel barrier. The label  $E_{ABS}$  indicates the energy (relative to  $\Delta_0$ ) of the Andreev bound state in the right (MTI-TI-STI) sub-system in the figure 30 and the label  $\Re(F)$  is the real part of the ratio shown in figure (35). (a) shows the  $I, V$  curves for  $\theta < 0$  where the bound state energies obtained for the 'right' isolated MTI-TI-STI system are positive. (b) shows the  $I, V$  curves for  $\theta > 0$  corresponding to negative bound state energies. Together the  $I, V$  in (a) and (b) correspond to horizontal sweep across figure 35 for  $\theta$  from  $-\pi/2$  to  $\pi/2$ . Here,  $m_z = 800\Delta_0$ ,  $\mu_m = 0$ ,  $\mu = \mu_m = 240\Delta_0$ , the width of the barrier is  $b = \hbar v_f / m_z$ .

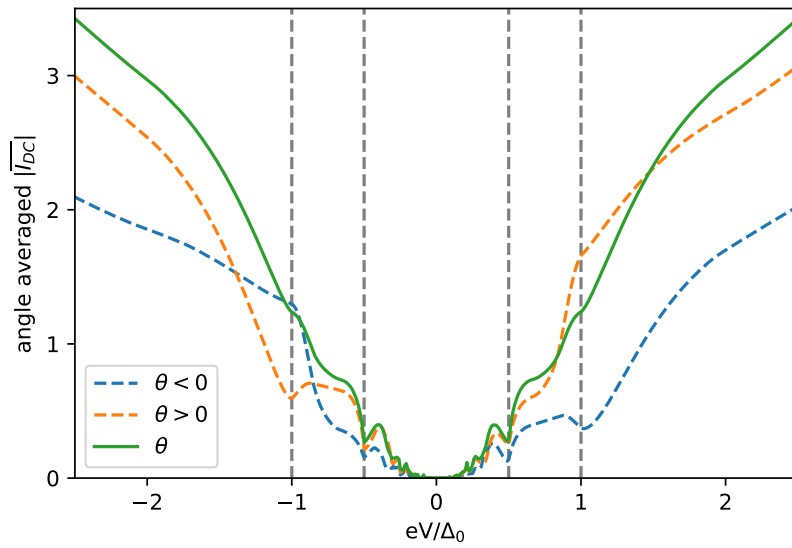


Figure 41: A figure showing the angle average over the normalized (by  $G_0 = \frac{2e^2}{h}$  and the transparency  $D$ )  $I, V$  curves in figure 40. The three curves shown are the angle averaged absolute current over negative angles ( $\theta < 0$ ), positive angles ( $\theta > 0$ ), and over all angles ( $\theta$ ) as a function of the applied voltage bias  $eV$ .

## 6 Concluding remarks and outlook

Fu and Kane's prediction [1] on the existence of chiral Majorana modes as Andreev bound states at the interface of a superconducting topological insulator to a magnetic topological insulator could form an important approach to the realization of the fault tolerant topological quantum computer[2]. Experimental confirmation of Majorana zero modes emerging in condensed matter physics has not been established, so the importance of further theoretical analysis of quantum systems potentially hosting such Majorana states is evident both from a fundamental perspective as well as in relation to multiple applications. In light of these applications we modelled the quantum transport in systems consisting of magnetic- and superconducting topological insulators. By constructing a tool that automates all the computation in the route from finding the plane-wave eigensolutions to the Bogoliubov-de Gennes equations to solving the scattering problems occurring at the interfaces between magnetic- and superconducting topological insulators the effect of Andreev bound states on the charge transport was investigated. In doing so we re-derived various results in literature and made several novel predictions.

To gain confidence in the automated derivations and analysis, the tool is validated by the (re)derivation of

- the BdG spinors equivalent to [47].
- the reflection coefficient in a 2D Fermi surface tunnel barrier equal to the one found by [46], [62] and [95].
- the reflection coefficient and related transmission in a 1D magnetic tunnel barrier [41].
- the angle and energy dependence of the chiral Majorana modes in a MTI-STI bi-layer, and the controllability of their chirality by inverting the magnetisation in the MTI [38].
- the characteristics of 1D MAR  $I, V$  curves for a magnetic topological Josephson junction [45].

Furthermore, the tool enabled the formulation of a novel mechanism to invert the chirality of Majorana modes in a MTI-STI bi-layer by controlling the ratio of the chemical potentials in the MTI and TI. This inversion is a unique signature of chiral Majorana modes in a spinful topological superconductor and it could actually be detected in a transport experiment [39]. The in this

work proposed mechanism for the inversion of the Majorana mode's chirality allows for further study.

By combining the (adapted) recurrence relations with the input provided by the custom made tool, we were able to study the topological Josephson junction consisting of a magnetic tunnel barrier in the 2D regime, which was not done before. Beyond the verification of the 1D limit by Badiane et al. [41], we established the connection between the occurrence of steps and resonance peaks in the multiple Andreev reflection spectra and the Andreev bound state energies of the constituent STI-TI-MTI and MTI-TI-STI systems. It was shown that by varying the angle of incidence the MAR spectra undergo a smooth transition according to the predicted relation

$$eV = \frac{\Delta_0 + |E_{ABS}|}{n}, n \in \mathbb{N}. \quad (6.1)$$

Here the bound state energy  $E_{ABS}$  varies from 0 to  $\pm 1$ , and consequently the MAR spectra transitions from steps at biases of  $2\Delta_0/n$  to  $\Delta_0/n$ . These two limiting cases correspond to the absence and presence of a zero energy structure in the density of states respectively. Moreover, we predicted an asymmetry in the MAR spectra per fixed  $\theta$  giving rise to the peaks in the DC current at voltage biases of  $eV = 2E_{ABS}$ .

The MAR results for a topological Josephson junction translate the non-topological junctions case too. In fact, when we consider a superconductor-ferromagnetic insulator-superconductor (SFS) junction, zero-energy bound states will form when a spin active barrier is considered [100]. That is, the barrier acts differently on opposite spin orientations, introducing a mixing term between the spin branches. In a topological junction, topology introduces this spin mixing. The results obtained in this thesis suggest a number of follow-up research directions. We finalize the discussion by giving recommendations for future research.

## Superconducting phase effects

The biggest point of discussion following from the results shown is the reconciliation of the MAR results with the theoretical prediction by Badiane et al. [45]. There it was shown that for a 1D topological Josephson junction consisting of a magnetic tunnel barrier, as shown in figure 3, the bound state energy scales with the square root of the transparency  $D$  of the tunnel barrier

$$E(\varphi) = \sqrt{D} \cos \frac{\varphi}{2}. \quad (6.2)$$

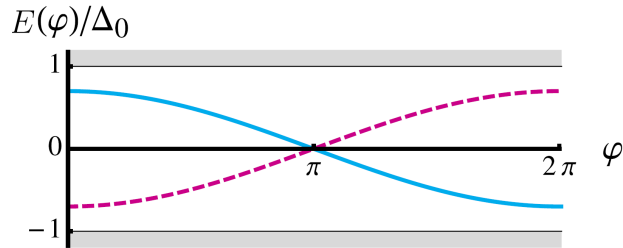


Figure 42: Dependence of the energy spectrum on the superconducting phase difference  $\varphi$ , including the continuum of states above the gap (gray) and a filled (solid line) or empty (dashed line) Andreev bound state, in a topological Josephson junction with transparency  $D = 0.7$ . Note that there is a level crossing at  $\varphi = \pi$ . This figure is an adaptation from [45].

Note that this effect works on top of the bound state energies derived for the CMM in section 5.1. That is, when we consider the full Josephson junction, the CMM bound state energies become delocalized and would be modulated additionally by this effect when the sub-systems are coupled.

The bound state's predicted  $4\pi$  periodicity (period of  $\cos \phi/2$ ) in the phase difference over the superconducting leads is well established [30]. The proportionality to  $\sqrt{D}$  can quite easily be derived and motivated qualitatively. The resulting bound state energy is shown in figure 42. Note that, for a vanishing phase difference, the bound state energies in the coupled Josephson junction go to  $\pm\sqrt{D}\Delta_0$  rather than  $\pm\Delta_0$ . For a finite phase difference of  $\varphi = \pi$  the gap closes. As shown by the authors no avoided level crossing<sup>19</sup> takes place at the crossing of the two bound state energies at  $\varphi = \pi$ . This  $\sqrt{D}$  scaling does not contradict the limiting behaviour for the CMM bound state energy in the isolated MTI-TI-STI (or MTI-TI-STI) systems shown in figure 26, because there we do not consider two superconducting leads thus no superconducting phases enter the discussion. The expected  $\sqrt{D}$  scaling behavior could, however, show up as a modulation of the peaks in the MAR  $I, V$  spectra for the full Josephson junction.

Physically it makes sense that when we connect the two isolated STI-TI-MTI and MTI-TI-STI systems to form the magnetic topological Josephson junction, the previously isolated CMM bound states become coupled through

<sup>19</sup>Avoided level crossing is the phenomenon that, e.g. two, energy levels at different energies in a quantum system generally do not cross when their levels are moved past each other under influence of some changing parameter. Please see [101] for a layman introduction.

the tunnel barrier. Effectively, the observed bound state energies in the isolated sub-systems become delocalized, resulting in a shift in their energy levels. This behavior is not recovered in the spectra in figure 37, 38, or 40. In their paper [45] the authors also do not recover this effect in the 1D magnetic tunnel barrier MAR  $I, V$  spectra. The expectation is that the bound state energies remain localized for a sufficiently small transparency. This can be seen by the fact that for a small  $D$ , the delocalization (shift away from zero) of the bound state energies in (6.2) is small, since for  $D$  well below 1, the square root behaviour brings the gap size down even more. Therefore, in this range the effect of the  $\sqrt{D}$  gap opening (6.2) would only result in a minute change in the location of the peaks in the  $I, V$  spectra. For now, this brief discussion bounds the validity of the 2D MAR results shown in this work to the small  $D$  regime.

An alternative approach to derive the recurrence relations might allow for the observation of the  $\sqrt{D}$  effect. To greatly reduce the complexity of the derivation of the recurrence relations we choose the Andreev reflections (in basis 2) such that they were equal for both electrons and holes at either side of the junction for any angle. In appendix C.2 we gathered all possible Andreev reflections. In basis 2 the superconducting phase difference only disappears for  $\varphi = 0$ . This means that the derived recurrence relations are for  $\varphi = 0$ , which would result in the  $\sqrt{D}$  scaling of the bound states seen in (6.2) and figure 42.

For further research we propose to re-derive the recurrence relations not under the condition that all Andreev reflections are identical for electrons and holes for all angles and a superconducting phase of  $\varphi = 0$ . By allowing for a complex phase difference between the Andreev reflections in the derivation of the recurrence relations we could capture the superconducting phase effects that would give rise to the predicted behavior in (6.2) [45]. In fact, these generalized recurrence relations might even shed light on the additional open question whether avoided level crossing occurs between the left and right CMM bound states, shown in figure 30, when we couple them in the Josephson junction. The question is whether the bound state energies left and right are sufficiently coupled through the magnetic tunnel barrier to undergo avoided level crossing as the angle of incidence  $\theta$  is varied. Avoided level crossing would result in a slight local dip of certain resonances peaks, this was however not observed in the MAR  $I, V$  spectra. Further study is encouraged.

## Experimental effects

The virtue of doing theoretical rather than experimental work is that we can (for the time being) neglect certain inconvenient effects, as is best illustrated by the fact that in this work we take the linear dispersion in a topological insulator for granted where colleagues [66] go to painstaking lengths to show the linear bands in figure 18. But various convenient simplifications need to be abandoned, when we want to compare a model to experiments. In that case, we have to also discuss various physical effects not (yet) taken into consideration in this work. Consider for instance the effect of the interference of the bulk bands with the surface states observed in topological insulators [44]. We however assumed perfect clean surface states in our 3D topological insulators. This interference clouds the adequate detection of characteristics of Majorana modes, theoretical work has been done to model these effects [102].

Additional effects that would appear in an experimental determination of the shown  $I, V$  curves would be the broadening of the bandwidth of the various resonance peaks (due to dissipation), and the occurrence of other resonance effects. The width of  $2E_{ABS}$  peaks in the 2D MAR curves, or the width of the TI-MTI-TI-STI transmission result in figure 29 can be studied further, e.g. similar to [103]. Moreover, tunnel resonances occur when the width of the TI sections or of the barrier are of order[62]

$$k_x L = n\pi, n \in \mathbb{N}, \quad (6.3)$$

where  $L$  is the width of the section, and  $k_x$  is the (plane wave) momentum. Then the electron waves interfere constructively and transmission resonances will occur analogously to Fabry-Pérot interference in optical waves [104]. The broadening of the bandwidth and the emergence of other resonances reduce the visibility of the predicted peaks and steps shown in this study. We therefore propose to further study and model them.

In conclusion, the re-derived results from literature in this work reflect the validity of the constructed tool and its application, but more importantly the new results and their discussion form a basis for further study. In light of the mentioned experimental significance in the search for CMM, the proposed mechanism controlling the chirality of the Majorana modes should be studied in more detail. Furthermore, the novel 2D magnetic tunnel barrier MAR  $I, V$  curves uncovered the intimate relationship between the CMM bound state energies in isolated STI-MTI bilayers and current resonances in  $I, V$  curves for a magnetic topological Josephson junction. To bridge the gap to experimental data we propose to on the one hand extend the analysis by con-

sidering a multitude of physical effects that would refine the model to better match a realistic experiment, and on the other hand re-derive the recurrence relations in full generality to study the effect of the superconducting phase difference.

## Acknowledgements

In yet another year dominated by a not to be mentioned virus, I have worked mostly online on a year-long project under the great supervision of Alexander Brinkman and Bernard Geurts. Their guidance was different but complementary. In many discussions with Alexander the focus was on the physical details, whereas Bernard, because of his distance to the underlying physics, was a great mentor in scientific writing and keeping track of the overall scope of the project. I've had an uncountable number of discussions, with both of them, on whether various minus signs in spinors or coefficients should be plus signs and vice-versa, but at the end of the discussion Bernard's conclusion was the same: "just automate the computational steps". Ironically, this remark actually lead me to build the tool that formed the backbone of this thesis.

It was refreshing to see Bernard's and Alexander's excitement about and commitment to this project, this, in part, has led me to pursue a further career in academia. I would like to express my appreciation for the positive and friendly atmosphere I experienced in both the MMS and ICE/QTM research groups, in the somewhat limited, number of live meetings I've had during my stay there. Lastly, I would like to thank Linde Olde Olthof for the pleasant and fruitful collaboration on the recurrence relations, I hope we can continue our combined work and finalize our combined efforts.

## A Spinors basis 2

In the following sections we will solve the Hamiltonian derived from the Bogoliubov-de Gennes equations in a plane wave basis for the three mentioned materials, TI, MTI and STI using basis 2. The BdG equations in represented in matrix form in basis 2 is given in (3.50). Note that here, we will derive the eigenfunctions in case of a right moving (quasi)particle. This results in a sign difference between the electron- and hole-like quasiparticles in the wavevector in the exponential for the plane wave term. We consider the following basis (so-called basis 2). The two bases are related by

$$\phi_2 = \text{diag} [\hat{\sigma}_0, i\hat{\sigma}_y] \phi_1. \quad (\text{A.1})$$

As described in section 3.3 the electron spinors for an TI and MTI are the same in basis 1 and 2. We therefore only describe the TI and MTI hole spinors and the STI spinors in basis 2 here.

### A.1 Topological insulator

Consider the  $2 \times 2$  lower right hole block in (3.50). In absence of induced superconductivity and ferromagnetism the 2D topological states are described by the eigenproblem

$$\begin{pmatrix} \mu & -\hbar k_h v_f e^{-i\theta} \\ -\hbar k_h v_f e^{i\theta} & \mu \end{pmatrix} \begin{pmatrix} v_{0\downarrow} \\ -v_{0\uparrow} \end{pmatrix} = E \begin{pmatrix} v_{0\downarrow} \\ -v_{0\uparrow} \end{pmatrix}, \quad (\text{A.2})$$

with eigensolutions

$$E_{h\mp}^{TI} = \mp \hbar k_h v_f + \mu \leftrightarrow \phi_{h\mp}^{TI}(x, y) = \frac{1}{\sqrt{2}} \begin{pmatrix} 1 \\ \pm e^{i\theta} \end{pmatrix} e^{-ik_x x - ik_y y}, \quad (\text{A.3})$$

where  $k_h = |E - \mu|/(\hbar v_f)$ . The  $\pm$  in the spinors and energy relations refers to the sign in front of the  $k$  term. We see that we retrieve the same dispersion relations. The explanation per branch (label) is elaborated upon in section 3.2.4.

### A.2 Magnetic topological insulator

Now we consider the above with a nonzero magnetic field orientated perpendicular to the two dimensional surface, i.e.  $\mathbf{m} = (0, 0, m_z)^T$ . The effect of the magnetisation is explained in section 3.2. In basis 2 the MTI eigenproblems

for both an increasing or decreasing evanescent ( $\mp q_e$ ) wave are given by

$$\begin{pmatrix} m_z + \mu_m & \hbar v_f (ik_h \sin(\theta) \mp q_h) \\ \hbar v_f (-ik_h \sin(\theta) \mp q_h) & -m_z + \mu_m \end{pmatrix} \begin{pmatrix} v_{0\downarrow} \\ -v_{0\uparrow} \end{pmatrix} = E \begin{pmatrix} v_{0\downarrow} \\ -v_{0\uparrow} \end{pmatrix}. \quad (\text{A.4})$$

This problem has two energy eigensolutions with corresponding eigenvectors

$$E_{h\pm}^{MTI} = \mu_m \pm \sqrt{m_z^2 + \hbar^2 k_h^2 v_f^2 \sin^2(\theta) + \hbar^2 q_h^2 v_f^2} \\ \leftrightarrow \phi_h^{MTI,\pm}(x, y) = \frac{1}{\sqrt{A_{h\pm}}} \begin{pmatrix} -i\hbar k_h v_f \sin(\theta) \pm \hbar q_h v_f \\ -E + m_z + \mu_m \end{pmatrix} e^{\mp i q_h x - i k_y y}, \quad (\text{A.5})$$

where  $A_{h\pm}$  is used for normalization. We solve for  $q_h$  in the dispersion relation

$$q_h = \pm \frac{\sqrt{-m_z^2 - (\hbar v_f k_h \sin \theta)^2 + (E - \mu_m)^2}}{\hbar v_f}, \quad (\text{A.6})$$

again the same sign convention for  $\phi_h^{MTI\pm}(x, y)$  as for basis 1 in section 3.2 will be used.

### A.3 Superconducting topological insulator

Next we consider a topological insulator in close contact with a s-wave superconductor. For a s-wave superconductor, the energy gap becomes a real valued constant. The gap couples the electron- and hole-like components in the Hamiltonian matrix, so for the STI need to solve the entire matrix eigenproblem

$$\begin{pmatrix} -\mu_s & \hbar k v_f e^{-i\theta_s} & \Delta_0 e^{i\varphi} & 0 \\ \hbar k v_f e^{i\theta_s} & -\mu_s & 0 & -\Delta_0 e^{i\varphi} \\ \Delta_0 e^{-i\varphi} & 0 & \mu_s & \hbar k v_f e^{-i\theta_s} \\ 0 & -\Delta_0 e^{-i\varphi} & \hbar k v_f e^{i\theta_s} & \mu_s \end{pmatrix} \begin{pmatrix} u_{0\uparrow} \\ u_{0\downarrow} \\ v_{0\downarrow} \\ -v_{0\uparrow} \end{pmatrix} = E \begin{pmatrix} u_{0\uparrow} \\ u_{0\downarrow} \\ v_{0\downarrow} \\ -v_{0\uparrow} \end{pmatrix}. \quad (\text{A.7})$$

As frequently mentioned, the momenta considered in the superconducting regime are in relative distance close to  $k_f$ , hence we describe both the electron- and hole-like momenta by a single momentum  $\mathbf{k}$  with 2-norm  $k$ .  $\theta_s$  is defined as in section 3.2.

The above system can be simplified using a unitary transformation. Let's denote the matrix in (A.7) by  $\check{H}_{STI}^{(2)}$ . Consider the unitary matrix

$$\check{U}_2 = \text{diag}(U, U), \quad (\text{A.8})$$

where the unitary matrix  $U$  is given by

$$U = \frac{1}{\sqrt{2}} \begin{pmatrix} -1 & e^{-i\theta_s} \\ e^{i\theta_s} & 1 \end{pmatrix}. \quad (\text{A.9})$$

The unitary transformation gives us the eigenproblem for

$$\check{H}_{STI}^{Trans} = \check{U}_2 \check{H}_{STI}^{(2)} \check{U}_2 = \begin{pmatrix} -\hbar k v_f - \mu_s & 0 & 0 & -\Delta_0 e^{i\varphi} e^{-i\theta_s} \\ 0 & \hbar k v_f - \mu_s & -\Delta_0 e^{i\varphi} e^{i\theta_s} & 0 \\ 0 & -\Delta_0 e^{-i\varphi} e^{-i\theta_s} & -\hbar k v_f + \mu_s & 0 \\ -\Delta_0 e^{-i\varphi} e^{i\theta_s} & 0 & 0 & \hbar k v_f + \mu_s \end{pmatrix}, \quad (\text{A.10})$$

which has the four eigenvalues

$$E_{\pm\pm}^{STI} = \pm \sqrt{\Delta_0^2 + (\mu_s \pm \hbar k v_f)^2}, \quad (\text{A.11})$$

with eigenvectors,

$$\begin{aligned} & (\Delta_0 e^{i\varphi} e^{-i\theta_s} / \chi_{\pm}, 0, 0, 1)^T, \\ & (0, \Delta_0 e^{i\varphi} e^{i\theta_s} / \chi_{\pm}, 1, 0)^T, \end{aligned} \quad (\text{A.12})$$

where

$$\chi_{\pm} := E \pm \chi = E \pm \sqrt{E^2 - \Delta_0^2}. \quad (\text{A.13})$$

Suppose  $\mathbf{x}$  is an eigenvector of (A.10), then  $\check{U}_2 \mathbf{x}$  is an eigenvector of the original problem (A.7) with the same eigenvalue. We find four eigenvalues

$$\begin{aligned} E_{\pm+}^{STI} = \pm \sqrt{\Delta_0^2 + (\mu_s - \hbar k v_f)^2} & \leftrightarrow \phi_+^{STI, \pm}(x, y) = \frac{1}{2} \begin{pmatrix} 1 \\ e^{i\theta_s} \\ \frac{\chi_{\pm}}{\Delta_0} e^{-i\varphi} \\ -\frac{\chi_{\pm}}{\Delta_0} e^{i\theta_s} e^{-i\varphi} \end{pmatrix} e^{ik_x x + ik_y y} e^{\pm \chi x} \\ E_{\pm-}^{STI} = \pm \sqrt{\Delta_0^2 + (\mu_s + \hbar k v_f)^2} & \leftrightarrow \phi_-^{STI, \pm}(x, y) = \frac{1}{2} \begin{pmatrix} 1 \\ -e^{i\theta_s} \\ \frac{\chi_{\mp}}{\Delta_0} e^{-i\varphi} \\ \frac{\chi_{\mp}}{\Delta_0} e^{i\theta_s} e^{-i\varphi} \end{pmatrix} e^{ik_x x + ik_y y} e^{\pm \chi x}. \end{aligned} \quad (\text{A.14})$$

The  $\pm$  sign labels in the eigenvectors correspond to the increasing or decreasing nature of the wave term. The  $k_{x,y}$  term is the same as it was in the TI, but now weighted with the chemical potential in the STI,  $\mu_s$ .

## B Equivalent spinors: spin rotation

In this appendix we show the equivalence between the output of this tool to results in literature [47]. The section consists of two parts, first we establish

the equivalence up to a spin rotation (as explained in the main text) and then we rewrite the STI results to create a one to one correspondence. We only show the results for a single wavefunction per material, but the other wavefunctions follow analogously. We adopt basis 1 in this section since this is the same basis used in [47].

First we focus on the difference between the tool's output and the references output due to a spin rotation in the definition of the single particle Hamiltonian. We only consider the two dimensional spinors here, but the 4 dimensional spinors follow analogously by transforming both the 'electron' and 'hole' block in the  $4 \times 4$  BdG matrix form similarly. In section 3.2 we work in a spin basis of eigenfunction of  $\sigma_x$ , i.e.,  $\{\frac{1}{\sqrt{2}}(1, 1)^T, \frac{1}{\sqrt{2}}(1, -1)^T\}$ . In this basis the spin locking part has the form

$$\hat{h}_x = \mathbf{p} \cdot \boldsymbol{\sigma}_x = p_x \sigma_x + p_y \sigma_y. \quad (\text{B.1})$$

The basis used in [47] is, w.r.t. to  $\sigma_y$   $\{\frac{1}{\sqrt{2}}(1, i)^T, \frac{1}{\sqrt{2}}(1, -i)^T\}$ ,

$$\hat{h}_y = \mathbf{p} \cdot \boldsymbol{\sigma}_y = p_y \sigma_x - p_x \sigma_y. \quad (\text{B.2})$$

The basis vectors are related by the transformation matrix  $T$

$$T = \begin{pmatrix} 1 & 0 \\ 0 & i \end{pmatrix}. \quad (\text{B.3})$$

Hence we have  $\hat{\phi}_y = T\hat{\phi}_x$  where the hat vectors are the basis vectors in each specified spin basis. Then we can transform a coefficient vector in spin basis  $x$  to a coefficient in spin basis  $y$  using  $T$ . Since we solve for eigensolution to (B.1) and (B.2) we can derive a condition for the equivalence of the two bases as follows

$$\begin{aligned} \hat{h}_y \phi_y &= \lambda \phi_y \\ \rightarrow \hat{h}_y T \phi_x &= \lambda T \phi_x \\ \rightarrow T^{-1} \hat{h}_y T \phi_x &= \lambda \phi_x \\ \rightarrow T^{-1} \hat{h}_y T \equiv \hat{h}_x &\iff -T^{-1} \sigma_x T = \sigma_y, \quad \text{and} \quad T^{-1} \sigma_y T = \sigma_x, \end{aligned}$$

Indeed if we plug in the Pauli matrices and use

$$T^{-1} = \begin{pmatrix} 1 & 0 \\ 0 & -i \end{pmatrix},$$

the two relations are satisfied. This means that we can apply the transformation to relate the wavefunctions in either basis. By applying  $T$  on the

wavefunctions derived in section 3.2 they become identical to those in [75].

In literature two ways to represent the superconducting wavefunctions are common. One uses the  $\chi$ 's

$$\chi_{\pm} = E - \sqrt{E^2 - \Delta_0^2},$$

another is using the BCS quasiparticles weights  $u, v$  as introduced in section 2.1.2. To make the equivalence to the STI wavefunctions in [47] explicit we introduce

$$u_0 = \frac{1}{\sqrt{2E}} \sqrt{E + \sqrt{E^2 - \Delta_0^2}},$$

$$v_0 = \frac{1}{\sqrt{2E}} \sqrt{E - \sqrt{E^2 - \Delta_0^2}}.$$

To illustrate this equivalence we consider a specific STI wavefunction solution from section 3.2, i.e. the right traveling 'electron' quasiparticle wavefunction given by

$$\phi_+^{STI,+} = \frac{1}{2} \begin{pmatrix} 1 \\ e^{i\theta} \\ \frac{\chi_-}{\Delta_0} e^{i\theta} \\ \frac{\chi_-}{\Delta_0} \end{pmatrix}.$$

Where we have set the superconducting phase to zero, since this was not modelled in the referenced work. We want to show this is equivalent to (we have already corrected for the spin rotation difference discussed above)

$$\phi' = \frac{1}{2} \begin{pmatrix} u_0 \\ u_0 e^{i\theta} \\ v_0 e^{i\theta} \\ v_0 \end{pmatrix},$$

we can go from one representation to the other using the following useful relations

$$\chi_+ \chi_- = \Delta_0^2 \rightarrow \Delta_0 = \sqrt{\chi_+} \sqrt{\chi_-}$$

$$u_0 = \frac{1}{\sqrt{2E}} \sqrt{\chi_+}$$

$$v_0 = \frac{1}{\sqrt{2E}} \sqrt{\chi_-}.$$

We ignore normalisation for intermediate calculations and simply normalize afterwards. Moreover we can always take out any common factor in front of vector

$$\phi_+^{STI,+} \sim \begin{pmatrix} 1 \\ e^{i\theta} \\ \frac{\chi_-}{\Delta_0} e^{i\theta} \\ \frac{\chi_-}{\Delta_0} \end{pmatrix} \sim \begin{pmatrix} 1 \\ e^{i\theta} \\ \frac{\chi_-}{\sqrt{\chi_+}\sqrt{\chi_-}} e^{i\theta} \\ \frac{\chi_-}{\sqrt{\chi_+}\sqrt{\chi_-}} \end{pmatrix} \sim \begin{pmatrix} \sqrt{\chi_+} \\ \sqrt{\chi_+} e^{i\theta} \\ \sqrt{\chi_-} e^{i\theta} \\ \sqrt{\chi_-} \end{pmatrix} \sim \begin{pmatrix} u_0 \\ u_0 e^{i\theta} \\ v_0 e^{i\theta} \\ v_0 \end{pmatrix} \sim \phi'.$$

Hence the STI wavefunction are equivalent.

## C Additional calculations

In this appendix we gather various calculations similar to those given in the main text. We consider for example a mirrored system or bilayer as discussed in the main text.

### C.1 TI-MTI-TI-STI-transmission

In this appendix we give the imposed continuity requirements that give rise to the transmission results through the entire TI-MTI-STI-STI system (figure 28) shown in figure 29. The system consists of three interfaces, i.e. a TI-MTI interface at  $x = -b - d$ ; a MTI-TI interface at  $x = -d$ ; and a TI-STI interface at  $x = 0$ . We will use the coefficients as shown in figure 28 in the following three continuity requirements. At the first two interfaces we have separate equations, of dimension two, for the electrons and holes, whereas for the last interface we have a single four dimensional equation. The wavefunctions are labelled by an index ( $i$ ) to indicate a potential basis, and for basis 1 and basis 2 they are given in section 3.2 and A.

#### TI-MTI interface:

For the electron wavefunctions at  $x = -b - d$  and  $y = 0$ ,

$$\phi_{e+}^{TI,(i)}(\theta) + C_1 \phi_{e+}^{TI,(i)}(\pi - \theta) = C_3 \phi_e^{MTI,+ (i)}(\theta) + C_4 \phi_e^{MTI,- (i)}(\theta),$$

and for the holes at  $x = -b - d$

$$C_2 \phi_{h-}^{TI,(i)}(\pi + \theta) = C_5 \phi_h^{MTI,+ (i)}(\pi + \theta) + C_6 \phi_h^{MTI,- (i)}(\pi + \theta).$$

#### MTI-TI interface:

For the electron wavefunctions at  $x = -d$  and  $y = 0$

$$C_3 \phi_e^{MTI,+ (i)}(\theta) + C_4 \phi_e^{MTI,- (i)}(\theta) = C_7 \phi_{e+}^{TI,(i)}(\theta) + C_8 \phi_{e+}^{TI,(i)}(\pi - \theta),$$

similarly for the holes we find

$$C_5 \phi_h^{MTI,+^{(i)}}(\pi + \theta) + C_6 \phi_h^{MTI,-^{(i)}}(\pi + \theta) = C_9 \phi_{h-}^{TI,(i)}(\pi + \theta) + C_{10} \phi_{h-}^{TI,(i)}(-\theta).$$

### TI-STI interface:

For the TI-STI interface we have a single four dimensional spinor continuity requirement at  $x = y = 0$ . Since we use the short hand notation to display the TI hole and electron spinors in two dimensions, we should now note that actually they are four dimensional. However since the electron spinors would look like  $(\cdot, \cdot, 0, 0)^T$  and the hole ones like  $(0, 0, \cdot, \cdot)^T$ , we can easily go from the two dimensional representation to the four dimensional one by app(pre)pending the electron (hole) spinor by two zero entries. Using the extended TI wavefunctions we find

$$\begin{aligned} C_7 \phi_{e+}^{TI,(i)}(\theta) + C_8 \phi_{e+}^{TI,(i)}(\pi - \theta) + C_9 \phi_{h-}^{TI,(i)}(\pi + \theta) + C_{10} \phi_{h-}^{TI,(i)}(-\theta) \\ = C_{11} \phi_+^{STI,-^{(i)}}(\theta_s) + C_{12} \phi_-^{STI,-^{(i)}}(-\theta_s). \end{aligned}$$

We note that in these five equations, we have twelve unknowns  $C_1$  through  $C_{12}$  and we have  $2 + 2 + 2 + 2 + 4 = 12$  equations. Since the some coefficients are present in different continuity requirements, we can not solve the linear systems separately and we cast all five equations to a  $12 \times 12$  linear matrix system.

## C.2 AR coefficients

In this section we compare the AR coefficients for a STI-TI system and a TI-STI for both bases and for both an incoming electron and hole. The calculations are done completely analogously to those in section 5.1.1. We suppose a phase of  $\varphi_R$  on the right STI, i.e. the superconductor in the TI-STI bilayer, and  $\varphi_L$  on the left superconductor.

### TI-STI

The AR reflection coefficients for the TI-STI bilayer in basis 1 are

$$r_{eh}^{(1),R}(\theta) = \frac{\chi_-}{\Delta_0} g(\theta, \theta_s) e^{i\theta} e^{-i\varphi_R}, \quad (\text{C.1})$$

and

$$r_{he}^{(1),R}(-\theta) = -\frac{\chi_-}{\Delta_0} g(\theta, \theta_s) e^{i\theta} e^{i\varphi_R}. \quad (\text{C.2})$$

Where  $g(\theta, \theta_s)$  is given in (5.5). The two coefficients are related by

$$\boxed{r_{eh}^{(1),R}(\theta) = -r_{he}^{(1),R}(-\theta) e^{-2i\varphi_R}.} \quad (\text{C.3})$$

Similarly in basis 2

$$r_{eh}^{(2),R}(\theta) = \frac{\chi_-}{\Delta_0} g(\theta, \theta_s) e^{-i\varphi_R} \quad (\text{C.4})$$

and

$$r_{he}^{(2),R}(-\theta) = \frac{\chi_-}{\Delta_0} g(\theta, \theta_s) e^{i\varphi_R}. \quad (\text{C.5})$$

Hence the two are related by

$$\boxed{r_{eh}^{(2),R}(\theta) = r_{he}^{(2),R}(-\theta) e^{-2i\varphi_R}.} \quad (\text{C.6})$$

### STI-TI

The AR reflection coefficients for the STI-TI bilayer in basis 1 are

$$r_{eh}^{(1),L}(\pi - \theta) = -\frac{\chi_-}{\Delta_0} g(\theta, \theta_s) e^{-i\theta} e^{-i\varphi_L}, \quad (\text{C.7})$$

$$r_{he}^{(1),L}(\pi + \theta) = \frac{\chi_-}{\Delta_0} g(\theta, \theta_s) e^{-i\theta} e^{i\varphi_L}. \quad (\text{C.8})$$

Hence the two are related by

$$\boxed{r_{eh}^{(1),L}(\pi - \theta) = -r_{he}^{(1),L}(\pi + \theta) e^{-2i\varphi_L}.} \quad (\text{C.9})$$

The AR reflection coefficients for the STI-TI bilayer in basis 2 are

$$r_{eh}^{(2),L}(\pi - \theta) = \frac{\chi_-}{\Delta_0} g(\theta, \theta_s) e^{-i\varphi_L}, \quad (\text{C.10})$$

$$r_{he}^{(2),L}(\pi + \theta) = \frac{\chi_-}{\Delta_0} g(\theta, \theta_s) e^{i\varphi_L}, \quad (\text{C.11})$$

hence the two are related by

$$\boxed{r_{eh}^{(2),L}(\pi - \theta) = r_{he}^{(2),L}(\pi + \theta) e^{-2i\varphi_L}.} \quad (\text{C.12})$$

## Phase difference

Consider a phase difference of  $\varphi = \varphi_L - \varphi_R$  over the superconducting leads, this gives  $\varphi_R = -\varphi/2$  and  $\varphi_L = \varphi/2$ . For simplicity we set  $\frac{\chi_-}{\Delta_0}g(\theta, \theta_s) := r_{AR}$

$$\begin{aligned}
r_{eh}^{(1),R}(\theta) &= r_{AR}e^{i\varphi/2}e^{i\theta}, \\
r_{he}^{(1),R}(-\theta) &= -r_{AR}e^{-i\varphi/2}e^{i\theta}, \\
r_{eh}^{(1),L}(\pi - \theta) &= -r_{AR}e^{-i\varphi/2}e^{-i\theta}, \\
r_{he}^{(1),L}(\pi + \theta) &= r_{AR}e^{i\varphi/2}e^{-i\theta}, \\
r_{eh}^{(2),R}(\theta) &= r_{AR}e^{i\varphi/2}, \\
r_{he}^{(2),R}(-\theta) &= r_{AR}e^{-i\varphi/2}, \\
r_{eh}^{(2),L}(\pi - \theta) &= r_{AR}e^{-i\varphi/2}, \\
r_{he}^{(2),L}(\pi + \theta) &= r_{AR}e^{i\varphi/2}.
\end{aligned} \tag{C.13}$$

Now consider a Josephson junction with a phase difference of  $\varphi$  and consisting of a tunnel barrier with a transparency  $D$ . We can first consider two limits,  $D = 0, 1$ . For  $D = 0$  we have two isolated bound states on either side of the barrier. In each bound state we should compare the electron and hole reflections on the same side. When we compare for instance the right hand side  $r_{eh}^{(2),R}$  and  $r_{he}^{(2),R}$  we see that for an isolated system with an infinite thick MTI that the additional electron and hole phase gain due to a superconducting phase cancel and we retrieve the same Andreev bound states found in section 5.1.3.

For a fully transparent barrier  $D = 1$  we consider a right traveling electron and we compare the electron to hole Andreev reflection at the right STI, i.e.  $r_{eh}^{(2),R}(\theta) = r_{AR}e^{i\varphi}$ , and the hole electron Andreev reflection at the left STI,  $r_{he}^{(2),L}(\pi + \theta) = r_{AR}e^{i\varphi}$ . Since these two are equal we get an total phase of  $\varphi$  per round trip.

## D Recurrence relations for a topological tunnel junction

The recurrence relations used to compute the  $I, V$  curves in section 5.3 are derived here. An elaborate discussion of their origin is given in [46]. In the work [46] the recurrence relations are derived in the case  $F = -1$ , here we focus on the main derivation and highlight the effect of the factor  $F$  in the

case when it is not necessarily -1. The work shown is a combined effort with the original author of the mentioned work.

## D.1 Scattering matrices

We introduce the scattering matrix for electrons and holes as,

$$S_e = \begin{bmatrix} r_{ee} & t_{ee} \\ t_{ee} & S_e^{22} \end{bmatrix}, \quad S_h = \begin{bmatrix} r_{hh} & t_{hh} \\ t_{hh} & S_h^{22} \end{bmatrix}, \quad (\text{D.1})$$

where  $r_{ee}$  is the electron-electron reflection,  $t_{ee}$  the electron-electron transmission,  $r_{hh}$  the hole-hole reflection and  $t_{hh}$  the hole-hole transmission. We follow the procedure by [96] and find the the bottom-right elements  $S_e^{22}$  and  $S_h^{22}$  by normalising  $S_e$  and  $S_h$  to be a unitary matrix, i.e.  $S_e^\dagger S_e = S_h^\dagger S_h = I$ , where  $I$  is the  $2 \times 2$  identity matrix. For simplicity, we define  $r \equiv r_{ee}$  and  $t \equiv t_{ee}$ . For the electrons, we find

$$S_e^\dagger S_e = \begin{bmatrix} r^* & t^* \\ t^* & (S_e^{22})^* \end{bmatrix} \begin{bmatrix} r & t \\ t & S_e^{22} \end{bmatrix} = \begin{bmatrix} r^*r + t^*t & r^*t + t^*S_e^{22} \\ t^*r + (S_e^{22})^*t & t^*t + (S_e^{22})^*S_e^{22} \end{bmatrix} \stackrel{!}{=} \begin{bmatrix} 1 & 0 \\ 0 & 1 \end{bmatrix}. \quad (\text{D.2})$$

Probability conservation gives  $r^*r + t^*t = |r|^2 + |t|^2 = 1$ . Solving the other equations, we obtain

$$S_e = \begin{bmatrix} r & t \\ t & -\frac{r^*t}{t^*} \end{bmatrix}. \quad (\text{D.3})$$

Comparing the electrons and holes, we assume the holes pick up an extra phase  $F$  upon reflection. Without loss of generality, we write  $r_{hh} = F r_{ee}^* = F r^*$  with  $|F|^2 = 1$ . For the transmission, we use  $t_{hh} = t_{ee}^* = t^*$ . Hence,

$$S_h = \begin{bmatrix} r^* & t^* \\ t^* & S_h^{22} \end{bmatrix}. \quad (\text{D.4})$$

The unitary matrix criterion then gives

$$S_h^\dagger S_h = \begin{bmatrix} F^*r & t \\ t & (S_h^{22})^* \end{bmatrix} \begin{bmatrix} F r^* & t^* \\ t^* & S_h^{22} \end{bmatrix} = \begin{bmatrix} F r F^* r^* + t t^* & F^* r t + t S_h^{22} \\ t F r^* + (S_h^{22})^* t^* & t t^* + (S_h^{22})^* S_h^{22} \end{bmatrix} \stackrel{!}{=} \begin{bmatrix} 1 & 0 \\ 0 & 1 \end{bmatrix}. \quad (\text{D.5})$$

By solving this equation, we obtain

$$S_h = \begin{bmatrix} F r^* & t^* \\ t^* & -F^* \frac{r t^*}{t} \end{bmatrix}. \quad (\text{D.6})$$



where the subscript  $n$  indicates the amount of Andreev reflections that have occurred and  $a$  is the Andreev reflection coefficient. This acts as a brief introduction to the wavefunctions taking part in the derivation of the recurrence relations, but the reader is referred to [46] for a more elaborate explanation.

The wave amplitudes in the regions in figure 43 are related by the scattering matrices as follows

$$\begin{aligned} \begin{bmatrix} B_n \\ C_n \end{bmatrix} &= S_e \begin{bmatrix} \delta_{n0} + a_{2n}A_n \\ a_{2n+1}D_n \end{bmatrix}, & S_e &= \begin{bmatrix} r & t \\ t & -r^*t/t^* \end{bmatrix}, \\ \begin{bmatrix} A_n \\ D_{n-1} \end{bmatrix} &= S_h \begin{bmatrix} a_{2n}B_n \\ a_{2n-1}C_{n-1} \end{bmatrix}, & S_h &= \begin{bmatrix} Fr^* & t^* \\ t^* & -F^*rt^*/t \end{bmatrix}, \end{aligned}$$

where  $F$  is the extra phase picked up by the holes upon Andreev reflection. This phase is material-dependent and ranges from  $F = 1$  for a normal metal and  $F = -1$  for a topological insulator.

From these matrices, we obtain a system of equations with four unknowns  $A_n$ ,  $B_n$ ,  $C_n$  and  $D_n$ :

$$\begin{aligned} B_n &= r [\delta_{n0} + a_{2n}A_n] + ta_{2n+1}D_n, \\ C_n &= t [\delta_{n0} + a_{2n}A_n] - \frac{r^*t}{t^*}a_{2n+1}D_n, \\ A_n &= Fr^*a_{2n}B_n + t^*a_{2n-1}C_{n-1}, \\ D_{n-1} &= t^*a_{2n}B_n - F^*\frac{rt^*}{t}a_{2n-1}C_{n-1}. \end{aligned}$$

The above equations (D.7)-(D.10) form a system of four equations with four unknowns. By substituting them into each other, we can reduce this to a single recurrence relation for  $B_n$ . After solving for  $B_n$ , we express  $A_n$  in terms of  $B_n$ , since  $A_n$  and  $B_n$  combined are sufficient to calculate the current through the junction.

In the following, we will need expressions for both indices  $n$  and  $n - 1$ , which can be obtained by simply substituting  $n \mapsto n - 1$  (for  $B_n$ ,  $C_n$  and

$A_n$ ) and  $n \mapsto n + 1$  (for  $D_{n-1}$ ). The full set of equations that we will use is

$$\begin{cases} B_n = r [\delta_{n0} + a_{2n}A_n] + ta_{2n+1}D_n, \\ B_{n-1} = r [\delta_{n-1,0} + a_{2n-2}A_{n-1}] + ta_{2n-1}D_{n-1}, \end{cases} \quad (\text{D.7})$$

$$\begin{cases} C_n = t [\delta_{n0} + a_{2n}A_n] - \frac{r^*t}{t^*}a_{2n+1}D_n, \\ C_{n-1} = t [\delta_{n-1,0} + a_{2n-2}A_{n-1}] - \frac{r^*t}{t^*}a_{2n-1}D_{n-1}, \end{cases} \quad (\text{D.8})$$

$$\begin{cases} A_n = Fr^*a_{2n}B_n + t^*a_{2n-1}C_{n-1}, \\ A_{n-1} = Fr^*a_{2n-2}B_{n-1} + t^*a_{2n-3}C_{n-2}, \end{cases} \quad (\text{D.9})$$

$$\begin{cases} D_n = t^*a_{2n+2}B_{n+1} - F^*\frac{rt^*}{t}a_{2n+1}C_n, \\ D_{n-1} = t^*a_{2n}B_n - F^*\frac{rt^*}{t}a_{2n-1}C_{n-1}, \end{cases} \quad (\text{D.10})$$

### D.2.1 Recurrence relation for $B_n$

We aim to substitute all relations between  $B_n$ ,  $C_n$ ,  $A_n$  and  $D_n$  into each other to obtain a closed recurrence relation for  $B_n$ . We start from  $B_n$  in (D.7) and substitute  $A_n$  from (D.9) and  $D_n$  from (D.10) into  $B_n$  from (D.7), which gives a relation between  $B_n$  and  $C_n$ . We obtain

$$\begin{aligned} B_n &= r [\delta_{n0} + a_{2n} (Fr^*a_{2n}B_n + t^*a_{2n-1}C_{n-1})] + ta_{2n+1} \left( t^*a_{2n+2}B_{n+1} - F^*\frac{rt^*}{t}a_{2n+1}C_n \right) \\ &= r\delta_{n0} + Frr^*a_{2n}^2B_n + rt^*a_{2n}a_{2n-1}C_{n-1} + tt^*a_{2n+1}a_{2n+2}B_{n+1} - F^*rt^*a_{2n+1}^2C_n. \end{aligned} \quad (\text{D.11})$$

We also substitute (D.9) and (D.10) into  $C_n$  from (D.8) to obtain a second relation between  $B_n$  and  $C_n$ , that is

$$\begin{aligned} C_n &= t\delta_{n0} + ta_{2n} (Fr^*a_{2n}B_n + t^*a_{2n-1}C_{n-1}) - \frac{r^*t}{t^*}a_{2n+1} \left( t^*a_{2n+2}B_{n+1} - F^*\frac{rt^*}{t}a_{2n+1}C_n \right) \\ &= t\delta_{n0} + Ftr^*a_{2n}^2B_n + tt^*a_{2n}a_{2n-1}C_{n-1} - r^*ta_{2n+1}a_{2n+2}B_{n+1} + F^*r^*ra_{2n+1}^2C_n. \end{aligned} \quad (\text{D.12})$$

To combine (D.11) and (D.12), we conveniently write the source term on the left-hand-side and all other terms on the right. We obtain

$$\begin{cases} \delta_{n0} = \frac{1}{r} [1 - Frr^*a_{2n}^2] B_n - t^*a_{2n}a_{2n-1}C_{n-1} - \frac{tt^*}{r}a_{2n+1}a_{2n+2}B_{n+1} + F^*t^*a_{2n+1}^2C_n. \\ \delta_{n0} = \frac{1}{t} [1 - F^*r^*ra_{2n+1}^2] C_n - Frr^*a_{2n}^2B_n - t^*a_{2n}a_{2n-1}C_{n-1} + r^*a_{2n+1}a_{2n+2}B_{n+1}. \end{cases} \quad (\text{D.13})$$

This allows us to equate the two equations. The  $t^*a_{2n}2_{2n-1}C_{n-1}$  and  $Fr^*a_{2n}^2B_n$  terms cancel. What remains is

$$\frac{1}{r}B_n = \left[ \frac{1}{t} - F^* \left( \frac{r^*r}{t} + t^* \right) a_{2n+1}^2 \right] C_n + \left( r^* + \frac{tt^*}{r} \right) a_{2n+1}a_{2n+2}B_{n+1}. \quad (\text{D.14})$$

We use the probability conversion  $r^*r + t^*t = rr^* + tt^* = 1$  to simplify the terms between round brackets and find

$$\frac{1}{r}B_n = \frac{1}{t} [1 - F^*a_{2n+1}^2] C_n + \frac{1}{r}a_{2n+1}a_{2n+2}B_{n+1}. \quad (\text{D.15})$$

We divide by  $C_n$ 's pre-factor to express  $C_n$  in terms of  $B_n$  by rewriting Eq. (D.15):

$$C_n = \frac{t}{r} \frac{1}{1 - F^*a_{2n+1}^2} B_n - \frac{t}{r} \frac{a_{2n+1}a_{2n+2}}{1 - F^*a_{2n+1}^2} B_{n+1}. \quad (\text{D.16})$$

Accordingly, by replacing  $n \mapsto n-1$ , we find an expression for  $C_{n-1}$ :

$$C_{n-1} = \frac{t}{r} \frac{1}{1 - F^*a_{2n-1}^2} B_{n-1} - \frac{t}{r} \frac{a_{2n-1}a_{2n}}{1 - F^*a_{2n-1}^2} B_n. \quad (\text{D.17})$$

We now substitute (D.16) and (D.17) into (D.11)

$$\begin{aligned} B_n &= r\delta_{n0} + Fr^*a_{2n}^2B_n + rt^*a_{2n}a_{2n-1} \left( \frac{t}{r} \frac{1}{1 - F^*a_{2n-1}^2} B_{n-1} - \frac{t}{r} \frac{a_{2n-1}a_{2n}}{1 - F^*a_{2n-1}^2} B_n \right) \\ &\quad + tt^*a_{2n+1}a_{2n+2}B_{n+1} - F^*rt^*a_{2n+1}^2 \left( \frac{t}{r} \frac{1}{1 - F^*a_{2n+1}^2} B_n - \frac{t}{r} \frac{a_{2n+1}a_{2n+2}}{1 - F^*a_{2n+1}^2} B_{n+1} \right) \\ &= r\delta_{n0} + Fr^*a_{2n}^2B_n + tt^* \frac{a_{2n}a_{2n-1}}{1 - F^*a_{2n-1}^2} B_{n-1} - tt^* \frac{a_{2n-1}^2a_{2n}^2}{1 - F^*a_{2n-1}^2} B_n \\ &\quad + tt^*a_{2n+1}a_{2n+2}B_{n+1} - tt^* \frac{F^*a_{2n+1}^2}{1 - F^*a_{2n+1}^2} B_n + tt^* \frac{F^*a_{2n+1}^3a_{2n+2}}{1 - F^*a_{2n+1}^2} B_{n+1}. \end{aligned}$$

We sort all the terms as follows:

$$\begin{aligned} tt^* \left[ \frac{F^*a_{2n+1}^3a_{2n+2}}{1 - F^*a_{2n+1}^2} + a_{2n+1}a_{2n+2} \right] B_{n+1} - \left[ 1 - Fr^*a_{2n}^2 + tt^* \left( \frac{a_{2n-1}^2a_{2n}^2}{1 - F^*a_{2n-1}^2} + \frac{F^*a_{2n+1}^2}{1 - F^*a_{2n+1}^2} \right) \right] B_n \\ + tt^* \frac{a_{2n}a_{2n-1}}{1 - F^*a_{2n-1}^2} B_{n-1} = -r\delta_{n0}. \end{aligned}$$

The coefficient in front of  $B_{n+1}$  can be simplified as

$$\frac{F^*a_{2n+1}^3a_{2n+2}}{1 - F^*a_{2n+1}^2} + a_{2n+1}a_{2n+2} = \frac{a_{2n+1}a_{2n+2}}{1 - F^*a_{2n+1}^2}, \quad (\text{D.18})$$

which makes it symmetric with the  $B_{n-1}$  coefficient. We define the interface transparency as  $D \equiv tt^*$ . The final recurrence relation for  $B_n$  becomes

$$D \frac{a_{2n+1}a_{2n+2}}{1 - F^*a_{2n+1}^2} B_{n+1} - \left[ 1 - Fr r^* a_{2n}^2 + D \left( \frac{a_{2n-1}^2 a_{2n}^2}{1 - F^*a_{2n-1}^2} + \frac{F^* a_{2n+1}^2}{1 - F^*a_{2n+1}^2} \right) \right] B_n \quad (\text{D.19})$$

$$+ D \frac{a_{2n}a_{2n-1}}{1 - F^*a_{2n-1}^2} B_{n-1} = -r\delta_{n0}. \quad (\text{D.20})$$

We can cast the recurrence relation (D.20), to a more general to reveal the mathematical structure more explicitly. By dividing (D.20) by the term in front of  $B_{n+1}$  we get,

$$B_{n+1} + \gamma_n B_n + \chi_n B_{n-1} = \zeta_n \delta_{n0}. \quad (\text{D.21})$$

where,

$$\gamma_n = -\frac{1}{D} \frac{(1 - F a_{2n}^2)(1 - F^* a_{2n+1}^2)}{a_{2n+1} a_{2n+2}} - a_{2n}^2 \frac{F - (FF^* - 1)a_{2n-1}^2}{1 - F^* a_{2n-1}^2} \frac{1 - F^* a_{2n+1}^2}{a_{2n+1} a_{2n+2}} - F^* \frac{a_{2n+1}}{a_{2n+2}} \quad (\text{D.22})$$

$$\chi_n = \frac{a_{2n} a_{2n-1} (1 - F^* a_{2n+1}^2)}{a_{2n+1} a_{2n+2} (1 - F^* a_{2n-1}^2)} \quad (\text{D.23})$$

$$\zeta_n = \frac{r}{D} \frac{1 - F^* a_{2n+1}^2}{a_{2n+1} a_{2n+2}} \delta_{n0} \quad (\text{D.24})$$

In the form (D.21) we readily recognize the non-homogeneous three term recurrence relation for  $B_n$ .

## D.2.2 Recurrence relation for $A_n$

Now that we have found a closed expression for  $B_n$ , we can consider  $B_n$  as known and express  $A_n$  in terms of  $B_n$ . Substituting  $C_{n-1}$  from (D.8) into  $A_n$  from (D.9) yields

$$\begin{aligned} A_n &= Fr^* a_{2n} B_n + t^* a_{2n-1} \left( t a_{2n-2} A_{n-1} - \frac{r^* t}{t^*} a_{2n-1} D_{n-1} + t \delta_{n-1,0} \right) \\ &= Fr^* a_{2n} B_n + tt^* a_{2n-1} a_{2n-2} A_{n-1} - r^* t a_{2n-1}^2 D_{n-1} + tt^* a_{2n-1} \delta_{n-1,0}. \end{aligned}$$

We use probability conversation to rewrite  $tt^* = 1 - rr^*$  and sort the terms in a clever way, as follows

$$\begin{aligned} A_n - a_{2n-1} a_{2n-2} A_{n-1} &= Fr^* a_{2n} B_n - r^* a_{2n-1} (t a_{2n-1} D_{n-1} + r a_{2n-2} A_{n-1} + r \delta_{n-1,0}) \\ &\quad + a_{2n-1} \delta_{n-1,0}. \end{aligned} \quad (\text{D.25})$$

We note that the part in between brackets is exactly  $B_{n-1}$  from (D.7). Hence, we rewrite (D.25) as

$$A_n - a_{2n-1}a_{2n-2}A_{n-1} = Fr^*a_{2n}B_n - r^*a_{2n-1}B_{n-1} + a_{2n-1}\delta_{n-1,0}.$$

This is already a correct recurrence relation for  $A_n$ . However, to mimic the recurrence relations in literature, we replace  $n \mapsto n+1$ . The source term has a Kronecker  $\delta$ -function at  $n=0$ , which turns its pre-factor into  $a_{2n+1} = a_1$ . Our final recurrence relation for  $A_n$  becomes

$$A_{n+1} - a_{2n+1}a_{2n}A_n = r^*(Fa_{2n+2}B_{n+1} - a_{2n+1}B_n) + a_1\delta_{n0}. \quad (\text{D.26})$$

We can write (D.26) in the following form,

$$A_{n+1} + \gamma'_n A_n = f(n). \quad (\text{D.27})$$

where,

$$\gamma'_n = -a_{2n+1}a_{2n} \quad (\text{D.28})$$

$$f(n) = r^*(Fa_{2n+2}B_{n+1} - a_{2n+1}B_n) + a_1\delta_{n0}. \quad (\text{D.29})$$

and recognize the non-homogeneous two term recurrence relation (D.27).

## References

- [1] L. Fu and C. L. Kane, “Superconducting proximity effect and Majorana fermions at the surface of a topological insulator,” *Physical Review Letters*, vol. 100, p. 096407, Mar. 2008. arXiv: 0707.1692.
- [2] A. Y. Kitaev, “Fault-tolerant quantum computation by anyons,” *Annals of Physics*, vol. 303, pp. 2–30, Jan. 2003. arXiv: quant-ph/9707021.
- [3] G. E. Blonder, M. Tinkham, and T. M. Klapwijk, “Transition from metallic to tunneling regimes in superconducting microconstrictions: Excess current, charge imbalance, and supercurrent conversion,” *Physical Review B*, vol. 25, pp. 4515–4532, Apr. 1982.
- [4] Emani *et al.*, “Quantum computing at the frontiers of biological sciences,” *Nature Methods*, vol. 18, pp. 701–709, July 2021.
- [5] Y. Kanamori and S.-M. Yoo, “Quantum Computing: Principles and Applications,” *Quantum Computing*, p. 30, 2020.
- [6] G. E. Moore, “Cramming More Components onto Integrated Circuits,” *Proceedings of the IEEE*, vol. 86, no. 1, p. 4, 1998.
- [7] T. N. Theis and H.-S. P. Wong, “The End of Moore’s Law: A New Beginning for Information Technology,” *Computing in Science & Engineering*, vol. 19, pp. 41–50, Mar. 2017.
- [8] R. de Wolf, “Quantum Computing: Lecture Notes,” *arXiv:1907.09415 [quant-ph]*, Jan. 2022. arXiv: 1907.09415.
- [9] P. Lambropoulos and D. Petrosyan, *Fundamentals of quantum optics and quantum information*. Berlin ; New York: Springer, 2007. OCLC: ocm74650533.
- [10] Y. I. . Manin, “Vychislimoe i nevychislimoe [Computable and Noncomputable] (in Russian),” pp. 13–15, 1980.
- [11] R. P. Feynman, “Simulating Physics with Computers,” vol. VoL 21, no. Nos. 6/7, p. 103, 1982.
- [12] P. Benioff, “Quantum mechanical hamiltonian models of turing machines,” *Journal of Statistical Physics*, vol. 29, pp. 515–546, Nov. 1982.
- [13] P. W. Shor, “Polynomial-Time Algorithms for Prime Factorization and Discrete Logarithms on a Quantum Computer,” *SIAM Journal on Computing*, vol. 26, pp. 1484–1509, Oct. 1997. arXiv: quant-ph/9508027.
- [14] M. Stamp, *Information Security: Principles and Practice*. Wiley, 2011.
- [15] C. H. Bennett and G. Brassard, “Quantum cryptography: Public key distribution and coin tossing,” in *Proceedings of IEEE International Conference on Computers, Systems, and Signal Processing*, (India), 1984.
- [16] Arute *et al.*, “Quantum supremacy using a programmable superconducting processor,” *Nature*, vol. 574, pp. 505–510, Oct. 2019.
- [17] D. DiVincenzo and D. Loss, “Quantum information is physical,” *Superlattices and Microstructures*, vol. 23, pp. 419–432, Mar. 1998.

- [18] C. Kloeffer and D. Loss, “Prospects for Spin-Based Quantum Computing,” *Annual Review of Condensed Matter Physics*, vol. 4, pp. 51–81, Apr. 2013. arXiv: 1204.5917.
- [19] J. Casanova, Z.-Y. Wang, and M. Plenio, “Noise-Resilient Quantum Computing with a Nitrogen-Vacancy Center and Nuclear Spins,” *Physical Review Letters*, vol. 117, p. 130502, Sept. 2016.
- [20] T. C. Ralph and G. J. Pryde, “Optical Quantum Computation,” in *Progress in Optics*, vol. 54, pp. 209–269, Elsevier, 2010.
- [21] J. L. O’Brien, “Optical quantum computing,” *Science*, vol. 318, no. 5856, pp. 1567–1570, 2007.
- [22] V. Lahtinen and J. K. Pachos, “A Short Introduction to Topological Quantum Computation,” *SciPost Physics*, vol. 3, p. 021, Sept. 2017. arXiv: 1705.04103.
- [23] C. Nayak, S. H. Simon, A. Stern, M. Freedman, and S. Das Sarma, “Non-Abelian anyons and topological quantum computation,” *Reviews of Modern Physics*, vol. 80, pp. 1083–1159, Sept. 2008.
- [24] F. Wilczek, *Fractional Statistics and Anyon Superconductivity*. WORLD SCIENTIFIC, 1990.
- [25] D. J. Griffiths, *Introduction to Quantum Mechanics*. Pearson Prentice Hall, 2 ed., 2005.
- [26] M. H. Freedman, A. Kitaev, M. J. Larsen, and Z. Wang, “Topological Quantum Computation,” *Topological quantum computation*, p. 8, 2002.
- [27] J. Alicea, “New directions in the pursuit of Majorana fermions in solid state systems,” *Reports on Progress in Physics*, vol. 75, p. 076501, July 2012. arXiv: 1202.1293.
- [28] E. Majorana, “Teoria simmetrica dell’elettrone e del positrone,” *Il Nuovo Cimento (1924-1942)*, vol. 14, p. 171, Sept. 2008.
- [29] F. Wilczek, “Majorana returns,” *Nature Physics*, vol. 5, pp. 614–618, Sept. 2009.
- [30] C. W. J. Beenakker, “Search for Majorana fermions in superconductors,” *Annual Review of Condensed Matter Physics*, vol. 4, pp. 113–136, Apr. 2013. arXiv: 1112.1950.
- [31] N. Read and D. Green, “Paired states of fermions in two dimensions with breaking of parity and time-reversal symmetries and the fractional quantum Hall effect,” *Physical Review B*, vol. 61, pp. 10267–10297, Apr. 2000.
- [32] T. Kokkeler, “Usadel equation for a four terminal junction,” 2021.
- [33] A. Chronister, A. Pustogow, N. Kikugawa, D. A. Sokolov, F. Jerzembeck, C. W. Hicks, A. P. Mackenzie, E. D. Bauer, and S. E. Brown, “Evidence for even parity unconventional superconductivity in  $\text{Sr}_2\text{RuO}_4$ ,” *Proceedings of the National Academy of Sciences*, vol. 118, p. e2025313118, June 2021.
- [34] A. Kitaev, “Unpaired Majorana fermions in quantum wires,” *Physics-Uspekhi*, vol. 44, pp. 131–136, Oct. 2001. arXiv: cond-mat/0010440.
- [35] R. M. Lutchyn, J. D. Sau, and S. Das Sarma, “Majorana Fermions and a Topological Phase Transition in Semiconductor-Superconductor Heterostructures,” *Physical Review Letters*, vol. 105, p. 077001, Aug. 2010.

- [36] Y. Oreg, G. Refael, and F. von Oppen, “Helical Liquids and Majorana Bound States in Quantum Wires,” *Physical Review Letters*, vol. 105, p. 177002, Oct. 2010.
- [37] X.-G. Wen, *Quantum field theory of many-body systems: From the origin of sound to an origin of light and electrons*. Oxford: Oxford: Oxford University Press, 2010.
- [38] Y. Tanaka, T. Yokoyama, and N. Nagaosa, “Manipulation of Majorana fermion, Andreev reflection and Josephson current on topological insulators,” *Physical Review Letters*, vol. 103, p. 107002, Sept. 2009. arXiv: 0907.2088.
- [39] A. D. Vela, G. Lemut, M. J. Pacholski, and C. W. J. Beenakker, “Chirality inversion of Majorana edge modes in a Fu-Kane heterostructure,” *New Journal of Physics*, vol. 23, p. 103006, Oct. 2021. arXiv: 2105.04433.
- [40] D. Averin and A. Bardas, “AC Josephson effect in a single quantum channel,” *Physical Review Letters*, vol. 75, pp. 1831–1834, Aug. 1995. arXiv: cond-mat/9505096.
- [41] D. M. Badiane, M. Houzet, and J. S. Meyer, “Nonequilibrium Josephson Effect through Helical Edge States,” *Physical Review Letters*, vol. 107, p. 177002, Oct. 2011.
- [42] S.-I. Suzuki, A. A. Golubov, Y. Asano, and Y. Tanaka, “Effects of phase coherence on local density of states in superconducting proximity structures,” *Physical Review B*, vol. 100, p. 024511, July 2019.
- [43] M. Leijnse and K. Flensberg, “Introduction to topological superconductivity and Majorana fermions,” *Semiconductor Science and Technology*, vol. 27, p. 124003, Dec. 2012. arXiv: 1206.1736.
- [44] D. Rosenbach, N. Oellers, A. R. Jalil, M. Mikulics, J. Kölzer, E. Zimmermann, G. Mussler, S. Bunte, D. Grützmacher, H. Lüth, and T. Schäpers, “Quantum Transport in Topological Surface States of Selectively Grown Bi<sub>2</sub>Te<sub>3</sub> Nanoribbons,” *Advanced Electronic Materials*, vol. 6, p. 2000205, Aug. 2020.
- [45] D. M. Badiane, L. I. Glazman, M. Houzet, and J. S. Meyer, “Ac Josephson effect in topological Josephson junctions,” *Comptes Rendus Physique*, vol. 14, pp. 840–856, Nov. 2013.
- [46] L. Olde Olthof, “Interfaces of topological insulators and superconductors,” August 2018.
- [47] J.-X. Zhu, “Bogoliubov-de Gennes Method and Its Applications, ch 6.4,” in *Bogoliubov-de Gennes Method and Its Applications*, vol. 924, p. 159, 2016.
- [48] V. V. Schmidt, *The Physics of Superconductors*. Berlin, Heidelberg: Springer Berlin Heidelberg, 1997.
- [49] D. van Delft and P. Kes, “The discovery of superconductivity,” p. 6.
- [50] H. K. Onnes, “Phys. lab. univ. leiden. suppl. 29,” 1911.
- [51] E. Snider, N. Dasenbrock-Gammon, R. McBride, M. Debessai, H. Vindana, K. Venkatasamy, K. V. Lawler, A. Salamat, and R. P. Dias, “Room-temperature superconductivity in a carbonaceous sulfur hydride,” *Nature*, vol. 586, pp. 373–377, Oct. 2020.

- [52] P. J. Ray, “Figure 2.4 in master’s thesis, ”structural investigation of  $la_{2-x}sr_xcuo_{4+y}$  - following staging as a function of temperature”,” *Niels Bohr Institute, Faculty of Science, University of Copenhagen*, November 2015.
- [53] F. London and H. London, “The electromagnetic equations of the supraconductor,” *Proceedings of the Royal Society of London*, vol. 149, p. 18, Mar. 1935.
- [54] V. Ginzburg and L. Landau, “On the theory of superconductivity,” vol. 20, p. 1064, 1950.
- [55] G.-H. Lee and H.-J. Lee, “Proximity coupling in superconductor-graphene heterostructures,” *Reports on Progress in Physics*, vol. 81, p. 056502, mar 2018.
- [56] J. Bardeen, L. N. Cooper, and J. R. Schrieffer, “Microscopic Theory of Superconductivity,” *Physical Review*, vol. 106, pp. 162–164, Apr. 1957.
- [57] R. P. Feynman, “Space-Time Approach to Quantum Electrodynamics,” *Physical Review*, vol. 76, pp. 769–789, Sept. 1949.
- [58] J. Island, *Quantum transport in superconducting hybrids: Molecular devices and layered materials*. 2016. OCLC: 7792843682.
- [59] C. W. J. Beenakker, “Why does a metal-superconductor junction have a resistance?,” *arXiv:cond-mat/9909293*, pp. 51–60, 2000. arXiv: cond-mat/9909293.
- [60] A. F. Andreev, “Thermal conductivity of the intermediate state of superconductors,” *Zh. Eksperim. i Teor. Fiz.*, vol. Vol: 46, 5 1964.
- [61] D. Supriyo, *Electronic Transport in Mesoscopic Systems*. Cambridge Studies in Semiconductor Physics and Microelectronic Engineering, Cambridge: Cambridge University Press, 10 ed., 1995.
- [62] M. I. Katsnelson, K. S. Novoselov, and A. K. Geim, “Chiral tunneling and the Klein paradox in graphene,” *Nature Physics*, vol. 2, pp. 620–625, Sept. 2006. arXiv: cond-mat/0604323.
- [63] N. Bohr, “On the Constitution of Atoms and Molecules,” in *Niels Bohr, 1913-2013* (O. Darrigol, B. Duplantier, J.-M. Raimond, and V. Rivasseau, eds.), vol. 68, pp. 13–33, Cham: Springer International Publishing, 2016. Series Title: Progress in Mathematical Physics.
- [64] A. Sommerfeld, “Zur theorie der balmerschen serie,” *Sitzung-berichte der Bayerischen Akademie der Wissenschaften, mathematisch-physikalische Klasse (München)*, pp. 425–458, 1915.
- [65] T. Klapwijk, G. Blonder, and M. Tinkham, “Explanation of subharmonic energy gap structure in superconducting contacts,” *Physica B+C*, vol. 109-110, pp. 1657–1664, 1982. 16th International Conference on Low Temperature Physics, Part 3.
- [66] L. Mulder, C. Castenmiller, F. J. Witmans, S. Smit, M. S. Golden, H. J. W. Zandvliet, P. L. de Boeij, and A. Brinkman, “Spectroscopic signature of surface states and bunching of bulk subbands in topological insulator ( Bi 0.4 Sb 0.6 ) 2 Te 3 thin films,” *Physical Review B*, vol. 105, p. 035122, Jan. 2022.
- [67] A. P. Ramirez and B. Skinner, “Dawn of the topological age?,” *Physics Today*, vol. 73, pp. 30–36, Sept. 2020.

- [68] M. Z. Hasan and C. L. Kane, “Colloquium : Topological insulators,” *Reviews of Modern Physics*, vol. 82, pp. 3045–3067, Nov. 2010.
- [69] B. Bernevig and T. Hughes, *Topological insulators and topological superconductors*. Princeton University Press, Mar. 2013.
- [70] C. Kittel, *Introduction to solid state physics 8th Edition*. John Wiley Sons, 2005.
- [71] H. Weng, X. Dai, and Z. Fang, “From anomalous hall effect to the quantum anomalous hall effect,” 09 2015.
- [72] S. Murakami, “Phase transition between the quantum spin hall and insulator phases in 3d: emergence of a topological gapless phase,” *New Journal of Physics*, vol. 9, pp. 356–356, sep 2007.
- [73] L. Mulder, *Pushing a topological insulator to its ultrathin limit*. PhD thesis, University of Twente, Netherlands, Nov. 2021.
- [74] M. Snelder, *Non-triviality matters: examining the interplay between s-wave superconductivity and topological surface states*. PhD thesis, University of Twente, June 2015.
- [75] J.-X. Zhu, “Bogoliubov-de Gennes Method and Its Applications ch1,” in *Bogoliubov-de Gennes Method and Its Applications*, vol. 924, pp. 3–35, 2016.
- [76] Y. Ando, “Topological insulator materials,” *Journal of the Physical Society of Japan*, vol. 82, no. 10, p. 102001, 2013.
- [77] A. Manchon, H. C. Koo, J. Nitta, S. M. Frolov, and R. A. Duine, “New perspectives for Rashba spin-orbit coupling,” *Nature Materials*, vol. 14, pp. 871–882, Sept. 2015.
- [78] Y. Tokura, K. Yasuda, and A. Tsukazaki, “Magnetic topological insulators,” *Nature Reviews Physics*, vol. 1, pp. 126–143, Feb. 2019.
- [79] W. Belzig, F. Wilhelm, C. Bruder, G. Schön, and A. Zaikin, “Quasiclassical Green’s function approach to mesoscopic superconductivity,” *Superlattices and Microstructures*, vol. 25, no. 5-6, p. 1251, 1999. 1251.
- [80] P.-G. d. Gennes, *Superconductivity of metals and alloys*. Advanced book classics, Redwood City, Calif.: Addison-Wesley, 1989. Section: xxii, 274 pages : illustrations ; 24 cm.
- [81] J.-X. Zhu, *Bogoliubov-de Gennes Method and Its Applications*, vol. 924. 2016.
- [82] A. L. Kuzemsky, “Variational Principle of Bogoliubov and Generalized Mean Fields in Many-Particle Interacting Systems,” *International Journal of Modern Physics B*, vol. 29, p. 1530010, July 2015. arXiv: 1507.00563.
- [83] E. Reich, “Bilinear forms.” <https://math.mit.edu/~dav/bilinearforms.pdf>.
- [84] N. N. Bogoljubov, “On a new method in the theory of superconductivity,” *Il Nuovo Cimento*, vol. 7, pp. 794–805, Mar. 1958.
- [85] M. Haase, *Functional analysis: an elementary introduction*. No. volume 156 in Graduate studies in mathematics, Providence, Rhode Island: American Mathematical Society, 2014.

- [86] M. OpenCourseWare, “Linear algebra: 18.06sc.” [https://ocw.mit.edu/courses/mathematics/18-06sc-linear-algebra-fall-2011/positive-definite-matrices-and-applications/similar-matrices-and-jordan-form/MIT18\\_06SCF11\\_Ses3.4sum.pdf](https://ocw.mit.edu/courses/mathematics/18-06sc-linear-algebra-fall-2011/positive-definite-matrices-and-applications/similar-matrices-and-jordan-form/MIT18_06SCF11_Ses3.4sum.pdf). Accessed: 2022-02-01.
- [87] S. Ryu, A. Schnyder, A. Furusaki, and A. Ludwig, “Topological insulators and superconductors: ten-fold way and dimensional hierarchy,” *New Journal of Physics*, vol. 12, p. 065010, June 2010. arXiv: 0912.2157.
- [88] T. Delft University of Technology: open course, “Bulk-edge correspondence in the Kitaev chain.” [https://topocondmat.org/w1\\_topointro/1D.html](https://topocondmat.org/w1_topointro/1D.html). Accessed: 2022-02-01.
- [89] T. Delft University of Technology: open course, “Hamiltonians, topology, and symmetry.” [https://topocondmat.org/w1\\_topointro/1D.html](https://topocondmat.org/w1_topointro/1D.html). Accessed: 2022-02-01.
- [90] F. de Juan, J. H. Bardarson, and R. Ilan, “Conditions for fully gapped topological superconductivity in topological insulator nanowires,” *SciPost Physics*, vol. 6, p. 060, May 2019.
- [91] B. Martin, “Nuclear and particle physics,” 2006.
- [92] M. Z. Hasan and C. L. Kane, “Topological Insulators,” *Reviews of Modern Physics*, vol. 82, pp. 3045–3067, Nov. 2010. arXiv: 1002.3895.
- [93] D. Zhang, T. Le, B. Lv, L. Yin, C. Chen, Z. Nie, D. Su, H. Yuan, Z.-A. Xu, and X. Lu, “Full superconducting gap and type-I to type-II superconductivity transition in single crystalline NbGe<sub>2</sub>,” *Physical Review B*, vol. 103, p. 214508, June 2021.
- [94] Meurer *et al.*, “SymPy: symbolic computing in Python,” *PeerJ Computer Science*, vol. 3, p. e103, Jan. 2017.
- [95] C. Li, J. C. de Boer, B. de Ronde, S. V. Ramankutty, E. van Heumen, Y. Huang, A. de Visser, A. A. Golubov, M. S. Golden, and A. Brinkman, “ $4\pi$  periodic Andreev bound states in a Dirac semimetal,” *Nature Materials*, vol. 17, pp. 875–880, Oct. 2018. arXiv: 1707.03154.
- [96] P. Markoš and C. M. Soukoulis, “Wave Propagation - From Electrons to Photonic Crystals and Left-Handed Materials,” Publisher: Princeton University Press.
- [97] C.-X. Liu, J. D. Sau, T. D. Stanescu, and S. Das Sarma, “Andreev bound states versus Majorana bound states in quantum dot-nanowire-superconductor hybrid structures: Trivial versus topological zero-bias conductance peaks,” *Physical Review B*, vol. 96, p. 075161, Aug. 2017.
- [98] e. b. A. R. E.L. Wachspress and H. Wilf, *Mathematische Methoden für Digitalrechner*. Oldenbourg Verlag, 1972.
- [99] W. Gautschi, “Computational Aspects of Three-Term Recurrence Relations,” *SIAM Review*, vol. 9, pp. 24–82, Jan. 1967.
- [100] M. Eschrig, “Theory of Andreev bound states in S-F-S junctions and S-F proximity devices,” *Philosophical Transactions of the Royal Society A: Mathematical, Physical and Engineering Sciences*, vol. 376, p. 20150149, Aug. 2018.

- [101] B. Skinner, “There’s nothing particularly “spooky” about avoided crossing.” <https://gravityandlevity.wordpress.com/2014/04/08/avoided-crossing/>. Accessed: 2022-02-01.
- [102] R. Giraud and J. Dufouleur, “Quantum Transport in Nanostructures of 3D Topological Insulators,” *physica status solidi (b)*, vol. 258, p. 2000066, Jan. 2021.
- [103] A. Brinkman and A. A. Golubov, “Coherence effects in double-barrier Josephson junctions,” *Physical Review B*, vol. 61, pp. 11297–11300, May 2000.
- [104] P. E. Allain and J. N. Fuchs, “Klein tunneling in graphene: optics with massless electrons,” *The European Physical Journal B*, vol. 83, pp. 301–317, Oct. 2011.